



**Michigan
Technological
University**

Michigan Technological University
Digital Commons @ Michigan Tech

Dissertations, Master's Theses and Master's Reports

2021

Multi-level analysis of atomic layer deposition barrier coatings on additively manufactured plastics for high vacuum applications

Nupur Bihari

Michigan Technological University, nbihari@mtu.edu

Copyright 2021 Nupur Bihari

Recommended Citation

Bihari, Nupur, "Multi-level analysis of atomic layer deposition barrier coatings on additively manufactured plastics for high vacuum applications", Open Access Dissertation, Michigan Technological University, 2021.

<https://doi.org/10.37099/mtu.dc.etr/1208>

Follow this and additional works at: <https://digitalcommons.mtu.edu/etr>

 Part of the [Inorganic Chemistry Commons](#), [Materials Chemistry Commons](#), [Nanoscience and Nanotechnology Commons](#), [Polymer and Organic Materials Commons](#), [Polymer Chemistry Commons](#), and the [Semiconductor and Optical Materials Commons](#)

MULTI-LEVEL ANALYSIS OF ATOMIC LAYER DEPOSITION BARRIER
COATINGS ON ADDITIVELY MANUFACTURED PLASTICS FOR HIGH
VACUUM APPLICATIONS

By

Nupur Bihari

A DISSERTATION

Submitted in partial fulfillment of the requirements for the degree of

DOCTOR OF PHILOSOPHY

In Materials Science and Engineering

MICHIGAN TECHNOLOGICAL UNIVERSITY

2021

© 2021 Nupur Bihari

This dissertation has been approved in partial fulfillment of the requirements for the Degree of DOCTOR OF PHILOSOPHY in Materials Science and Engineering.

Department of Materials Science and Engineering

Dissertation Advisor: *Dr. Joshua M. Pearce*

Committee Member: *Dr. Paul L. Bergstrom*

Committee Member: *Dr. Kathryn A. Perrine*

Committee Member: *Dr. Stephen A. Hackney*

Department Chair: *Dr. Stephen L. Kampe*

Table of Contents

List of Figures	v
List of Tables	ix
Author Contribution Statement.....	x
Acknowledgements.....	xi
Abstract.....	xiii
1 Introduction.....	1
1.1 Outline.....	1
2 3D Printable Open Source Dual Axis Gimbal System for Optoelectronics Measurements	3
2.1 Introduction	3
2.2 Materials and methods.....	4
2.2.1 Mechanical Architecture.....	5
2.2.2 Electronic Architecture	12
2.2.3 Software Architecture	12
2.3 Validation and Demonstration.....	15
2.4 Results	17
2.4.1 Demonstration of Angular Dependence of Transmission.....	18
2.4.2 Unidirectional Accuracy	18
2.4.3 Repeatability	19
2.4.4 Backlash.....	20
2.4.5 Maximum Speed	21
2.4.6 Speed resolution.....	21
2.4.7 Micro step Size	22
2.4.8 Angular Limitations.....	22
2.5 Discussion	23
2.6 Conclusions	26
2.7 Acknowledgements	26
2.8 References	26
3 Atomic layer deposited aluminum oxide mitigates outgassing from fused filament fabrication-based 3-D printed components	34
3.1 Introduction	34
3.2 Experimental	35
3.2.1 Sample preparation	35
3.2.2 Characterization.....	36
3.3 Results	38
3.4 Discussion	46

3.5	Conclusions	49
3.6	Acknowledgments	50
3.7	References	50
4	Vacuum Outgassing Characteristics of Unpigmented 3-D Printed Polymers Coated with ALD Alumina	55
4.1	Introduction	55
4.2	Experimental	56
4.2.1	Sample preparation	57
4.2.2	Characterization	58
4.2.2.1	Thickness of deposited film	58
4.2.2.2	Microstructure and chemical analysis.....	58
4.2.2.3	Residual gas analysis for outgassing quantification	58
4.3	Results and Discussion	59
4.4	Conclusions	69
4.5	Acknowledgements	70
4.6	References	70
5	Understanding the multilevel phenomena that enables inorganic atomic layer deposition to provide barrier coatings for highly-porous 3-D printed plastic in ultra-high vacuums	74
5.1	Introduction	74
5.2	Experimental	76
5.2.1	Characterization	76
5.2.1.1	Thickness of deposited film	76
5.2.1.2	Residual gas analysis for outgassing quantification	77
5.2.1.3	Microstructure analysis.....	77
5.2.1.4	FTIR.....	77
5.2.1.5	Crystallinity calculation using XRD.....	77
5.2.1.6	Surface analysis using XPS	78
5.3	Results and discussion.....	78
5.4	Conclusions	90
5.5	Acknowledgements	90
5.6	References	90
6	Future Work.....	98
6.1	Precursor selection and process optimization	98
6.2	Characterization of films	99
6.3	Education.....	99
A	Copyright documentation.....	101

List of Figures

Figure 2.1: Large 3-D printed support showing casing for stepper motor, microcontroller and driver boards and two M8 screws.	5
Figure 2.2: Small 3-D printed support structure showing bearing in blue and two M8 threaded rods in red.....	5
Figure 2.3: 3-D printed cover showing slots for power supply and USB cables.....	6
Figure 2.4: 3-D printed major platform showing pivots and casing for stepper motor	6
Figure 2.5: 3-D printed minor platform showing pivots and slots for latches.....	7
Figure 2.6: 3-D printed holder showing slots for latches.....	7
Figure 2.7: 3-D printed latches to fasten cover to minor platform.	8
Figure 2.8: 3-D printed mount base used as the foundation for mount arms.....	8
Figure 2.9: 3-D printed mount arm used to hold the fiber optic cable.....	8
Figure 2.10: 3-D printed fiber optic aligner is used to fasten the fiber optic cables.....	9
Figure 2.11: Schematic showing assembly of all 3-D printed parts. The sample stage, motor and circuit assembly parts were constructed before joining them to the supporting fiber optic alignment components.....	9
Figure 2.12: Schematic showing placement of the open source dual axis gimbal system equidistant from a fiber optic light source and detector. The axes of rotation are also shown. The optical path is highlighted in red.....	11
Figure 2.13: Circuit schematic of open source gimbal system showing interconnects between Arduino microcontroller, power supply and drivers.	12
Figure 2.14: Flowchart showing logic used by the microcontroller to move the major and minor platforms on y and x axes respectively.	14
Figure 2.15: Schematic of the system used for calculating physical angle. The laser mounted on the gimbal system is represented by the red dot with the red dotted line representing the path of the laser beam. The laser beam was at an angle of 0° from the base for this test.....	16
Figure 2.16: Open source gimbal system used for transmission measurement. A set of aligned fiber optic cables is seen with a sample mounted on the rotating gimbal stage. The fiber optic cables are secured with cable ties as shown.....	17
Figure 2.17: Angular dependence of transmission through a glass sample between $(x,y) = 0$ to 60° . Note that the transmission is only shown from 40% to 100%. The lowest recorded value of transmission in the 0 - 60° range was 42%.....	18
Figure 2.18: Unidirectional accuracy of the gimbal system with movement in x direction while holding y constant was found to be the least of all test cases. The root mean squared error value of all points was calculated. It was found to be the highest when x was moved from 40° to 50° with y constant at 0° . Interestingly the same	

high value of error was recorded when the x axis motor was moved in the reverse direction from 50° to 40° with y constant at 0°.	19
Figure 2.19: Repeatability was highest during the movement of y in the forward direction with x held constant. The RMS error recorded in this case was the least at 0.3950. The least repeatable condition was the movement of x when y is held constant (RMS = 1.5850).	20
Figure 2.20: Backlash analysis yielded lowest error when a final position of 0° was approached by y with x held constant. In contrast, the highest error was recorded when x was moved to a final position of 50°. The top and bottom of the error bar represents the error in forward and reverse movement respectively. Hence the size of the error bar represents total backlash.	21
Figure 2.21: The shaded area represents the allowed motion of motors in both x and y directions while keeping adequate intensity at the detector for optical measurements. While angular limitation in the y direction is -180° to 180°, it is -45° to 45° in the x direction.	22
Figure 3.1: (a) Modified load lock of MBE system showing sample heater, polymer sample and RGA. (b) 3-D printed 30 mm × 30 mm × 1 mm plastic samples were placed on a silicon wafer inside the ALD chamber. The yellow lines mark the locations where the ALD AlOx film thickness and density were measured with XRR. The thickness of the AlOx film was also mapped across the whole monitor wafer with ellipsometry.	38
Figure 3.2: Photographs and ellipsometry maps of the monitor wafer after each sequential (I-III) ALD run for ABS and PC. The thickness maps close to the plastic sample position are not accurate because of uncontrolled film deposition. The non-uniformity of the deposition is clear in both photos and ellipsometer maps. The thickness scale [nm] is on the right of each map.	40
Figure 3.3: SEM micrographs of cryo-fractured cross-sections of uncoated 3-D printed (a) ABS and (b) PC, showing porous structures.	41
Figure 3.4: Cryo-fractured cross-section of 3-D printed PC sample, coated with the commercial vacuum resin. The image shows partial penetration of the resin into the pores of the plastic. Pore size was smaller close the surface of the sample than in the bulk. (b) PC surface showing cracks in the vacuum resin. (c) Accumulation of resin on the PC surface with the inset showing a magnified view of resin clusters.	41
Figure 3.5: SEM image of (a) PC ALD coating (BSE image), (b) inset image of hole in PC ALD coating, (c) ABS ALD coating (BSE image), (d) inset image of hole in ABS ALD coating.	42
Figure 3.6: SEM image of a strand of PC, coated with 900 cycles of AlOx. Instead of growing as a uniform film, the AlOx had accumulated on the plastic surface as micron-sized particles and whiskers.	43

Figure 3.7: Backscattered SEM cross section images of (a) black ABS with ALD coating and (b) black PC ALD coating. Note the presence of sub-surface AlOx crystallites, identified via EDS. An example EDS line scan path is presented in the sub-set image for the black ABS image.....43

Figure 3.8: Depth profiles of C, O, and Al K α signal from EDS line scan (left: black ABS, right: black PC). Depth measured as linear distance from the maximum Al K α signal position (assumed to be the centreline of the AlOx coating). Line scans were taken with an accelerating voltage of 15 kV and each elemental K α profile is normalized to the maximum intensity within the sampling length.....44

Figure 3.9: Sum of the normalized partial pressures for each temperature for (a) ABS and (b) PC. Due to a high amount of outgassing from samples with the resin, the outgassing could not be measured at all temperatures with limits indicated with dashed lines. Estimate for the pressure that was too high for the RGA measurement is indicated in the graphs as the grey area. The outgassing from the ALD-coated samples remained low throughout the studied temperature range. The acceptable partial pressure value is determined by the end user’s application.....45

Figure 3.10: A comparison of outgassing characteristics of coated ABS (a) and PC (b) samples at molecular masses 1 to 100 AMU at 50 °C, showing a consistently low value for the ALD-coated samples.46

Figure 4.1: Ellipsometry maps showing thickness of AlOx on sequential monitor wafers. The thickness scale (in nm) is represented as a color bar on the right of each map. The square in the middle of each map represents the location of the plastic sample. It is observed that the thickness around the plastic sample is non-uniform due to uncontrolled deposition. The targeted thickness on silicon for each run was 50 nm.60

Figure 4.2: SEM image of macropores seen in PC. These are indicative of print lines. ..61

Figure 4.3: SE SEM cross section images of ALD-coated polymer samples: (a) PC (x10k), (b) ABS (x30k), and (c) PP (x2.5k); (d) shows the ALD coating on the surface of the PP sample62

Figure 4.4: Surface accumulation of AlOx in the form of particles are seen in (a) PC (b) ABS and (c) PP.63

Figure 4.5: BSE SEM cross section images of ALD-coated polymer samples: (a) PC, (b) ABS and (c) PP. Note that all images are at magnification of x3.5k.....64

Figure 4.6: EDS depth profiles for Al K α for ALD-coated 3-D printed polymer samples65

Figure 4.7: Sum of normalized partial pressures at all measured temperatures for (a) PC, (b) ABS, (c) PP. The vertical dashed lines indicate temperature setpoints after which partial pressure could not be measured without damaging equipment. The grey area represents a region of high outgassing where data collection is not possible with the RGA used in this study.66

Figure 4.8: Outgassing characteristics of clear PC (a), ABS (b) and PP (c) at molecular masses 1 to 100 at 60°. A consistently low value of normalized partial pressure was seen for all ALD coated samples.	68
Figure 5.1: EDS depth profiles for Al K α for clear and black ALD-coated 3-D printed polymer samples. 0 μ m represents the alumina oxide/polymer interface.	79
Figure 5.2: Porosity seen in a cross section of clear (left) and black (right) ABS. These large porous spaces allow precursor flow into the bulk of the plastic.	81
Figure 5.3: Vacuum outgassing characteristics of all black and clear samples showing the lowest recorded outgassing for ALD coated samples.	82
Figure 5.4: FTIR spectral comparison of black and unpigmented ABS and PC.	84
Figure 5.5: XPS spectra of black and clear a) PC and b) ABS samples. All samples showed Si contamination likely due to a contaminated ALD deposition chamber.	85
Figure 5.6: XRD spectra of all 3-D printed samples (inset) showing degree of crystallinity.	86
Figure 5.7: FTIR spectral comparison of pure polypropylene and commercial polypropylene filament shows additional carbon in pure PP. 3-D printed pure PP using a bespoke syringe printer setup shows soft and crumbly texture. This is compared against a similar sample printed using commercial filament.	88
Figure 5.8: XPS spectra comparing pure PP to filament PP. The samples showed both sodium and silicon contamination.	89

List of Tables

Table 2.1: Customized 3-D printable parts for the open source dual axis Gimbal system.	10
Table 2.2: Commercially available parts for the open source dual axis Gimbal system ..	11
Table 2.3: Comparison of available gimbal systems compared to the open source gimbal system for accuracy, micro step size, repeatability and cost.	24
Table 3.1: Essential printing parameters of the ABS and PC samples, defined using the Cura software.	35
Table 3.2: Sample types and methods of pre-treatment. All samples were prepared for both ABS and PC.	36
Table 4.1: The printing parameters used to 3-D print the ABS, PC, and PP samples.	57
Table 5.1: Comparison of Tg, porosity, crystallinity, and TMA diffusion depth and AlOx coating thickness. Note that diffusion depth is defined as the sub-surface depth at which the normalized Al K α signal was measured to be less than 0.1.	86

Author Contribution Statement

This dissertation is comprised of four manuscripts. The authors' contributions are described below.

Chapter 2 is reproduced from “Bihari, N., Dash, S.P., Dhankani, K.C. and Pearce, J.M., 2018. 3-D printable open source dual axis gimbal system for optoelectronic measurements. *Mechatronics*, 56, pp.175-187,” with the permission of Elsevier.

Nupur Bihari: Data curation, Formal analysis, Investigation, Methodology, Validation, Visualization, Writing - original draft, Writing - review & editing.

Chapter 3 is reproduced from “Heikkinen, I.T., Marin, G., Bihari, N., Ekstrum, C., Mayville, P.J., Fei, Y., Hu, Y.H., Karppinen, M., Savin, H. and Pearce, J.M., 2020. Atomic layer deposited aluminum oxide mitigates outgassing from fused filament fabrication-based 3-D printed components. *Surface and Coatings Technology*, 386, p.125459,” with the permission of Elsevier.

Nupur Bihari: Data curation, Formal analysis, Investigation, Methodology, Validation, Visualization, Writing - original draft, Writing - review & editing.

Chapter 4 is reproduced from “Bihari, N., Heikkinen, I.T., Marin, G., Ekstrum, C., Mayville, P.J., Oberloier, S., Savin, H., Karppinen, M. and Pearce, J.M., 2020. Vacuum outgassing characteristics of unpigmented 3D printed polymers coated with atomic layer deposited alumina. *Journal of Vacuum Science & Technology A: Vacuum, Surfaces, and Films*, 38(5), p.053204,” with the permission of AIP Publishing.

Nupur Bihari: Data curation, Formal analysis, Investigation, Methodology, Validation, Visualization, Writing - original draft, Writing - review & editing.

Chapter 5 will be submitted for peer review as “Bihari, N., Heikkinen, I.T., Marin, G., Ekstrum, C., de Alwis, C., Mayville, P.J., Perrine, K.A., Savin, H., Karppinen, M. and Pearce, J.M., 2021. Understanding the multilevel phenomena that enables inorganic atomic layer deposition to provide barrier coatings for highly-porous 3-D printed plastic in ultra-high vacuums.”

Nupur Bihari: Data curation, Formal analysis, Investigation, Methodology, Validation, Visualization, Writing - original draft, Writing - review & editing.

Acknowledgements

I am immensely grateful to my advisor Dr. Joshua Pearce for believing in me and allowing me to develop as an independent researcher. He provided me with an opportunity that enabled me to work on multiple research projects and learn from experts in different fields. From him, I learnt to value original ideas, the power of collaboration and a willingness to always believe in possibilities. I hope to be able to impart the same love for research to my future mentees someday.

Dr. Bergstrom taught me everything I know about semiconductor micro/nano fabrication. The background he familiarized me with enabled me to envision what processing equipment could look like in the future. The many hours spent troubleshooting at Michigan Tech's Microfabrication Facility with Dr. Bergstrom and Dr. Chito Kendrick have been invaluable learning experiences.

I appreciate the efforts of Chathura de Alwis, Dr. Kathryn Perrine and Dr. Timothy Leftwich who have always gone out of their way to help design, run experiments and collaborate on various surface science techniques. Yuhuan Fei and Dr. Yun Hang Hu are cherished collaborators and co-authors.

I thank Dr. Hackney for teaching me how to be a "materials scientist" – thinking in terms of structure-property interactions to better understand my experimental results.

I have caused Owen Mills, Paul Fraley, Mark Sloat, Mike Chase and Mike Myllyoja more than my fair share of trouble, but they always responded with smiles and words of encouragement and advice. I am still learning patience and an attention to detail from them.

I wish my collaborators from Aalto University, Finland the best in everything they do. I am hoping our paths will cross again in the future. My colleagues at Michigan Tech's Open Sustainability Technology Lab have been the best team I could have hoped for. We have made many memories together and they have always been kind, enthusiastic and willing to give the project all that it takes and more.

I thank my family for their support; teaching me tenacity and bravery when faced with the unexpected. Rick Stanitis, Bobby Escobar and the team at Canterbury House have been my home away from home. I have immense love and adoration for Dr. Junying Li who has been a mother to me in Houghton. Jenny Lester and Copper Country Senior Meals gave me friendship and purpose during the pandemic. Dr. Kishan Bellur's constant partnership is something I hope to cherish for a lifetime.

I thank Michigan Tech Recreation, City of Hancock and the many wonderful people of the Keweenaw who help maintain beautiful trail systems and allow me to hike and forage on their lands.

Lastly, I wish to thank Michigan Technological University's Department of Materials Science and Engineering, the Finishing Fellowship and the Richard Witte endowment for financial support.

Abstract

While hardware innovations in micro/nano electronics and photonics are heavily patented, the rise of the open-source movement has significantly shifted focus to the importance of obtaining low-cost, functional and easily modifiable research equipment. This dissertation provides a foundation of open source development of equipment to aid in the micro/nano electronics and photonics fields. First, the massive acceptance of the open source Arduino microcontroller has aided in the development of control systems with a wide variety of uses. Here it is used for the development of an open-source dual axis gimbal system. This system is used to characterize optoelectronic properties of thin transparent films at varying angles. The use of open source hardware is not limited to characterization, it can also be used for fabrication in these fields. Conventionally, the ubiquity of vacuum systems in semiconductor fabrication has precluded the development of an open-source development in the “fab” environment and thus has high foundational and operational costs. In order to make vacuum systems and their components cost-effective in a research environment there has been a paradigm shift towards refurbishing and repairing instead of replacing legacy systems. These legacy systems are built and operate on the principle that the vacuum industry is a small industry, and hence only a small number of sizes and types of parts may be used to reduce costs. The assumption that the vacuum industry is a small industry is no longer valid. The semiconductor industry alone, which is a subset of the vacuum industry, was worth over USD 481b and increasing. Hence, there is a need to not only introduce new methods, but also new materials that make up these systems. Additive manufacturing is a low-waste, low-capital cost way to make custom equipment. The most popular materials used in additive manufacturing processes are polymer blends. 3-D printing using Fused Filament Fabrication (FFF) methods has been used to create custom objects for laboratories. However, the use of polymer-based materials is conspicuously absent in the development of vacuum systems, especially those that are used for semiconductor fabrication. There are two major problems identified when polymeric materials are used to make vacuum systems: finding a way to prevent outgassing (which can subsequently lead to contamination), and sealing them so that they can hold a vacuum. This work has demonstrated how an inorganic barrier layer introduced via Atomic Layer Deposition (ALD) can alleviate outgassing to a large extent under high vacuum levels (1E-6 to 1E-7 torr). Recognizing the importance of ALD alumina in back end of the line (BEOL) semiconductor processing, films were deposited on 3-D printed polymer-based substrates with differing constituents. These samples were tested in a bespoke gas analysis chamber for outgassing characterization. Surface and bulk characterization was completed using various tools such as scanning electron microscopy (SEM), energy dispersive x-ray analysis (EDX), x-ray photoelectron spectroscopy (XPS), and attenuated total reflectance - Fourier transform infrared spectroscopy (ATR-FTIR). Additionally, spectroscopic ellipsometry (SE) was used to understand how the concept of thickness of a film deposited on a porous polymer-based sample does not correlate directly with its conventional definition. Also, an effort is made to understand the mechanism of ALD alumina deposition on porous plastic surfaces. It was concluded that this deposition is a complex amalgamation of physical and chemical properties of both the polymer and the precursor gases. Finally, recommendations are made for AM materials to be used in vacuum systems.

1 Introduction

Additive manufacturing (AM) is a minimal-waste, low cost method of manufacturing customizable equipment. Pieces of equipment are typically 3-D printed in-house leading to reduced transportation costs, both monetary and environmental. In addition, whenever a repair or a replacement part is needed, the lead-time is only as long as the design and printing may take. These bespoke tools have now been employed at various industrial and educational institutions. The open source movement in particular has led to unprecedented growth in their acceptance across industries. Despite their widespread growth in scientific research, they remain conspicuously absent from semiconductor microfabrication environments. This is due to the fact that polymer-based materials are predominantly used for 3-D printing and are considered incompatible with the microfabrication process flow. These materials are typically not pure substances and have a wide range of molecular weights of the same compound, as well as many additives (fixers, primers, plasticizers, colorants, etc.). In the presence of a heat or pressure gradient, these materials outgas – a process in which the lower molecular mass entities exit the polymeric matrix. This leads to contamination of the environment these parts are housed in, and affects their mechanical strength. Their acceptance in the semiconductor manufacturing arena could be enhanced if their outgassing could be reduced or eliminated. If these parts were to be coated with a material that behaves as a barrier, then the lower molecular mass entities would not have a way to leave the polymer matrix thus resulting in much lower outgassing. Atomic layer deposition (ALD) is used as a method to coat these materials and hence lower their outgassing. This thesis describes both bulk and surface characterization of such coatings. An attempt has been made to discuss the special challenges plastics materials pose on ALD due to their porosity, chemical nature and moisture retention.

1.1 Outline

Chapter 2 describes a 3-D printed dual axis gimbal system that is used to study the angle dependence of spectroscopic properties of thin films. This tool was developed to characterize thin films for far less capital costs than proprietary systems. It introduces the concept of 3-D printing open source scientific hardware in a modular way. It also describes the design process, electronic design and touches upon a cost comparison against commercial equipment. This model of development can be extended into the future for 3-D printed plastic equipment if outgassing and sealing can be accomplished, which are the topics of the remaining Chapters.

Chapter 3 delves into the material selection for building open source plastic-based vacuum systems. It introduces two different coatings used to insulate 3-D printed parts – a commercial sealant and an ALD coating. Here only black pigmented plastics were examined as a “worst case scenario”. Black pigmented plastics often use carbon black as the colorant, which outgasses when exposed to a vacuum. A number of surface and bulk characterization methods were used to determine that ALD coatings fared better under very high vacuum (VHV) as compared to the commercial sealant. The vacuum

compatibility tests on these plastic samples when coated with an ALD layer prove that these coatings form an effective barrier layer.

Although black colored plastics could potentially be used to build vacuum systems and components, as long as they are coated with an ALD layer, an effort was made to study clear, unpigmented plastics, as these would be the materials of choice due to lower probabilities of contamination. Chapter 4 describes three such materials: polycarbonate (PC), polypropylene (PP) and acrylonitrile butadiene styrene (ABS). The effect of barrier coatings was studied and ALD coated PP was chosen as the material of choice to build the vacuum system.

With a number of surface and bulk characterization tests used on both black pigmented and unpigmented plastics, many differences in their behavior when exposed to a vacuum were uncovered. The results of these tests are described in Chapter 5 and an effort is made to develop a more complete scientific understanding of their vacuum behavior. Chapter 6 includes recommendations for films and plastics for use in a future plastic based vacuum system.

This dissertation describes many of the insights on vacuum compatibility of ALD-coated plastic and characterization techniques utilized during the process. This proof of concept study not only shows that plastic based materials can be used in a clean, vacuum environment, but they could potentially be used to form semiconductor compatible tooling.

2 3D Printable Open Source Dual Axis Gimbal System for Optoelectronics Measurements

2.1 Introduction

A high level of modularization [1] in open technology development allows for collaboration in a way that knowledge is efficiently shared by many [2,3]. Free and open source technological development also decreases ambiguity and makes information freely available to a large group of developers [4-6]. This promotes the sharing of knowledge among researchers in dissimilar fields [7], which has led to a number of success stories, notably Linux [8,9] and the rise of free and open source software (FOSS) movement [10-11]. The motivation for development is high when assistance from skilled developers is available [12,13] and the results are favorable [14-18]. Thus, FOSS is now also well established in mechatronics [19-21]. The success of FOSS has encouraged hardware developers to adopt this model as well [22-24]. Free and open source hardware (FOSH) development has seen success with a number of projects including the popularity of accessible microcontrollers such as the Arduino [25], which has been rapidly adopted by researchers in industry and academia [26] for ease of use, high modularization [27], and affordable cost [28-30].

Arduino microcontrollers have been used wearable textile ‘e-clothing’ with embedded sensors [31-33], complex communication systems for microgrids [34], educational tools [35] such as a mechatronics project based on 3-D printing [36] and home automation control systems [37-39]. Most useful to scientists, Arduino microcontrollers are being used to automate mechatronic equipment in the lab [27,40] including a number of wireless sensor networks [41], air pollution monitoring and control system [42], data sharing and environmental monitoring [43,44], oceanographic sensor and actuator control systems [45-47] and have repeatedly proven that a low cost open source platform has the capability to perform equally well as compared to sophisticated expensive systems [27,40,48]. Other mechatronics equipment including quadrotors [49], robot fish [50], and mobile wheeled robots [51] have been developed using Arduino. It is being used as a teaching tool at the undergraduate level in mechatronics laboratories [52] and for developing low-cost educational material [53,54].

The development of open source 3-D printing in the RepRap project [55] has emerged as one of the primary mechanisms driving FOSH development as the digital designs for 3-D printing can themselves be open sourced [56]. In addition to educational opportunities [57-59], rapid prototyping using 3-D printing has reduced the cost of commonly used scientific equipment while allowing faster development [27,40,60,61]. Much modern experimental scientific research requires expensive equipment that has high maintenance costs. With 3-D printed equipment, this maintenance cost is reduced significantly since most parts can be printed and replaced internally. The plethora of repositories (e.g. NIH 3D Printer Exchange [62], Youmagine [63], MyMiniFactory [64], GrabCAD [65], Thingiverse [66], etc.) available with CAD models of various parts enables low-cost and relatively easy

distributed production by consumers [67] and adopted by scientists [40]. One area that is benefiting from 3-D printing is optics with 3-D printed embedded optical elements and interactive devices [68], curved displays [69], phantoms for whole animal optical imaging [70], spectral system for collagen fluorescence lifetime measurements [71], flexure translation stage for open-source microscopy [72], smart phone microscope adapters [73], a 3-D microscope stage [74] and a large customizable library of mechanical components for optics setups [75]. While open source 3-D printing has seen wide acceptance in biology and optics, it remains conspicuously absent from the semiconductor arena. The solar photovoltaic industry in particular relies on reduced costs and quick manufacturing. There is a need to further develop this low-cost open source technology to characterize thin film anti-reflective coatings and transparent conducting oxides (TCO) for the glass, mirror and solar photovoltaic industry [76,77] whose transmission properties are angle dependent [78-79]. The angular and spectral dependence of reflectivity and transmissivity of a material are important parameters that need to be studied for x-ray and other spectroscopic analyses [80]. A gimbal system is often used to rotate the sample in axes to study this angular dependence of optical and optoelectronic properties.

In order to fulfil this research need, a novel low-cost 3-D printable open source dual axis gimbal system is presented in this study. The motivation for this study is to determine if a 3-D printed open hardware system, which reuses component designs from other applications is adequate to perform as an optoelectronic measurement aid while eliminating precision machining used in commercial systems, reducing equipment capital costs, allowing complete control by the user in order to make modifications and meet the needs of custom applications. In the design an Arduino based microcontroller is used to move the sample holder to the user specified angle where two stepper motors control the motion providing two degrees of freedom. The sample holder is made in such a way that sample glass slides can easily be mounted on it by two movable latches. The system was validated and characterized for: i) unidirectional accuracy, ii) repeatability, iii) backlash, iv) speed resolution and v) microstep size. Finally, the mechatronic system is tested for the intended application using a halogen light source and a spectrometer to measure transmission through glass TCO samples through a hemisphere. The results are discussed in the context of the development of open source mechatronic equipment for laboratory use.

2.2 Materials and methods

The design methodology used for this device uses an FOSH optimization model previously described [81], which encompasses six design principles: design involving the principles of use of a free and open-source tool chain, minimize the number and type of parts and the complexity of the tools, minimize the amount of material and the cost of production, maximize the use of components that can be 3-D printed, create parametric designs to enable design customization and use of off-the-shelf parts, which are readily available throughout the world. Following these design principles, here, a gimbal system that can automatically test a range of custom angles in an x and y axis for use in optical thin film

characterization is described. This system was found to have a microstep size of less than 1 degree and repeatability and backlash error of less than 2 degrees.

2.2.1 Mechanical Architecture

The 3-D printed parts were all designed in parametric CAD for ease of customization and to be easily 3-D printed on low-cost desktop 3-D printers include:

1. The large support structure (**Figure 2.1**) has housing for a stepper motor, Adafruit Trinket Pro microcontroller board and the driver boards for the stepper motor. It also includes space for two M8 screws that ensure perfect alignment between the large and small support structures.



Figure 2.1: Large 3-D printed support showing casing for stepper motor, microcontroller and driver boards and two M8 screws.

2. The small support structure (**Figure 2.2**) does not contain any electronics but ensures that the structure remains flat at all times. It also has the pivot for the y-axis of the gimbal.

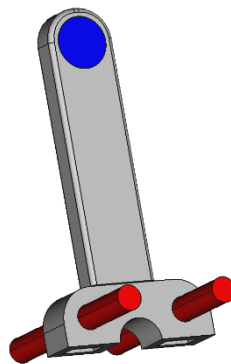


Figure 2.2: Small 3-D printed support structure showing bearing in blue and two M8 threaded rods in red.

3. The 3-D printed cover (**Figure 2.3**) is used to enclose all electronics inside the large support structure. It has two openings for power supply and USB cables.

Having a cover ensures correctly connected wires and protects the electronics from the environment.

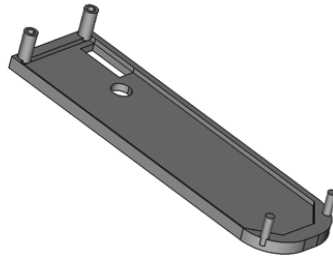


Figure 2.3: 3-D printed cover showing slots for power supply and USB cables

4. The major platform is the y-axis of the gimbal system shown in **Figure 2.4**. This has two pivots that can be attached to the large and small support structures. This also has housing for a stepper motor.



Figure 2.4: 3-D printed major platform showing pivots and casing for stepper motor

5. The minor platform is the x-axis of the gimbal system and is shown in **Figure 2.5**. This has pivots that can be attached to the larger and smaller support structures. This part is also the sample holder and includes slots for fastening the sample latch. Although the design is parametric and can be customized, the current platform holds samples 75mm x 60mm or smaller.

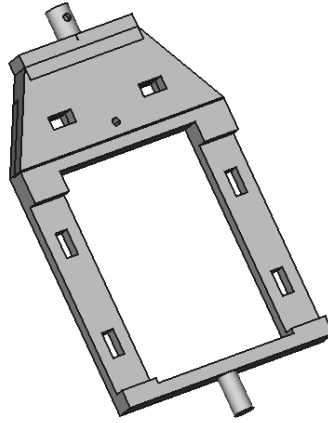


Figure 2.5: 3-D printed minor platform showing pivots and slots for latches

6. The holder latches (**Figure 2.6**) onto the minor platform and provides a stable surface for the sample. This holder as designed in its current dimensions can be used for two plain standard microscope glass slides (25mm x 76mm).

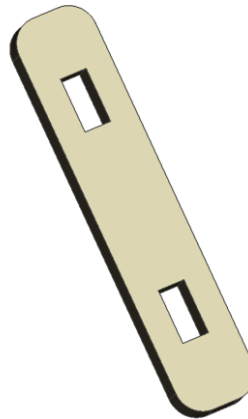


Figure 2.6: 3-D printed holder showing slots for latches

7. The 3-D printed latches (**Figure 2.7**) can be used to fasten the holder to the minor platform. These ensure that the sample stays flat and stationary during the measurement.

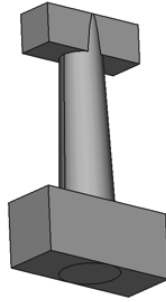


Figure 2.7: 3-D printed latches to fasten cover to minor platform.

8. Mount base (**Figure 2.8**) is used as the foundation on which the alignment apparatus is fixed. This forms the basis of the support structure for fiber optic cables.



Figure 2.8: 3-D printed mount base used as the foundation for mount arms.

9. Mount arm (**Figure 2.9**) is 3-D printed to the correct height for the fiber optic cable. This is fixed on opposite ends of the mount base. The gap allows the user to change the height of the aligner, and thus the cables.

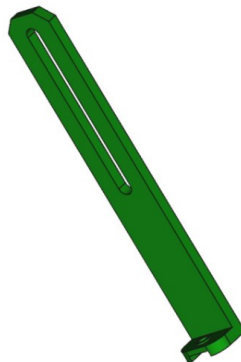


Figure 2.9: 3-D printed mount arm used to hold the fiber optic cable.

10. Fiber optic aligner (**Figure 2.10**) is used to ensure that the fiber optic cables lay flat and the transmitting and the receiving end are always 180° from each other.



Figure 2.10: 3-D printed fiber optic aligner is used to fasten the fiber optic cables.

The assembly of these parts is demonstrated in **Figure 2.11**.

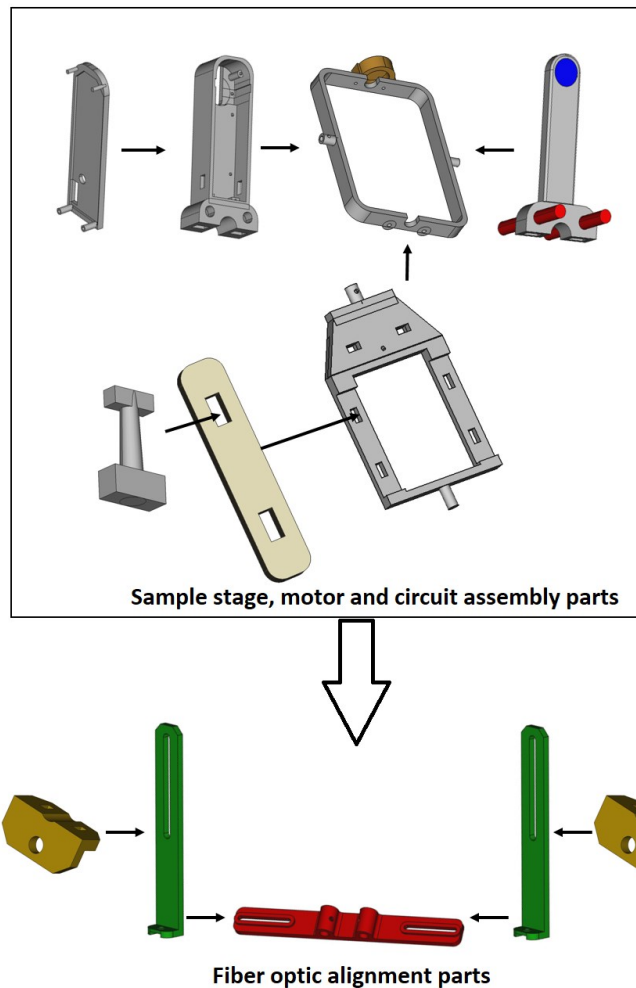


Figure 2.11: Schematic showing assembly of all 3-D printed parts. The sample stage, motor and circuit assembly parts were constructed before joining them to the supporting fiber optic alignment components.

The complete bill of materials (BOM) is available with design files used to print various parts of the gimbal system [82]. This BOM can be classified into two categories: 3-D printable parts (**Table 2.1**) and commercially available hardware (**Table 2.2**). All custom parts were designed using version 0.15 of FreeCAD [83], an open source parametric 3-D CAD modeler. These parts were designed parametrically and can be customized easily by the user. Polylactic acid (PLA) filament purchased commercially [84] was used with an open source delta style RepRap 3-D printer [85], which was controlled by the open source Franklin 3-D printer controller [86]. However, any hard thermoplastic can be used on any fused filament fabrication (FFF)–based desktop 3-D printer. The expected operating environment was indoor laboratory space with an ambient temperature between 20°C and 25°C. Thermal expansion of 3-D printing polymer was thus not taken into consideration while determining part dimensions. A tolerance of 0.1mm was used to ensure parts fit snugly without the possibility of cracking or loosening. The price of a 1kg PLA filament spool on November 17, 2017 was used for the cost analysis. Off-the-shelf parts were procured from Amazon.com or similar.

Table 2.1: Customized 3-D printable parts for the open source dual axis Gimbal system.

	Part	Quantity	PLA Mass (g) (15% infill)	Cost (USD)
1	Large Support	1	22	0.64
2	Small Support	1	38	1.10
3	Cover	1	18	0.52
4	Major Platform	1	38	1.10
5	Minor Platform	1	38	1.10
6	Holder	1	6	0.17
7	Latch	2	2	0.12
8	Mount Base	1	32	0.93
9	Mount Arm	2	20	1.16
10	Fiber Optic Aligner	2	2	0.12
	Total			6.96

Table 2.2: Commercially available parts for the open source dual axis Gimbal system

	Component	Quantity	Cost (\$)	Source
1	Bearing (Roller skates bearing: O.D = 21mm and I.D = 8mm)	2	2.90	Hardware Store
2	5V Stepper Motor and Driver	2	5.60	Amazon.com*
3	Adafruit Pro Trinket 5V Microcontroller	1	9.95	Amazon.com*
4	5/16" (or M8) screw 195mm	2	2.80	Hardware Store
5	5/16" (or M8) nuts	6	0.60	Hardware Store
6	5V DC Supply Adaptor	1	10.99	Amazon.com*
7	5.5mm Jack Connector Socket	1	1.03	Amazon.com*
8	M5 Socket Head Bolt 16mm	4	0.48	Hardware Store
9	M5 Steel Hex Nut	4	0.07	Hardware Store
10	M3 Heat Set Insert	2	0.25	Hardware Store
11	M3 Socket Head Screw	2	0.14	Hardware Store
12	8" Cable Tie	2	0.06	Hardware Store
	Total		34.87	

As can be seen from the sum total of the BOM from Tables 1 and 2 the total hardware cost is USD \$41.83. It should be noted that the cost of PLA filament has been reduced recently and this should be viewed as an upper cost limit.

The assembled gimbal system was then set up between a fiber optic light source and detector as shown in **Figure 2.12**.

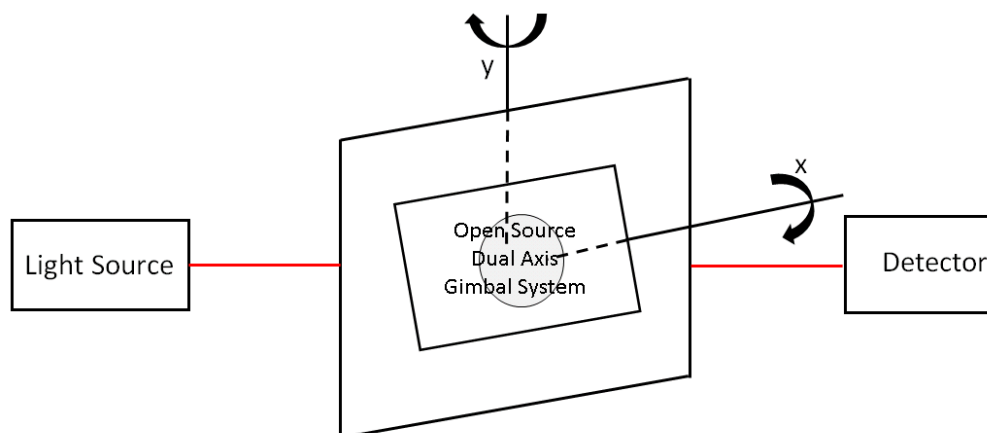


Figure 2.12: Schematic showing placement of the open source dual axis gimbal system equidistant from a fiber optic light source and detector. The axes of rotation are also shown. The optical path is highlighted in red.

2.2.2 Electronic Architecture

An Adafruit Trinket Pro 5V 16MHz with ATmega328 common core Arduino chip was obtained from Adafruit Industries. This development board features micro-USB jack that was used for uploading the program to the system memory. Two Elegoo 28BY J-48 ULN2003 5V stepper motors were used to move the major and minor platforms in y and x axes respectively. Two ULN2003 driver boards for Arduino were used to control these stepper motors. The circuit schematic is shown in **Figure 2.13**.

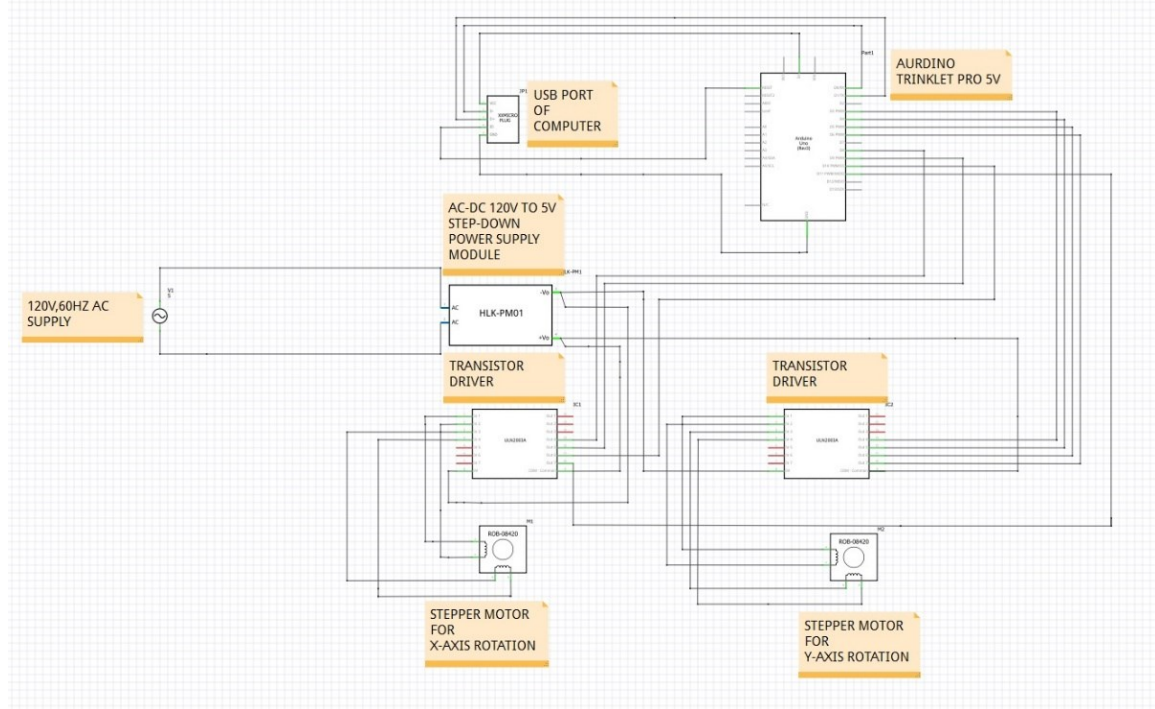


Figure 2.13: Circuit schematic of open source gimbal system showing interconnects between Arduino microcontroller, power supply and drivers.

2.2.3 Software Architecture

The system runs on a sketch file written for Adafruit Trinket Pro 5V and available on the Open Science Framework [82]. The user is prompted to choose a terminal x-y coordinate or a trace between the initial and the user provided final x-y coordinates. The tracing feature moves in steps of ten degrees. However, this can be easily changed in the code.

Figure 2.14 shows a flowchart describing programming logic and the pseudocode written below describes the stepper motor control.

//Pseudo code for Gimbal system

1. *Initiate device*
2. *Obtain mode of operation (user input: "1" for commanded angle and "2" for trace)*
3. *if mode == 1*
 1. *Obtain desired X axis angle (user input)*

2. *Move stepper in X axis to desired angle*
3. *Update X axis location*
4. *Obtain desired Y axis angle (user input)*
5. *Move stepper in Y axis to desired angle*
6. *Update y axis location*
4. *else if mode == 2*
 1. *Obtain desired target X axis angle (user input)*
 2. *Obtain desired target Y axis angle (user input)*
 3. *Loop Y angle from zero to Y target in specified steps*
 1. *Loop X angle from zero to X target in specified steps*
 1. *Move stepper in Y axis to next angle*
 2. *Update Y axis location*
 3. *Move stepper in X axis to next angle*
 4. *Update X axis location*
5. *else display error (must enter either "1" or "2")*

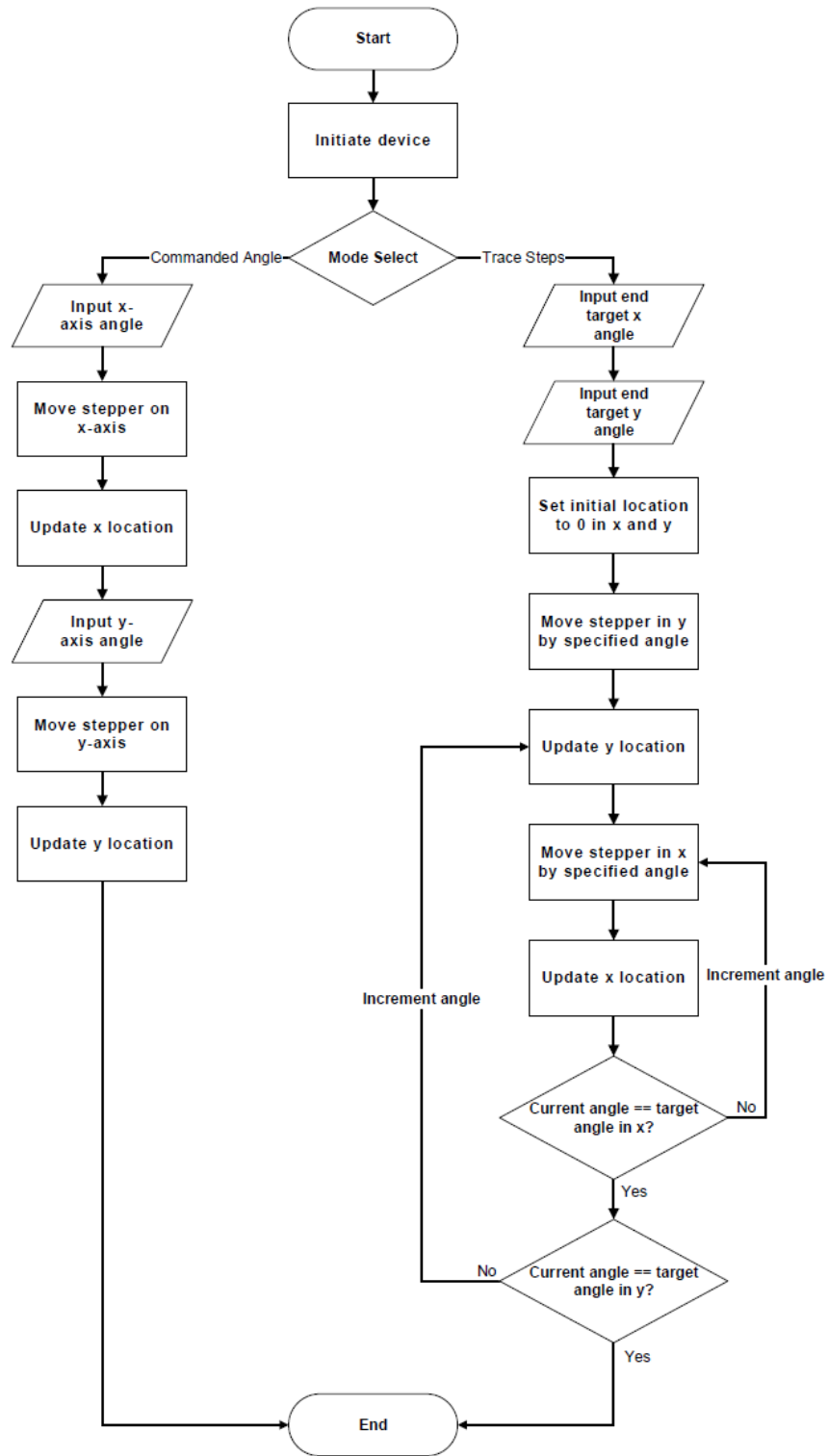


Figure 2.14: Flowchart showing logic used by the microcontroller to move the major and minor platforms on y and x axes respectively.

The intended purpose of this system is to measure angle dependent transmission properties of thin films on glass substrates. This angle dependence can be accurately recorded using any computer running Arduino Integrated Development Environment's (IDE) Serial Monitor [87]. Alternatively, this data can be written to files for platform independent access.

2.3 Validation and Demonstration

The gimbal system was tested using an Ocean Optics DH-2000 UV-VIS-NIR halogen light source. An Ocean Optics QP600-2-VIS-NIR fiber optic patch cable was used with a USB2000+ spectrometer. Spectra Suite was used to collect transmission data over the visible spectrum, from wavelength 400nm to 800nm. Data was collected at angles $[x,y]$: $[0,0]$ to $[60,60]$ in steps of 10 degrees.

25mm x 76mm plain glass microscope slides were obtained from VWR International in a thickness of 1mm. These were cleaned using acetone, 2-propanol and DI water, nitrogen dried, and were mounted on the sample holder of the gimbal system.

The gimbal system was positioned between the light source and the detector such that the source and detector were both equidistant from the sample. This length was kept constant for all measurements. Care was taken to ensure that there were minimal bends in the optical fiber cable, both on the source and the detector side.

There were five major parameters identified for system characterization: 1) unidirectional accuracy, 2) repeatability, 3) backlash, 4) speed resolution and 5) microstep size [88, 89]. These parameters provide characterization metrics needed by users when sourcing a research system. These metrics are used by manufacturers and are part of the standard specification sheets of commercial products with similar functionality and applications.

The unidirectional accuracy was the error in moving between two positions, when approached from the same direction. This was experimentally determined by moving the stepper motor to a commanded angle from two different initial positions and measuring the angle in each case. For repeatability, the same measurement was made six times each in x and y directions and the errors in final positions were calculated [90].

These measurements were made by placing the gimbal system at a chosen distance of 85cm from a wall and using the projection from a laser as shown in Figure 15. The system was rotated to a specified angle after installing a visible laser on it. The distance from the floor to the point on the wall at which the beam was visible was measured using a tape-measure. The inverse tangent of the distances measured was used to calculate the physical angle (Figure 2.15).

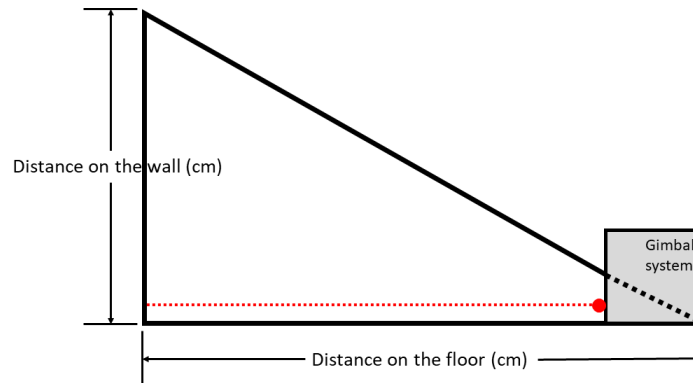


Figure 2.15: Schematic of the system used for calculating physical angle. The laser mounted on the gimbal system is represented by the red dot with the red dotted line representing the path of the laser beam. The laser beam was at an angle of 0° from the base for this test.

Backlash was defined as the maximum error when the same final position is approached from two different directions. This was experimentally determined by commanding the stepper motor to move from two different initial angles to a final angle such that: initial angle 1 > final angle > initial angle 2 [91].

Speed resolution was defined as the smallest incremental change in speed that can be achieved by the system [92]. This was recognized due to its importance in reducing time required to run a set of tests. After moving from an ‘initial angle’ to a ‘final angle’, the user’s need to move to a different angle (final angle + Δ angle) from that ‘final angle’ was seen. The speed at which this incremental change happened was crucial for a given test.

Step and micro-stepping are used to describe stepper motor movement in accordance with the terminology used by component manufacturers. Microstep size is defined as the measured angle divided by the number of states per step allowed by the motor in commanded angle mode. The motors were operated in 8-step sequence with 64 steps per turn [93]. Number of states refers to whether the motor is being operated in full-step mode or half-step mode. In the half-step mode, the motor has 8 states – referring to 8 possible configurations of the transistors. Discussion using states is only made to delineate the stepping pattern. While the “microstep” size is 64 is the number of steps required for a full turn of the motor, the number of steps required for a complete 360 degree rotation of the axes is specified as step size, which is 2048.

2.4 Results

A photograph of the complete open source gimbal system with a TCO sample as used for transmission measurements is shown in **Figure 2.16**. As can be seen in **Figure 2.16**, the system is completely novel compared to commercial counterparts. The open source gimbal system 3-D printed system has no precision-machined metal parts and uses no metal other than fasteners. This enables radical reduction in costs and enables distributed manufacturing and ease of customizability at the expense of characteristics such as unidirectional accuracy and repeatability as quantified below.

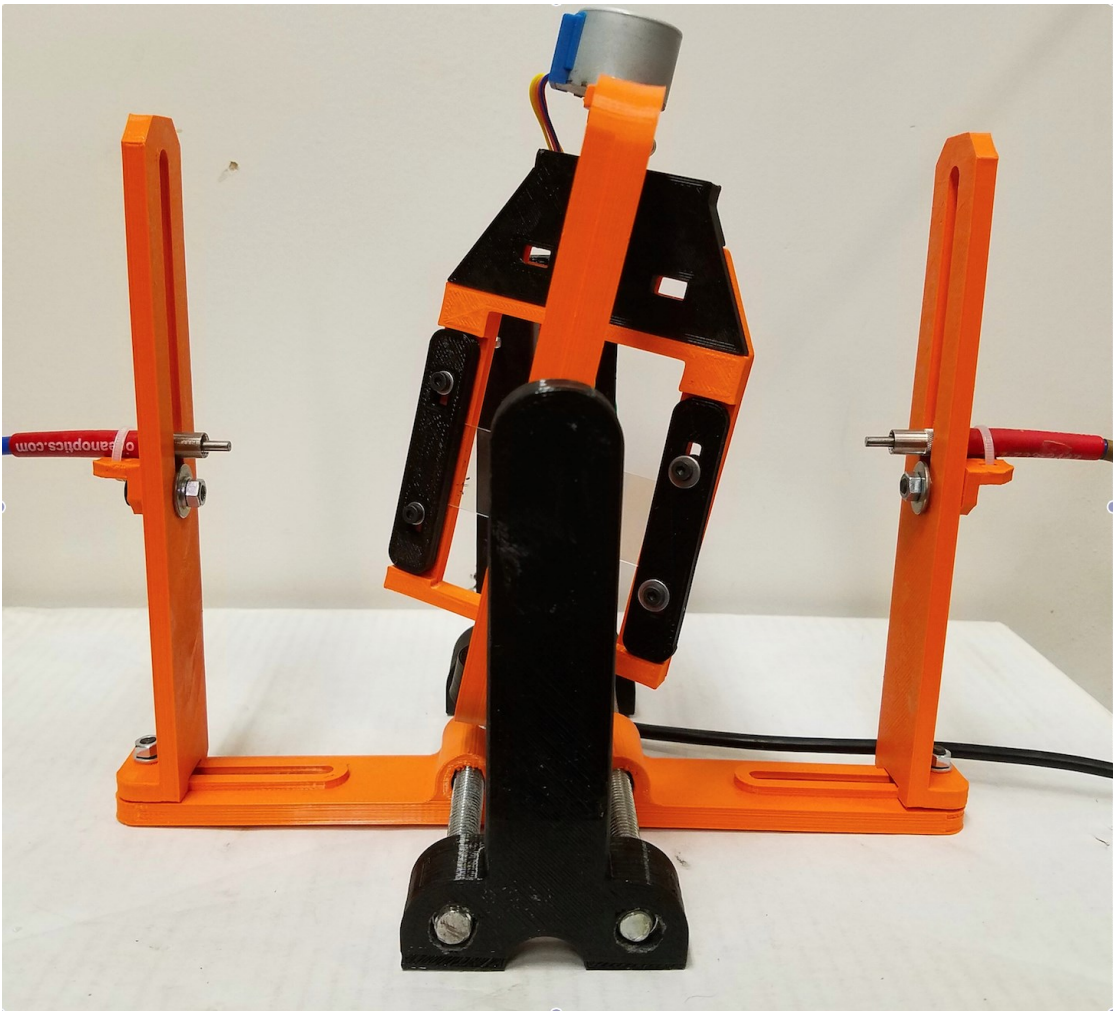


Figure 2.16: Open source gimbal system used for transmission measurement. A set of aligned fiber optic cables is seen with a sample mounted on the rotating gimbal stage. The fiber optic cables are secured with cable ties as shown.

2.4.1 Demonstration of Angular Dependence of Transmission

The angular dependence of transmission could be quantified using the gimbal system by integrating intensity recorded by the detector from 400nm to 800nm. The clear glass sample had a transmission as shown in **Figure 2.17**. This control sample shows a decline in transmission between 30° and 60° (in x) due to partial screening of the light beam by the physical placement of stepper motors. This effect is accounted for in all samples. A smaller percentage of light is transmitted in the 30° to 60° range due to this shading effect. To obtain those equivalent angles the sample can be rotated in the z axis 180° and the same scan run. If the transmittance of a specific point on the sample is desired, appropriate positioning can help, although the error in measurement may be high. Multiple measurements may be made in this angular region to gather statistically significant data. The same final position may also be approached from two different directions in order to get this statistical data while accounting for the backlash error. This shading effect is important to consider when detected intensities are important. However, if only the detection of presence or absence of a bright source of radiation is desired, the gimbal system can be used over its entire angular range.

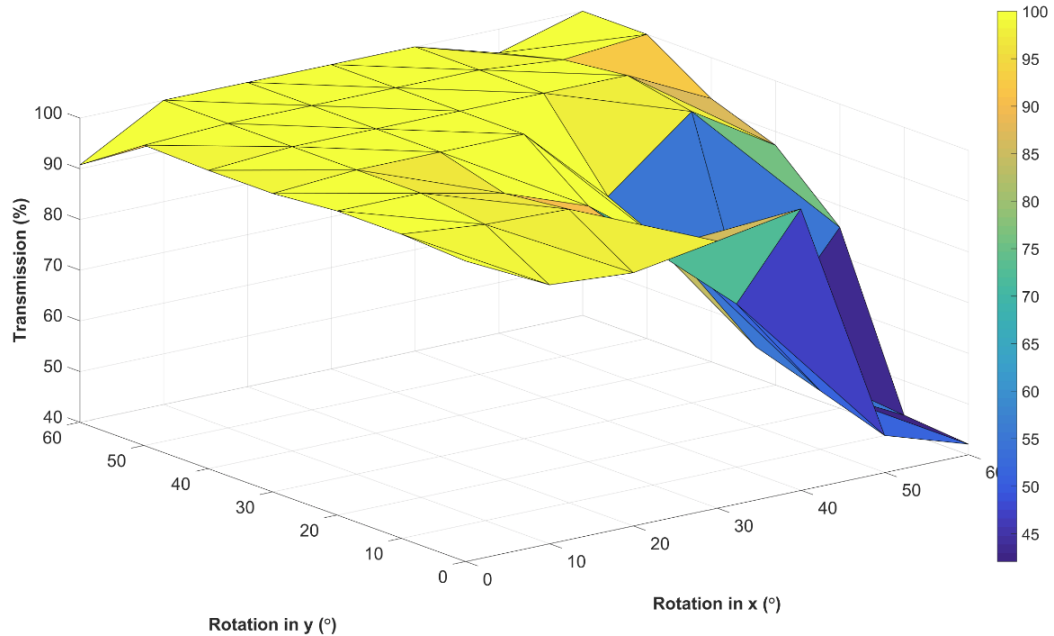


Figure 2.17: Angular dependence of transmission through a glass sample between $(x,y) = 0$ to 60° . Note that the transmission is only shown from 40% to 100%. The lowest recorded value of transmission in the 0 - 60° range was 42%.

2.4.2 Unidirectional Accuracy

The largest recorded error was during the movement of x with a constant value of y in forward and reverse directions. The root mean squared (RMS) absolute error in position

was determined to be 2.827. In contrast, the movement of y axis with a constant x yielded much lower RMS errors of 1.849 and 1.637 in the forward and reverse directions respectively. The results from the highest error configuration are shown in Figure 18. It should be noted the x-axis is more limited in its range as compared to the y-axis in the described configuration of the system. The x-stage is also smaller and lighter than the y-stage, making it more prone to shift slightly when y-stage is moved. To compensate for this, tighter fittings were used to ensure x-stage stays in place as compared to the y-stage. As the large range of the y-stage was of interest for running experiments, this was exploited more in the system leading to a slight loosening of y-stage fittings. While error in the intermediate angle range is kept almost the same for both x and y axes, towards the extreme angles this becomes more apparent.

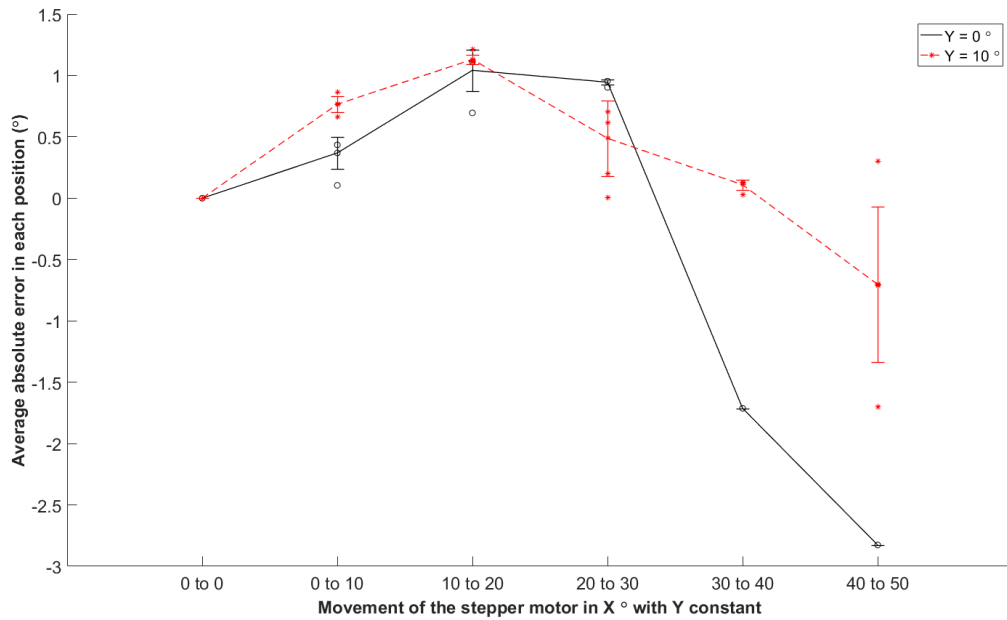


Figure 2.18: Unidirectional accuracy of the gimbal system with movement in x direction while holding y constant was found to be the least of all test cases. The root mean squared error value of all points was calculated. It was found to be the highest when x was moved from 40° to 50° with y constant at 0°. Interestingly the same high value of error was recorded when the x axis motor was moved in the reverse direction from 50° to 40° with y constant at 0°.

2.4.3 Repeatability

Six iterations of the experiment defined above were made in both forward and reverse directions (**Figure 2.19**). The root mean squared values of error in position of each movement category about the horizontal at zero were calculated as a way to quantify the disparity in position recorded during all 6 iterations. The highest repeatability was recorded for the movement of y in the forward direction when x is held constant. In contrast, the movement of x in the reverse direction when y is held constant was found to be the least repeatable.

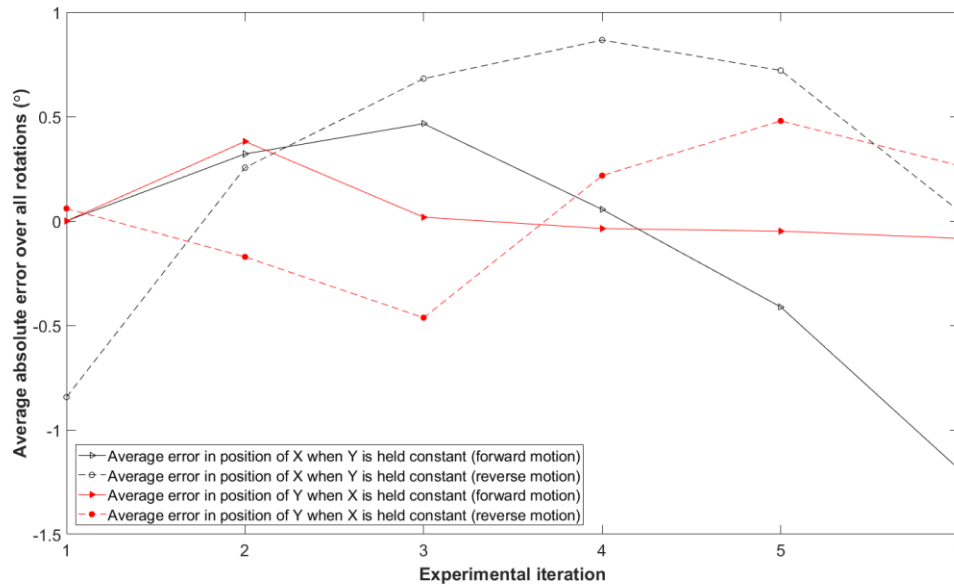


Figure 2.19: Repeatability was highest during the movement of y in the forward direction with x held constant. The RMS error recorded in this case was the least at 0.3950. The least repeatable condition was the movement of x when y is held constant (RMS = 1.5850).

2.4.4 Backlash

Backlash was quantified using the average errors across all 6 iterations when approaching the same final position from the forward and the reverse directions. During the movement of x (with y constant) to a final position of 50° the RMS error recorded was the highest at 1.237. This is visualized as the length of the error bars in Figure 20. The least error was recorded for movement of y axis to 0° with x held constant (RMS = 0.059).

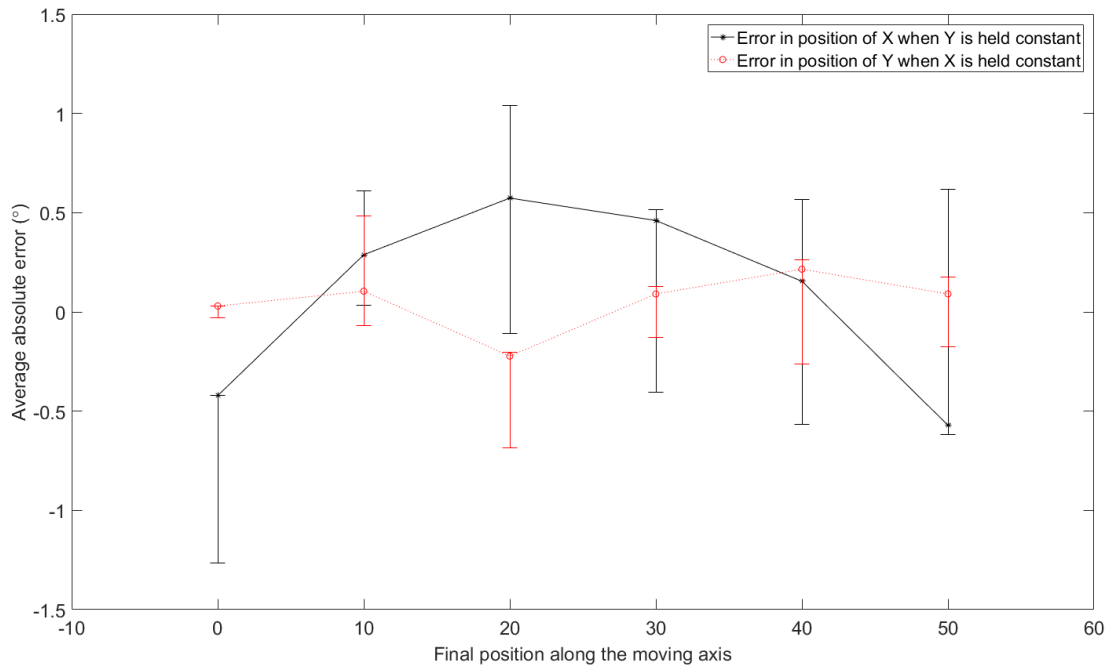


Figure 2.20: Backlash analysis yielded lowest error when a final position of 0° was approached by y with x held constant. In contrast, the highest error was recorded when x was moved to a final position of 50° . The top and bottom of the error bar represents the error in forward and reverse movement respectively. Hence the size of the error bar represents total backlash.

2.4.5 Maximum Speed

The 5V stepper motor used 2048 steps to complete a 360° rotation. Hence, each step was calculated to be 0.175° . The maximum speed set up in the software was 200 steps per second. Multiple attempts were made increase this speed, however, a grinding noise was observed when the speed was increased beyond 200 steps per second. This was equivalent to a maximum motor speed of 35.156° per second.

2.4.6 Speed resolution

The smallest incremental change in speed that could be measured was limited by the experimental constraints chosen for the transmission measurement of interest to the authors. The smallest recorded change was between 0.33° and 1.01° per second, which translated to a horizontal distance of 85cm and a vertical displacement of $1.5\text{cm} \pm 0.5$ as shown in **Figure 2.15**. Hence, the smallest measureable increment in steps was between 2 and 5 steps.

2.4.7 Micro step Size

Microstep size was determined by dividing the angle by the number of allowed states. Alternatively it was calculated by multiplying the steps per revolution of the motor by the number of allowed states. In this case the multiplier was 8. Since each revolution of the axes corresponded to 2048 steps, the microstepping was determined to be 16,384 steps per revolution, or 0.022° per step. While this is theoretically true, as stated in section 4.6, experimentally, a change in angle smaller than 0.33° could not be verified.

2.4.8 Angular Limitations

The angular rotation domain of the gimbal system can be visualized as seen in **Figure 2.21**. The shaded area represents the unhindered motion of the x and y axes together. Due to the design of this system other angles, while being partly accessible, may not allow adequate brightness in the transmission setup for optical measurements. The placement of the stepper motors and the frame obstructs the line of sight from the light source to the detector through the sample holder. However experimental results stated above show that the system could be used for optical measurements when targeted angles lie in the shaded regions.

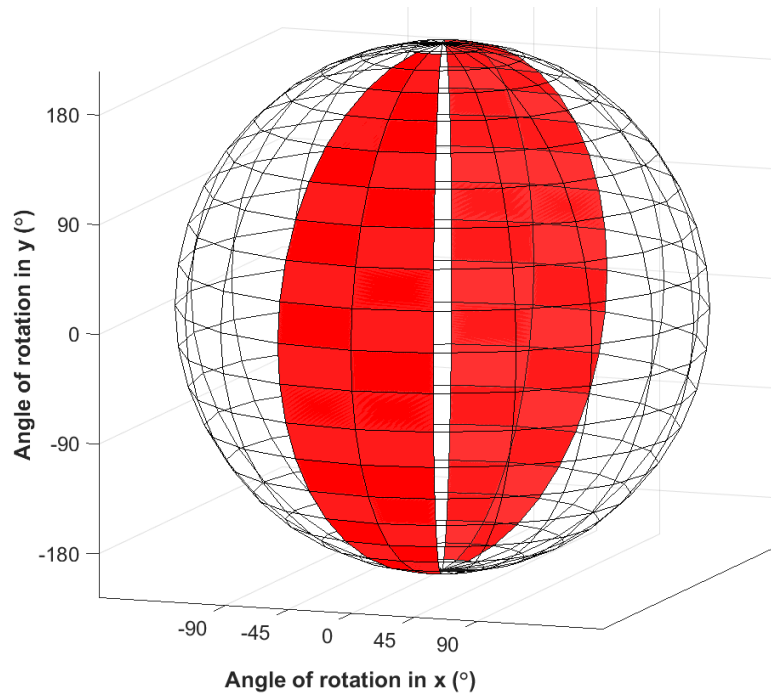


Figure 2.21: The shaded area represents the allowed motion of motors in both x and y directions while keeping adequate intensity at the detector for optical measurements. While angular limitation in the y direction is -180° to 180° , it is -45° to 45° in the x direction.

2.5 Discussion

The total cost of materials of the open source gimbal system is \$41.83, which is compared to the commercial systems already in the market shown in **Table 2.3**. As can be seen by **Table 2.3**, the open source gimbal system represents 95% or more savings from commercial systems. These cost savings are based on comparison of the material costs of the open source system to the retail price of the commercial systems. Thus, for the open source system there is no labor cost calculated for the purchasing of components, 3-D printing, and assembly. Each of these assumptions can be analyzed carefully. First, ignoring labor costs are relevant in the following situations: (1) where the 3-D printing and the assembly of the device is used as a learning aide for the construction of scientific equipment, open hardware or as part of a course [59, 94]; (2) where the labor is provided by unpaid interns or volunteers such as undergraduates trying to gain research experience and improve their resume or curriculum vitae; or, (3) where there is no opportunity cost to using existing salaried employee (e.g., the use of a lab manager or assistant or other position that is paid a fixed cost for all tasks conducted in a particular lab space, and for which there is no opportunity cost for them working on the fabrication of the device). At academic institutions such as colleges and universities these conditions can be readily met in most labs. In other labs, where this is not the case it is instructive to at the look at the potential cost of labor for the fabrication of the open source gimbal system. The labor involved is represented by three tasks: (1) 3-D printing the ten 3-D printed parts listed in **Table 2.1**, (2) purchasing the 12 components listed in Table 2; and (3) assembling the device and installing the software when all of the components have been gathered. The labor for each of these tasks will be analyzed separately, below using the lowest cost skill level employee.

First, the components listed in **Table 2.1** must be 3-D printed and due to the mass proliferation of FFF RepRap based 3-D printers [95], this can now be considered a relatively low-skilled task [96]. The designs have already been made are easily downloaded, pre-oriented and ready to be sent to a pre-calibrated FFF based 3-D printer. There are hundreds of thousands of these 3-D printers deployed globally [95], which are thus readily accessible to most labs. Although early desktop printers were challenging for non-experts, a tuned DIY RepRap like the one used in this study or a commercial self-bed leveling open source 3-D printer (e.g. a Lulzbot [97], Prusa [98], or Ultimaker [99]) can be left unattended after the file has been sent to print. This is similar in operation to the use of a 2-D printer or photocopying machine. The print time is not the labor time of the individual operating the printer as the 3-D printer does not need to be monitored by a user during printing. Thus, although the actual 3-D print time is much longer (approximately 9 hours for the slowest printing part, and 40 hours for all prints done in succession on a single printer), the time that labor is focused only on printing is less than half an hour to set up and clear 10 print jobs. For organizations without ready access to a 3-D printer, it should be pointed out that a low-end 3-D printer can be justified for the fabrication of even this tool alone as shown in **Table 2.3**. However, there is also access to 3-D printers at FabLabs [100,101], makerspaces [102], hackerspaces [103], and even public libraries [104] often have 3-D printing services available either for free, or for the cost of materials. Nearly all modern universities now have at least basic 3-D printing capabilities somewhere on campus, which are adequate to replicate the open source gimbal system. For researchers

with no access to 3-D printers locally, on demand quasi-local 3-D print services (e.g. MakeXYZ [105]) are available. The costs for a 3-D printing service will be more than the costs of the materials alone, but in general reasonable, as there is a high degree of competition because quotes are available immediately for users in any given area.

Table 2.3: Comparison of available gimbal systems compared to the open source gimbal system for accuracy, micro step size, repeatability and cost.

System	Accuracy	Micro step size	Repeatability	Cost (US\$)	Source
T-OMG Series: Miniature motorized gimbal optic mounts with built-in controllers	0.055°	0.000115378°	< 0.007°	\$1,440	[106]
Picomotor Piezo Optical Mounts	0.000069°	4°	0.00004°	\$1,088.00 - \$2,051.00	[107]
Stability Picomotor Piezo Optical Mounts	0.00004°	4°	0.00004°	\$1,536.00 - \$2,123.00	[107]
Open source gimbal system	2.827°	0.022°	1.585°	\$41.83	This study

Next, purchasing the components is a low-skill task, particularly when the hyperlinks to existing suppliers are provided (see [82]) and still active and purchasing is occurring in the United States (U.S.). The total time for this task would be about 12 min. for anyone with an existing Amazon account and shipping is free for those with Amazon prime. In the future, if these components are no longer available on these hyperlinks then they will need to be sourced from other websites, which would increase the time cost. On the other hand, as this is an open source hardware project, any number of entrepreneurs could begin to offer kits with all the components that could be purchased with a single order [108]. It should also be pointed out that it may be possible to decrease the cost of the device by careful comparison shopping for the components, and/or using existing supplies. Regardless of the exact situation, this subtask can be undertaken by the lowest-cost worker in an organization (e.g., a receptionist employed at a company) and represents a trivial cost.

Lastly, once all of the components are gathered they must be assembled by a moderately skilled worker following the instructions provided in this paper. Having designed the system, the researchers in this study could build the device in about 15 min. To remain conservative, for a novice builder the build time is estimated to be under 30 min.

Thus, the overall cost in labor to source, print, and assemble a 3-D printable open source gimbal system is about 1.25 h. This indicates that it is profitable for an organization to use the open source version if their labor costs are under \$250/h, even for the least expensive commercial equivalent (or under \$330/h for the average commercial system).

Finally, a point should be made about the life cycle cost advantages of the open source gimbal system. All of the design files are freely shared and the BOM is known. Thus, regardless of the cause of the failure of the device it can be easily repaired from readily available components (e.g. the user can reprint a broken plastic component or replace a stepper motor). This ease of repair (and even the ability to upgrade) is simply not available for all of the commercial systems, which would often demand the purchasing of a replacement device or a highly skilled and thus expensive repair. Furthermore, the ability to reuse parts from previously completed projects is also demonstrated in the addition of support structures from the open source laboratory sample rotator mixer and shaker [61]. Thus, the value of the open source tool can be considered higher than the commercial functional equivalent, even though the open source tool costs less than 5% of the cost of the commercial system to build upfront.

In light of the open source nature of this system, which opens up collaborative opportunities for further improvement, the current cost may justify the lower accuracy and higher errors associated with measurements made on this system. The quantified metrics of the system are acceptable for provisional testing and feasibility analyses of thin film transmittances. The system as described is thus adequate for the optical measurements it was designed for, but other researchers will need to carefully assess if the system meets the needs for their experiments as designed, if it needs to be improved, or if a full commercial system is warranted. Since the schematic is openly shared, in the future, upgrades to the microcontroller, motors and drivers can be made to further improve the characteristics. The design as described was optimized for quick print speeds. For this, standard print quality was used with a low level of infill. These parameters as well as the mechanical strength can be improved significantly by printer settings and material selection (e.g. print in polycarbonate) for a more robust system that may have a lower maintenance need.

This system also allows for a variety of custom-made sample holders, which could be designed and printed by a moderately skilled user. While the system used in this study is optimized for optical measurements of TCOs on a 75mm x 25mm x 1mm glass slide, different sample holders may be designed for up to 50 mm silicon wafers. The smallest sample holder size is limited by the spot size of the radiation and printing capabilities. The overall cost of the current set up is 1.97% of the most expensive commercial variant analyzed in this study and 4% of the least expensive. This saving in initial cost could potentially result in vast improvements.

This system could be expanded to include z-axis rotation as well with no required change in the skillset of the designer. The usability of this system may be expanded to optical alignment systems [109], active response systems [110], and as a mount for cameras in altitude estimation [111]. With minor modifications, this has applications not only in the semiconductor and optics fields but also in robotics, computer vision and surveying.

Both the low cost and the open source nature of the open source gimbal system are important as they provide accessibility to a wider range of users than was available. The

potential populations that will benefit from such a system include optics researchers at universities as well as K-12 teachers and Science, Technology, Engineering and Mathematics (STEM) outreach professionals who are typically in favor of building their own research equipment due to lower costs and easy troubleshooting due to a high degree of familiarity with apparatus. This study is also expected to have a greater impact in developing nations where the need to reduce costs while maintaining adequate technical performance is more significant than in well-funded laboratories [112].

2.6 Conclusions

The process of building a low cost two-axis gimbal system using RepRap 3-D printed parts is described and all non-printed parts are commercially available and inexpensive. The system performed as expected has a unidirectional accuracy of 2.827° , repeatability of 1.585° and a backlash error of 1.237° . Despite the highest mean squared errors, the open source gimbal system performed adequately while measuring transmission of radiation through glass slides with TCO coatings. This open source system also represents a 96% cost in savings as compared to the least expensive commercial variant. This study also opens up further opportunities for design improvements to modify the system based on user-specific applications.

2.7 Acknowledgements

This work was supported by the MOST lab and Fulbright Finland.

2.8 References

1. Narduzzo, A. and Rossi, A., 2008. *Modularity in action: GNU/Linux and free/open source software development model unleashed* (No. 020). Department of Computer and Management Sciences, University of Trento, Italy.
2. Meyer, M.H., Seliger, R., 1998. Product Platforms in Software Development. *Sloan Management Review*; Cambridge 40, 61–74.
3. Allen, E.B., Khoshgoftaar, T.M. and Chen, Y., 2001. Measuring coupling and cohesion of software modules: an information-theory approach. In *Software Metrics Symposium, 2001. METRICS 2001. Proceedings. Seventh International* (pp. 124-134). IEEE.
4. Laat, P.B. de, 2007b. Governance of open source software: state of the art. *J Manage Governance* 11, 165–177. doi:10.1007/s10997-007-9022-9
5. Grant, R.M., 1996. Toward a knowledge-based theory of the firm. *Strat. Mgmt. J.* 17, 109–122. doi:10.1002/smj.4250171110
6. Simon, H.A., 1991. Organizations and Markets. *The Journal of Economic Perspectives* 5, 25–44.

7. Taylor, J.B., 1993, December. Discretion versus policy rules in practice. In *Carnegie-Rochester conference series on public policy* (Vol. 39, pp. 195-214). North-Holland.
8. Hertel, G., Niedner, S., Herrmann, S., 2003. Motivation of software developers in Open Source projects: an Internet-based survey of contributors to the Linux kernel. *Research Policy, Open Source Software Development* 32, 1159–1177. doi:10.1016/S0048-7333(03)00047-7
9. Lee, G.K., Cole, R.E., 2003. From a Firm-Based to a Community-Based Model of Knowledge Creation: The Case of the Linux Kernel Development. *Organization Science* 14, 633–649. doi:10.1287/orsc.14.6.633.24866
10. Kogut, B., Metiu, A., 2001. Open-Source Software Development and Distributed Innovation. *Oxf Rev Econ Policy* 17, 248–264. doi:10.1093/oxrep/17.2.248
11. Mockus, A., Fielding, R.T., Herbsleb, J., 2000. A case study of open source software development: the Apache server, in: *Proceedings of the 2000 International Conference on Software Engineering. ICSE 2000 the New Millennium*. Presented at the *Proceedings of the 2000 International Conference on Software Engineering. ICSE 2000 the New Millennium*, pp. 263–272. doi:10.1145/337180.337209
12. Bagozzi, R.P., Dholakia, U.M., 2006. Open Source Software User Communities: A Study of Participation in Linux User Groups. *Management Science* 52, 1099–1115. doi:10.1287/mnsc.1060.0545
13. Dempsey, B.J., Weiss, D., Jones, P., Greenberg, J., 1999. A quantitative profile of a community of open source Linux developers. Chapel Hill: School of Information and Library Science, University of North Carolina
14. Hars, A., Ou, S., 2001. Working for free? Motivations of participating in open source projects, in: *Proceedings of the 34th Annual Hawaii International Conference on System Sciences*. Presented at the *Proceedings of the 34th Annual Hawaii International Conference on System Sciences*, p. 9. doi:10.1109/HICSS.2001.927045
15. Feller, J., Fitzgerald, B., others, 2002. *Understanding open source software development*. Addison-Wesley London.
16. Bonaccorsi, A., Rossi, C., 2003. Why Open Source software can succeed. *Research Policy, Open Source Software Development* 32, 1243–1258. doi:10.1016/S0048-7333(03)00051-9f
17. Crowston, K., Howison, J., 2005. The social structure of free and open source software development. *First Monday* 10. doi:10.5210/fm.v10i2.1207
18. Tu, Q., 2000. Evolution in open source software: A case study. In *Software Maintenance, 2000. Proceedings. International Conference on* (pp. 131-142). IEEE.
19. Drumea, A., 2012. Education in development of electronic modules using free and open source software tools. “HIDRAULICA” Magazine of Hydraulics, Pneumatics, Tribology, Ecology, Sensorics, Mechatronics, (3–4), pp.54-60.
20. Sarker, M.O.F., Kim, C. and You, B.J., 2006, July. Development of a network-based real-time robot control system over IEEE 1394: Using open source software

- platform. In *Mechatronics, 2006 IEEE International Conference on* (pp. 563-568). IEEE.
21. Xi, X.C., Hong, G.S. and Poo, A.N., 2010. Improving CNC contouring accuracy by integral sliding mode control. *Mechatronics*, 20(4), pp.442-452.
 22. Gibb, A., 2014. *Building Open Source Hardware: DIY Manufacturing for Hackers and Makers*. Pearson Education.
 23. Balka, K., Raasch, C., Herstatt, C., 2009. Open source enters the world of atoms: A statistical analysis of open design. *First Monday* 14. doi:10.5210/fm.v14i11.2670
 24. Zhang, L., Slaets, P. and Bruyninckx, H., 2012. An open embedded hardware and software architecture applied to industrial robot control. In *Mechatronics and Automation (ICMA), 2012 International Conference on* (pp. 1822-1828). IEEE.
 25. Banzi, M. and Shiloh, M., 2014. *Getting Started with Arduino: The Open Source Electronics Prototyping Platform*. Maker Media, Inc.
 26. Pearce, J.M., 2012. Building research equipment with free, open-source hardware. *Science*, 337(6100), pp.1303-1304.
 27. Baldwin, C.Y., Clark, K.B., 2000. *Design Rules: The power of modularity*. MIT Press.
 28. Pocero, L., Amaxilatis, D., Mylonas, G., & Chatzigiannakis, I. (2017). Open source IoT meter devices for smart and energy-efficient school buildings. *HardwareX*, 1, 54-67.
 29. McMunn, M. S. (2017). A time-sorting pitfall trap and temperature datalogger for the sampling of surface-active arthropods. *HardwareX*, 1, 38-45.
 30. Oh, J., Hofer, R., & Fitch, W. T. (2017). An open source automatic feeder for animal experiments. *HardwareX*, 1, 13-21.
 31. Buechley, L., Eisenberg, M., Catchen, J., Crockett, A., 2008. The LilyPad Arduino: Using Computational Textiles to Investigate Engagement, Aesthetics, and Diversity in Computer Science Education, in: *Proceedings of the SIGCHI Conference on Human Factors in Computing Systems, CHI '08*. ACM, New York, NY, USA, pp. 423–432. doi:10.1145/1357054.1357123.
 32. Coyle, S., Morris, D., Lau, K.T., Diamond, D., Moyna, N., 2009. Textile-Based Wearable Sensors for Assisting Sports Performance, in: *2009 Sixth International Workshop on Wearable and Implantable Body Sensor Networks*. Presented at the 2009 Sixth International Workshop on Wearable and Implantable Body Sensor Networks, pp. 307–311. doi:10.1109/BSN.2009.57
 33. Sugathan, A., Roy, G.G., Kirthyvijay, G.J., Thomson, J., 2013. Application of arduino based platform for wearable health monitoring system, in: *2013 IEEE 1st International Conference on Condition Assessment Techniques in Electrical Systems (CATCON)*. Presented at the 2013 IEEE 1st International Conference on Condition Assessment Techniques in Electrical Systems (CATCON), pp. 1–5. doi:10.1109/CATCON.2013.6737464
 34. Purusothaman, S.R.R.D., Rajesh, R., Vijayaraghavan, V., Bajaj, K.K., 2014. Design of Arduino-based communication agent for rural Indian microgrids, in: *2014 IEEE Innovative Smart Grid Technologies - Asia (ISGT ASIA)*. Presented at

- the 2014 IEEE Innovative Smart Grid Technologies - Asia (ISGT ASIA), pp. 630–634. doi:10.1109/ISGT-Asia.2014.6873865
35. Zachariadou, K., Yiasemides, K., Trougakos, N., 2012. A low-cost computer-controlled Arduino-based educational laboratory system for teaching the fundamentals of photovoltaic cells. *Eur. J. Phys.* 33,1599. doi:10.1088/0143-0807/33/6/1599
 36. Kentzer, J., Koch, B., Thiim, M., Jones, R.W. and Villumsen, E., 2011, May. An open source hardware-based mechatronics project: The replicating rapid 3-D printer. In *Mechatronics (ICOM), 2011 4th International Conference On* (pp. 1-8). IEEE.
 37. Baraka, K., Ghobril, M., Malek, S., Kanj, R. and Kayssi, A., 2013, June. Low cost arduino/android-based energy-efficient home automation system with smart task scheduling. In *Computational Intelligence, Communication Systems and Networks (CICSyN), 2013 Fifth International Conference on* (pp. 296-301). IEEE.
 38. Piyare, R., Tazil, M., 2011. Bluetooth based home automation system using cell phone, in: 2011 IEEE 15th International Symposium on Consumer Electronics (ISCE). Presented at the 2011 IEEE 15th International Symposium on Consumer Electronics (ISCE), pp. 192–195. doi:10.1109/ISCE.2011.5973811
 39. Kumar, P., Kumar, P., 2013. Arduino based wireless intrusion detection using IR sensor and GSM. *International Journal of Computer Science and Mobile Computing* 2, 417–424.
 40. Pearce, J.M., 2013. *Open-Source Lab: How to Build Your Own Hardware and Reduce Research Costs*. Elsevier: New York.
 41. Ferdoush, S., Li, X., 2014. Wireless Sensor Network System Design Using Raspberry Pi and Arduino for Environmental Monitoring Applications. *Procedia Computer Science, The 9th International Conference on Future Networks and Communications (FNC'14)/The 11th International Conference on Mobile Systems and Pervasive Computing (MobiSPC'14)/Affiliated Workshops 34*, 103–110. doi:10.1016/j.procs.2014.07.059
 42. Méndez, D., Pérez, A.J., Labrador, M.A., Marrón, J.J., 2011. P-Sense: A participatory sensing system for air pollution monitoring and control, in: 2011 IEEE International Conference on Pervasive Computing and Communications Workshops (PERCOM Workshops). Presented at the 2011 IEEE International Conference on Pervasive Computing and Communications Workshops (PERCOM Workshops), pp. 344–347. doi:10.1109/PERCOMW.2011.5766902
 43. Lee, S., Jo, J., Kim, Y., Stephen, H., 2014. A Framework for Environmental Monitoring with Arduino-Based Sensors Using Restful Web Service, in: 2014 IEEE International Conference on Services Computing. Presented at the 2014 IEEE International Conference on Services Computing, pp. 275–282. doi:10.1109/SCC.2014.44
 44. Gertz, E., Justo, P.D., 2012. *Environmental Monitoring with Arduino: Building Simple Devices to Collect Data About the World Around Us*. O'Reilly Media, Inc.

45. Busquets, J., Busquets, J.V., Tudela, D., Pérez, F., Busquets-Carbonell, J., Barberá, A., Rodríguez, C., García, A.J., Gilabert, J., 2012. Low-cost AUV based on Arduino open source microcontroller board for oceanographic research applications in a collaborative long term deployment missions and suitable for combining with an USV as autonomous automatic recharging platform, in: *Autonomous Underwater Vehicles (AUV)*, 2012 IEEE/OES. IEEE, pp. 1–10.
46. Leeuw, T., Boss, E.S., Wright, D.L., 2013. In situ Measurements of Phytoplankton Fluorescence Using Low Cost Electronics. *Sensors* 13, 7872–7883. doi:10.3390/s130607872
47. Alkandari, A., alnasheet, M., Alabduljader, Y., Moein, S.M., 2012. Water monitoring system using Wireless Sensor Network (WSN): Case study of Kuwait beaches, in: *2012 Second International Conference on Digital Information Processing and Communications (ICDIPC)*. Presented at the 2012 Second International Conference on Digital Information Processing and Communications (ICDIPC), pp. 10–15. doi:10.1109/ICDIPC.2012.6257270
48. Bardají, R., Zafra, E., Simon, C., Piera, J., 2014. Comparing water transparency measurements obtained with low-cost citizens science instruments and high-quality oceanographic instruments, in: *OCEANS 2014 - TAIPEI*. Presented at the OCEANS 2014 - TAIPEI, pp. 1–4. doi:10.1109/OCEANSTAIPEI.2014.6964550
49. Navajas, G.T. and Prada, S.R., 2014, October. Building your own quadrotor: A mechatronics system design case study. In *Engineering Mechatronics and Automation (CIIMA), 2014 III International Congress of* (pp. 1-5). IEEE.
50. Abaid, N., Bernhardt, J., Frank, J.A., Kapila, V., Kimani, D. and Porfiri, M., 2013. Controlling a robotic fish with a smart phone. *Mechatronics*, 23(5), pp.491-496.
51. Jenabi, S.H., Shahri, A.M. and Beyad, M.R., 2016, January. Advanced mechatronics course based on wheeled mobile robots and real-time embedded control experimental setups. In *Control, Instrumentation, and Automation (ICCIA), 2016 4th International Conference on* (pp. 413-418). IEEE.
52. Grover, R., Krishnan, S., Shoup, T. and Khanbaghi, M., 2014, March. A competition-based approach for undergraduate mechatronics education using the arduino platform. In *Interdisciplinary Engineering Design Education Conference (IEDEC), 2014 4th* (pp. 78-83). IEEE.
53. Asato, K., Asato, K., Nagado, T. and Tamaki, S., 2015, November. Development of low cost educational material for learning fundamentals of mechatronics. In *Intelligent Informatics and Biomedical Sciences (ICIIBMS), 2015 International Conference on* (pp. 454-456). IEEE.
54. Soriano, A., Marin, L., Valles, M., Valera, A. and Albertos, P., 2014. Low Cost Platform for Automatic Control Education Based on Open Hardware. *IFAC Proceedings Volumes*, 47(3), pp.9044-9050.
55. Jones, R., Haufe, P., Sells, E., Iravani, P., Olliver, V., Palmer, C. and Bowyer, A., 2011. RepRap—the replicating rapid prototyper. *Robotica*, 29(01), pp.177-191.
56. Rundle, G., 2014. *A Revolution in the Making*. Simon and Schuster.

57. Gonzalez-Gomez, J., Valero-Gomez, A., Prieto-Moreno, A. and Abderrahim, M., 2012. A new open source 3d-printable mobile robotic platform for education. In *Advances in autonomous mini robots* (pp. 49-62). Springer Berlin Heidelberg.
58. Irwin, J.L., Pearce, J.M., Anzalone, G. and Oppliger, D.E., 2014, June. The RepRap 3-D printer revolution in STEM education. In *121st ASEE Annual Conference & Exposition* (pp. 15-18).
59. Schelly, C., Anzalone, G., Wijnen, B. and Pearce, J.M., 2015. Open-source 3-D printing technologies for education: Bringing additive manufacturing to the classroom. *Journal of Visual Languages & Computing*, 28, pp.226-237.
60. Baden, T., Chagas, A.M., Gage, G., Marzullo, T., Prieto-Godino, L.L. and Euler, T., 2015. Open Labware: 3-D printing your own lab equipment. *PLoS Biol*, 13(3), p.e1002086.
61. Dhankani, K.C., Pearce, J.M., 2017. Open source laboratory sample rotator mixer and shaker. *HardwareX* 1, 1–12. doi:10.1016/j.ohx.2016.07.001
62. <https://3dprint.nih.gov/>
63. <https://www.youmagine.com/>
64. <https://www.myminifactory.com/>
65. <https://grabcad.com/>
66. <https://www.thingiverse.com/>
67. Wittbrodt, B.T., Glover, A.G., Laureto, J., Anzalone, G.C., Oppliger, D., Irwin, J.L. and Pearce, J.M., 2013. Life-cycle economic analysis of distributed manufacturing with open-source 3-D printers. *Mechatronics*, 23(6), pp.713-726.
68. Willis, K., Brockmeyer, E., Hudson, S., Poupyrev, I., 2012. Printed Optics: 3D Printing of Embedded Optical Elements for Interactive Devices, in: *Proceedings of the 25th Annual ACM Symposium on User Interface Software and Technology, UIST '12*. ACM, New York, NY, USA, pp. 589–598. doi:10.1145/2380116.2380190
69. Brockmeyer, E., Poupyrev, I., Hudson, S., 2013. PAPHON: Designing Curved Display Surfaces with Printed Optics, in: *Proceedings of the 26th Annual ACM Symposium on User Interface Software and Technology, UIST '13*. ACM, New York, NY, USA, pp. 457–462. doi:10.1145/2501988.2502027
70. Bentz, B.Z., Chavan, A.V., Lin, D., Tsai, E.H. and Webb, K.J., 2016. Fabrication and application of heterogeneous printed mouse phantoms for whole animal optical imaging. *Applied optics*, 55(2), pp.280-287.
71. Zou, L., Koslakiewicz, R., Mahmoud, M., Fahs, M., Liu, R. and Lo, J.F., 2016. Three-dimensional printed miniaturized spectral system for collagen fluorescence lifetime measurements. *Journal of biomedical optics*, 21(7), pp.075001-075001.
72. Sharkey, J.P., Foo, D.C., Kabla, A., Baumberg, J.J. and Bowman, R.W., 2016. A one-piece 3D printed flexure translation stage for open-source microscopy. *Review of Scientific Instruments*, 87(2), p.025104.
73. Coakley, M. and Hurt, D.E., 2016. 3D Printing in the Laboratory: Maximize Time and Funds with Customized and Open-Source Labware. *Journal of Laboratory Automation*, 21(4), pp.489-495.

74. Wijnen, B., Petersen, E.E., Hunt, E.J. and Pearce, J.M., 2016. Free and open-source automated 3-D microscope. *Journal of Microscopy*, 264(2), pp.238-246.
75. Zhang, C., Anzalone, N.C., Faria, R.P. and Pearce, J.M., 2013. Open-source 3D-printable optics equipment. *PloS one*, 8(3), p.e59840.
76. Zhao, J., Green, M.A., 1991. Optimized antireflection coatings for high-efficiency silicon solar cells. *IEEE Transactions on Electron Devices* 38, 1925–1934. doi:10.1109/16.119035
77. Zhao, J., Wang, A., Altermatt, P. and Green, M.A., 1995. Twenty-four percent efficient silicon solar cells with double layer antireflection coatings and reduced resistance loss. *Applied Physics Letters*, 66(26), pp.3636-3638.
78. Parretta, A., Sarno, A., Tortora, P., Yakubu, H., Maddalena, P., Zhao, J. and Wang, A., 1999. Angle-dependent reflectance measurements on photovoltaic materials and solar cells. *Optics Communications*, 172(1-6), pp.139-151.
79. Pfaff, G., Reynders, P., 1999. Angle-Dependent Optical Effects Deriving from Submicron Structures of Films and Pigments. *Chem. Rev.* 99, 1963–1982. doi:10.1021/cr970075u
80. Tsuji, J., 1927-, 1995. Palladium reagents and catalysts. Wiley & Sons.
81. Oberloier, S. and Pearce, J.M. General Design Procedure for Free and Open-Source Hardware for Scientific Equipment. *Designs* 2018, 2(1), 2; doi:10.3390/designs2010002
82. Open Source Dual Axis Gimbal System <https://osf.io/6nse3/> (accessed 12.8.2017)
83. FreeCAD <https://www.freecadweb.org/> (accessed 5.2.2017).
84. <https://www.lulzbot.com/store/filament>
85. Anzalone, G.C., Wijnen, B. and Pearce, J.M., 2015. Multi-material additive and subtractive prosumer digital fabrication with a free and open-source convertible delta RepRap 3-D printer. *Rapid Prototyping Journal*, 21(5), pp.506-519.
86. Wijnen, B., Anzalone, G.C., Haselhuhn, A.S., Sanders, P.G., Pearce, J.M., 2016. Free and Open-source Control Software for 3-D Motion and Processing. *Journal of Open Research Software* 4. doi:10.5334/jors.78
87. Arduino. Arduino IDE. <https://www.arduino.cc/en/Main/Software> (accessed 5.2.2017).
88. Leenhouts, A.C., 1997. Step motor system design handbook. Litchfield Engineering.
89. Rogers, J.R. and Craig, K., 2005. On-hardware optimization of stepper-motor system dynamics. *Mechatronics*, 15(3), pp.291-316.
90. Muñoz, C., Levi, R., Benkrid, M., Rodríguez, F.B. and Varona, P., 2008. Real-time control of stepper motors for mechano-sensory stimulation. *Journal of Neuroscience Methods*, 172(1), pp.105-111.
91. Banihani, S., Al-Widyan, K., Al-Jarrah, A. and Ababneh, M., 2013. A genetic algorithm based lookup table approach for optimal stepping sequence of open-loop stepper motor systems. *Journal of Control Theory and Applications*, 11(1), pp.35-41.
92. Righettini, P., Strada, R., Oldani, A.C. and Ginammi, A., 2012. An experimental investigation on the dynamic behavior of step motor drives. *Journal of Mechanics Engineering and Automation*, 2(7), pp.431-440.

93. Baluta, G., 2007, July. Microstepping mode for stepper motor control. In *Signals, Circuits and Systems, 2007. ISSCS 2007. International Symposium on* (Vol. 2, pp. 1-4). IEEE.
94. Bailey, M.; Grieco, J.; Speights, A.; Weiss, R.G. 3D printing in the classroom and laboratory. *J. Comput. Sci. Coll.* 2015, 31, 183–184.
95. Wohler, T. (2016). Wohlers report 2016. Wohlers Associates, Inc.
96. Petersn, E. E., & Pearce, J. (2017). Emergence of Home Manufacturing in the Developed World: Return on Investment for Open-Source 3-D Printers. *Technologies*, 5(1), 7. doi:10.3390/technologies5010007
97. <https://www.lulzbot.com/>
98. <https://www.prusa3d.com/>
99. <https://ultimaker.com/> Stacey, M. The FAB LAB network: A global platform for digital invention, education and entrepreneurship. *Innovations* 2014, 9, 221–238.
100. Fab Foundation. Fab Labs. Available online: <http://www.fabfoundation.org/fab-labs/> (accessed on 31 October 2017).
101. The Maker Map. Available online: <http://themakermap.com/> (accessed on 31 October 2017).
102. Hackspaces. Available online: <https://wiki.hackerspaces.org/> (accessed on 31 October 2017).
103. Mooreield-Lang, H. 3-D printing in your libraries and classrooms. *Knowl. Quest* 2014, 43, 70–73.
104. MakeXYZ Available online: <https://www.makexyz.com/> (accessed on 31 October 2017).
105. ZaberTechnologies
https://www.zaber.com/products/product_detail.php?detail=T-OMG
106. Newport Photonics Solutions <https://www.newport.com/f/picomotor-piezo-mirror-mounts>
107. Pearce, J. M. (2017). Emerging Business Models for Open Source Hardware. *Journal of Open Hardware*, 1(1). Doi: <http://doi.org/10.5334/joh.4>
108. Burge, J.H., Su, P., Zhao, C. and Zobrist, T., 2007, September. Use of a commercial laser tracker for optical alignment. In *Proc. SPIE* (Vol. 6676, p. 66760E).
109. Wilson, G.W., 1975, August. Double gimbal control moment gyroscope-gimbal control loop synthesis. In *AIAA, Guidance and Control Conference*.
110. Zhang, R. and Liu, H.H., 2011, June. Vision-based relative altitude estimation of small unmanned aerial vehicles in target localization. In *American Control Conference (ACC)*, 2011 (pp. 4622-4627). IEEE.
111. J. Gwamuri, and Pearce, 2017. Open source 3D printers: an appropriate technology for building low cost optics labs for the developing communities", *Proc. SPIE 10452, 14th Conference on Education and Training in Optics and Photonics: ETOP 2017*, 104522S (16 August 2017); doi: 10.1117/12.2269852

3 Atomic layer deposited aluminum oxide mitigates outgassing from fused filament fabrication–based 3-D printed components

3.1 Introduction

Additive manufacturing (AM) methods allow for rapid prototyping of designs and producing complex geometries that are not easily accessible by other manufacturing methods. In recent years, AM has facilitated the development of various open-source research tools, and especially affordable fused filament fabrication (FFF)–based 3-D printing shows great potential in laboratories in the fabrication of low-cost, customized, and high-quality scientific instruments [1-3]. Generally, these bespoke tools can reduce the cost of scientific equipment by 90-99% compared to commercial equipment, which has already created considerable value for the scientific community [4,5]. Examples of such tools include chemical mixers [6,7], microfluidic devices [8-11], and mass spectroscopy equipment [12], which highlights the various fields in which laboratories can benefit from open source scientific hardware.

Despite their promise, only a few short studies on using 3-D printed components in vacuum environments have been published [13-17]. Studies by Gans *et al.* [13] and Povilus *et al.* [14] mention that both the high porosity of FFF plastics and their lack of mechanical strength might pose issues in a vacuum. During the printing process, small voids and inclusions can form in the component, which can trap atmospheric gases. These gases can slowly leak into the vacuum environment, which increases the pressure in the vacuum vessel and renders the component incompatible with low-pressure applications. Other concerns in using plastics in vacuum environments are the high vapour pressure of the material itself, which can lead to significant amount of outgassing, and their limited thermal conductance. These issues have been discussed in previous studies [13, 15, 18, 19]. A potential approach to mitigate outgassing from 3-D printed plastics is to coat the component with metal layers [16] or by commercial vacuum sealing resins [17].

Atomic layer deposited (ALD) AlO_x is a potential material for outgassing reduction, as layers that efficiently limit gas diffusion [20] can be deposited even at low temperatures [21-23] on various polymers [24]. ALD films have been demonstrated as viable layers for increasing the performance of polymers in space applications, such as protecting plastics from degradation [18] and potentially reducing outgassing of plastics at elevated temperatures [19]. In this study, we explore the mitigation of outgassing from affordable and easily printable FFF plastics using vacuum resins or thin inorganic aluminium oxide (AlO_x) coatings prepared by in house ALD. Specifically, we investigate the worst-case scenario using black pigmented plastics whose coloring agents can add to outgassing. The ultimate aim of these experiments is to create a toolkit for an open-source fully 3-D printable ALD tool, capable of producing high-quality ALD films for contamination-sensitive applications.

3.2 Experimental

The investigated commercial 3-D printed materials were acrylonitrile butadiene styrene (ABS), which is one of the most common FFF plastics, and polycarbonate (PC), which is one of the highest strength plastics commonly available for standard FFF-based 3-D printers [25]. The plastics were coated with either a commercial vacuum sealing resin or ALD AlO_x , and the reduction of outgassing was compared using a residual gas analysis (RGA) tool. Black 3-D printed plastics were used to explore the limits of outgassing reduction, as a large number of concentrates used for black colouring are based on carbon black, which is a known outgassing agent [26]. The thermal and vacuum history of all samples were carefully matched to each other to provide an accurate analysis of the outgassing properties of the plastics.

3.2.1 Sample preparation

3-D models of rectangular samples with the dimensions $5 \text{ mm} \times 5 \text{ mm} \times 2 \text{ mm}$ and $30 \text{ mm} \times 30 \text{ mm} \times 1 \text{ mm}$ were designed using OpenSCAD [27]. Uncoated $5 \text{ mm} \times 5 \text{ mm} \times 2 \text{ mm}$ samples were used in surface area analysis, while the $30 \text{ mm} \times 30 \text{ mm} \times 1 \text{ mm}$ were coated and used in outgassing studies. The samples were printed with an open source Lulzbot Taz 6 FFF-based 3-D printer (Aleph Objects, Loveland CO) using commercial 3-D printing filaments of ABS and PC. The ABS filament was obtained from IC3D (Ohio, USA), and PC (PC-Max) from Polymaker (Shanghai, China). The printer and slicing settings were determined with the Cura slicing software (21.08 Lulzbot edition), and the samples were printed with 100% infill using the printing parameters described in Table 3.1. PVA-based glue was applied to the printing bed before printing PC to decrease the adhesion between the samples and the printing bed. The residual glue was removed from the PC samples with particular care by wiping them with water-damped disposable laboratory wipes. After printing, both ABS and PC samples were handled with nitrile gloves and cleaned by consecutively wiping them with lint-free wipes damped in water and isopropanol.

Table 3.1: Essential printing parameters of the ABS and PC samples, defined using the Cura software.

Plastic	Layer height [mm]	Shell thickness [mm]	Bottom/top thickness [mm]	Print speed [mm/s]	Top/bottom speed [mm/s]	Print T [°C]	Bed T [°C]	Minimal layer time [s]
ABS	0.18	1.0	1.05	50	30	245	95	15
PC	0.15	1.0	0.9	50	30	255	100	20

The first sets of $30 \text{ mm} \times 30 \text{ mm} \times 1 \text{ mm}$ ABS and PC samples were treated with a commercial silicone-based high vacuum leak sealing resin (Vacseal [28]), which was cured at 95°C for 24 hours [17]. The resin was applied to the top, bottom and sides of the samples using a brush. The second sample set of the same dimensions was coated with ALD AlO_x using a Picosun R-100 top-flow ALD tool with trimethylaluminum (TMA) and deionized

water as precursors. The reactor temperature was 80°C, which was below the glass transition temperature of both ABS (~105°C) and PC (~110°C) [29]. The reactor pressure was ~20 mTorr in a constant N₂ flow. TMA and water were dosed into the reactor from external containers kept at room temperature using pneumatic valves with pulse lengths 0.2 and 0.5 s, respectively, with 5 s purging steps between the precursor pulses. The samples were placed on top of silicon wafers used as monitor samples and coated with 300 cycles of AlO_x per run in three consecutive runs, labelled depositions I, II, and III. Since the 3-D printed samples have high surface roughness there was some gas flow between the monitor wafer and the bottom of the plastic sample. The use of the monitor samples for film thickness characterization is further explained in the next section. Third sample set was made by applying the vacuum resin to the side facing the Si wafer during the deposition of some of the ALD-coated samples and curing them at 95°C at 24 hours. Uncoated samples were used as a reference set.

The vacuum histories of all samples were matched to the ALD-coated samples by placing the resin-coated and the reference samples in a vacuum chamber in ~20 mTorr pressure at 80°C for the duration of the ALD runs (~5 h). This sample pre-treatment was done to ensure that each sample had the opportunity to outgas and dehydrate before characterization. All sample sets and their corresponding coatings and pre-treatments are summarized in Table 3.2.

Table 3.2: Sample types and methods of pre-treatment. All samples were prepared for both ABS and PC.

Sample set	ALD coating	Pre-treatment	Resin applied	Resin curing
Resin-coated	None	80°C at 20 mTorr for 5 h	All sides	95°C for 24 h
ALD-coated	900 cycles AlO _x at 80°C	None	No	None
Resin- and ALD-coated	900 cycles AlO _x at 80°C	None	Bottom side	95°C for 24 h
Reference	None	80°C at 20mTorr for 5 h	No	None

3.2.2 Characterization

The specific surface area of 3-D printed ABS and PC was determined using Brunauer-Emmett-Teller (BET) theory [30]. The nitrogen adsorption and desorption properties at liquid nitrogen temperature (77K) were investigated from one hundred pieces of the 5 mm × 5 mm × 2 mm samples using a Micromeritics ASAP 2000 instrument. PC and ABS samples were cryofractured and coated with conducting Pt:Pd in a 80:20 ratio, and scanning electron microscope (SEM) images were acquired with a Hitachi S-4700 field emission SEM (FE-SEM) to investigate the polymer cross-section microstructures. The same equipment was used for energy-dispersive X-ray spectroscopy (EDX) to identify the spatial distribution of elements in the micrographs. Depth profiling using X-ray photoelectron spectroscopy (XPS) was conducted using a PHI 5800 photoelectron

spectrometer (Physical Electronics, Minnesota, USA) to check for carbon contamination in the deposited inorganic film.

A bespoke quadrupole residual gas analyser (RGA) setup, shown in Figure 1(a), was used in the outgassing experiments. The load lock region of a Riber molecular beam epitaxy system was connected to a roughing and turbo pump to create an isolated chamber capable of holding a vacuum of 10^{-7} Torr. A Transpector Inficon gas analysis system was installed on an available flange. A sample heater capable of reaching 100°C was mounted in the chamber and used to test the outgassing of the samples at 10°C increments, from base temperature ($>36^{\circ}\text{C}$) until 100°C . Baseline partial pressure data using the RGA was gathered without a sample loaded at each temperature set point to characterize the inherent species present in an empty chamber. Samples were stored in a sealed desiccant container for a minimum of 24 hours prior to RGA analysis. Each sample was placed in the vacuum chamber at a base pressure of 1.7 to 2.3×10^{-7} Torr for 12 hours before initiating the measurement. The partial pressures for species with 1 to 100 atomic mass units (AMU) were recorded using a TWare32 gas analysis software at the specified temperatures.

The data for each measurement was normalized using Equation 3.1 to isolate the quantity of outgassed species:

$$PP = \frac{\left(\frac{PP_M}{P_0}\right)}{\left(\frac{PP_M^B}{P_0^B}\right)} \quad 3.1$$

where

PP_M is the partial pressure of the molecular mass of interest,

P_0 is the chamber pressure during the run,

PP_M^B is the partial pressure of the molecular mass of interest during the baseline run (without sample),

P_0^B is the chamber pressure during the baseline run.

Due to the variation in base pressure during each run, the partial pressure in both the numerator and the denominator were divided by the base pressure during that run. The noise level of the partial pressure measurement was approximately 10^{-15} Torr, so data below this limit was discarded.

During the ALD depositions, 4-inch silicon wafers (Okmetic, n-type, $300 \mu\text{m}$, $2\text{-}5 \Omega/\text{cm}$, double-side polished, 100 orientation) were used as monitor samples to facilitate the characterization of film growth in the ALD runs. Initially, a $30 \text{ mm} \times 30 \text{ mm}$ piece of a similar Si wafer was placed on top of a monitor wafer to study how the geometry of the samples affect the film growth. A schematic explaining the sample positioning inside the ALD reactor is presented in Figure 3.1(b). One 3-D printed plastic sample at a time was placed on a monitor wafer, and the samples were coated with 300 cycles of AlO_x per run in three consecutive runs (runs I-III). The monitor wafer was changed for each individual

run to observe if the increasing film thickness on the plastic sample would influence the outgassing in such a degree that changes could be seen in the properties of the ALD film. Therefore, the plastic samples had 900 cycles of AlO_x on them after all the runs, while all monitor samples had only 300 cycles on them. The difference between each monitor sample was that the thickness of the AlO_x on the plastic sample placed on top of the wafer was different.

ALD film thickness and density were determined from the monitor samples using X-ray reflectometry (XRR) (PANalytical X'Pert) in four areas per wafer to study how the potential outgassing from the plastic pieces would influence the growth rate and density of the AlO_x film on silicon. This provides indirect information on the amount of outgassing from the plastics, as volatile compounds potentially perturb the precursor flow over the samples. The thickness map was created with an ellipsometer (J.A. Woollam M2000UI) scan of full wafer area giving better thickness data compared to the XRR analysis. Additionally, a J.A. Woollam V-VASE spectroscopic ellipsometer was used at angles 65° , 70° and 75° (wavelength = 300 to 900nm in steps of 10nm) to determine refractive index at certain selected points which were shown to have similar thickness.

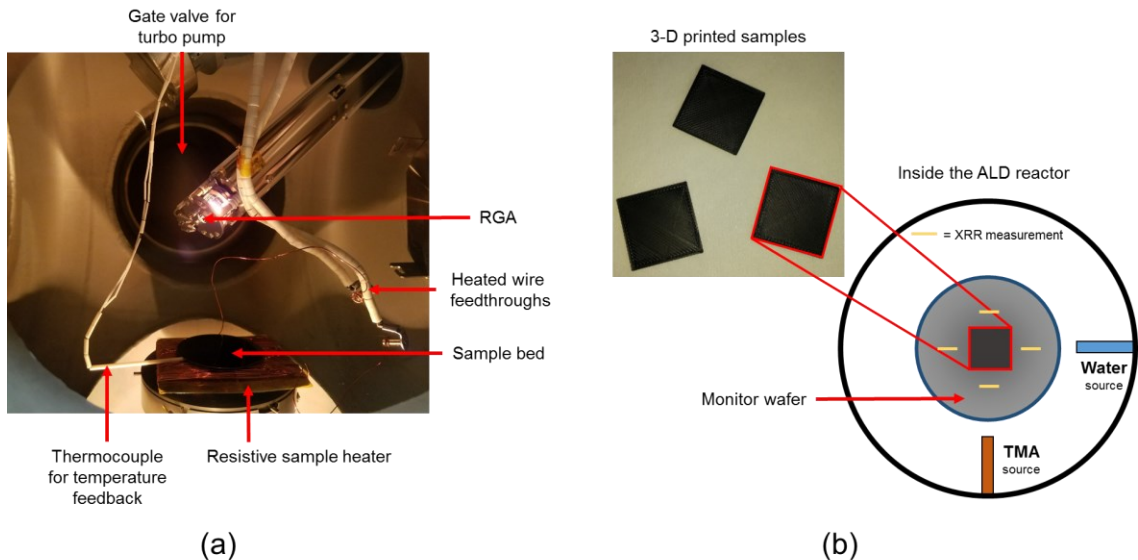


Figure 3.1: (a) Modified load lock of MBE system showing sample heater, polymer sample and RGA. (b) 3-D printed 30 mm \times 30 mm \times 1 mm plastic samples were placed on a silicon wafer inside the ALD chamber. The yellow lines mark the locations where the ALD AlO_x film thickness and density were measured with XRR. The thickness of the AlO_x film was also mapped across the whole monitor wafer with ellipsometry.

3.3 Results

Thickness measurements on the monitor Si wafers confirmed that the presence of both ABS and PC made the AlO_x film grow non-uniformly. In the reference deposition, in which

the 30 mm × 30 mm silicon piece was on top of the monitor wafer, the film thickness ranged from 39 nm (further away from the precursor inlets) to 46 nm (directly after the inlets). During the initial depositions on ABS and PC samples, a more severe disruption of the film growth on the monitor wafers compared to the square silicon sample was observed. Pictures of the wafers and the respective thickness maps are shown in Figure 3.2, and it was observed that the AlO_x film did not grow uniformly on the surface of the monitor wafer. There was higher growth in the area near the TMA inlet and lower on its opposite side. Around the edges of the plastic samples, highly irregular growth that was limited around and below the samples was observed. With each consequent step of the deposition, the uniformity of the film on the monitor wafer improved slightly, which suggested changes in the outgassing, the surface properties of the plastic, or introduction of new alumina nucleation sites that contribute to the outgassing barrier properties. XRR measurements on the monitor samples revealed that film density remained essentially constant (values) among the four measurement areas for both ABS and PC in all monitor wafers.

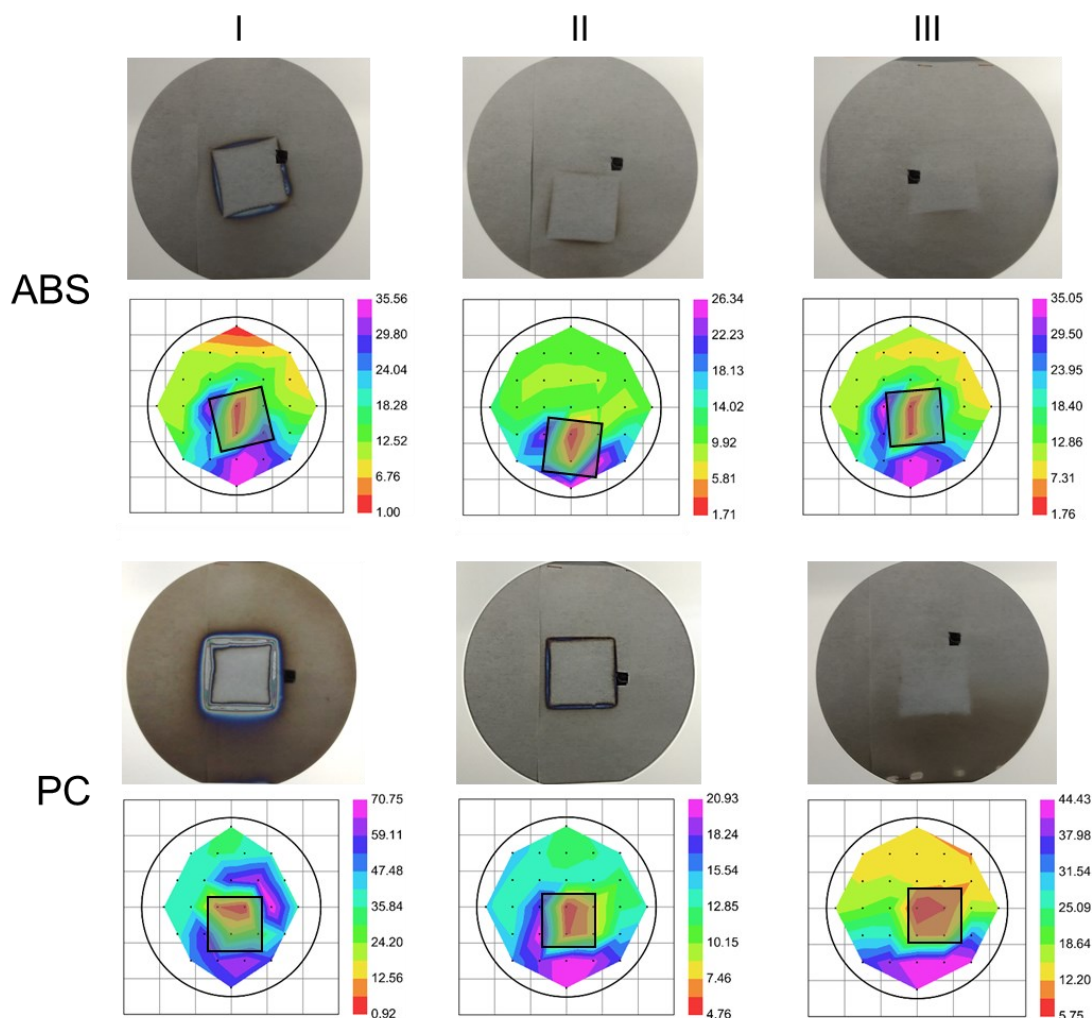


Figure 3.2: Photographs and ellipsometry maps of the monitor wafer after each sequential (I-III) ALD run for ABS and PC. The thickness maps close to the plastic sample position are not accurate because of uncontrolled film deposition. The non-uniformity of the deposition is clear in both photos and ellipsometer maps. The thickness scale [nm] is on the right of each map.

Characterization of the 3-D printed plastics revealed that both materials were highly porous. Based on the BET analysis, the specific surface area of uncoated ABS was $0.91 \text{ m}^2/\text{g}$, while for PC it was $1.08 \text{ m}^2/\text{g}$. SEM images of the cryofractured ABS and PC cross sections are shown in **Figure 3.3**. The average pore diameter in PC was approximately 500 nm, while the pore size distribution in ABS was much larger, ranging from the nanometer to the micrometer range. Based on the SEM images, it was estimated that the pores accounted for approximately 28% of the volume of the ABS sample, while for PC $\sim 56\%$ of the volume comprised of pores. When uncoated ABS and PC samples were loaded into the testing chamber and pumped down, the base pressure of the system did not get down

to a level low enough for the RGA to function. Therefore, the need for reduction of outgassing from both ABS and PC was evident in order to use them in vacuum applications.

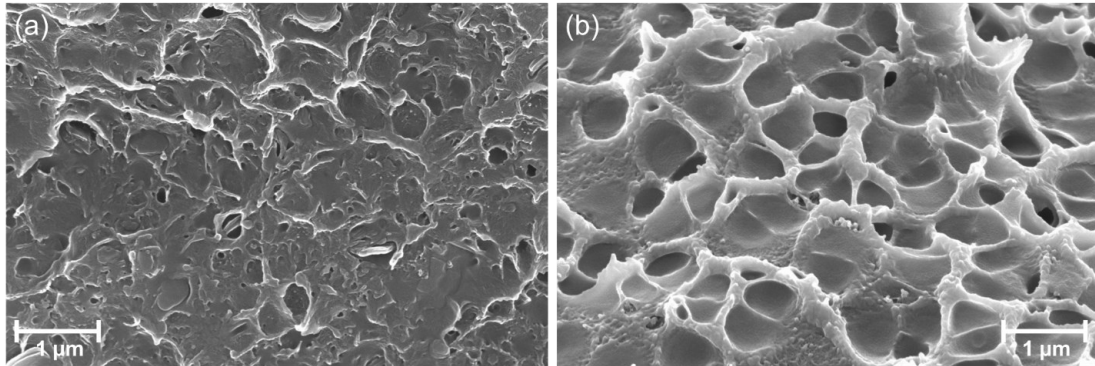


Figure 3.3: SEM micrographs of cryo-fractured cross-sections of uncoated 3-D printed (a) ABS and (b) PC, showing porous structures.

Coating the plastics with an approximately 7 μm thick layer of the commercial vacuum resin smoothed the surfaces substantially, as seen for the resin-coated PC sample in **Figure 3.4(a)**. The resin had partially penetrated the porous surface, and the pore size seemed to increase towards the bulk of the sample. SEM images of the PC surface show both surface cracks and point defects on the resin layer (**Figure 3.4(b)** and **Figure 3.4(c)**), which indicated that the application of the resin and the curing process were not optimal to achieve perfect surface coverage.

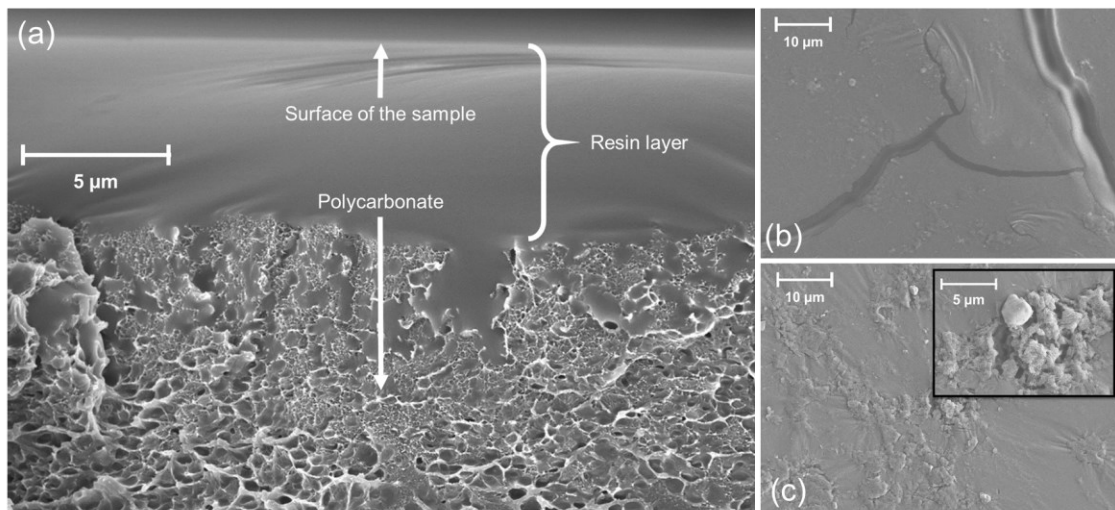


Figure 3.4: Cryo-fractured cross-section of 3-D printed PC sample, coated with the commercial vacuum resin. The image shows partial penetration of the resin into the pores of the plastic. Pore size was smaller close the surface of the sample than in the bulk. (b) PC surface showing cracks in the vacuum resin. (c) Accumulation of resin on the PC surface with the inset showing a magnified view of resin clusters.

SEM images and EDS analysis of the ALD-coated plastics revealed that the AlO_x coating was fully conformal on the surface of PC, whereas the surface of ABS exhibited regions devoid of an oxide coating (**Figure 3.5**). ALD layers on both polymers were found to include 3-D growth, with clusters of AlO_x appearing to grow vertically from the film surfaces (**Figure 3.5** and **Figure 3.6**). EDS confirmed the composition of the observed particulates to be a majority of Al and O, suggesting that they were monocrystals or polycrystals of AlO_x . The particles had a diameter of 1-2 μm . The presence of particulates suggests that the layer-by-layer reaction sequence characteristic to ALD growth was interrupted. It is possible that TMA and water molecules desorbed from the polymers reacted with each other in the gas phase, subsequently precipitating, or free water vapor pre-emptively reacted with TMA adsorbed to the polymer surface during the precursor stage of the ALD cycle.

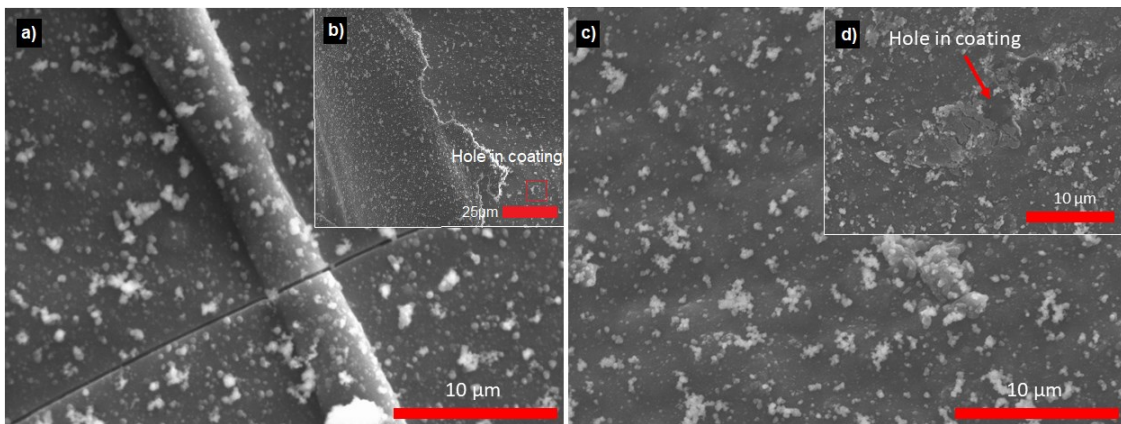


Figure 3.5: SEM image of (a) PC ALD coating (BSE image), (b) inset image of hole in PC ALD coating, (c) ABS ALD coating (BSE image), (d) inset image of hole in ABS ALD coating.

The presence of fracture in the ALD layer on the PC samples is telling of the layer's uniform mechanical properties and contiguousness. No fractures were noted in the ALD on the ABS sample's surface, which further exemplifies the non-contiguous nature of the film as shown in **Figure 3.5**, having sizeable gaps in the film.

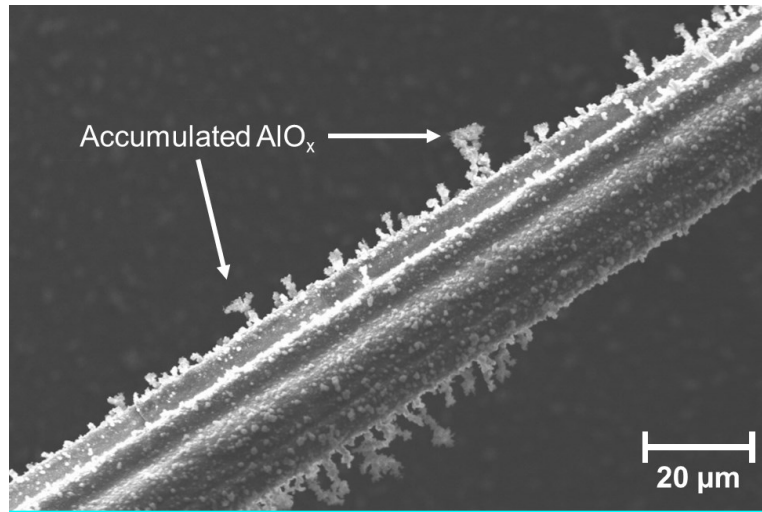


Figure 3.6: SEM image of a strand of PC, coated with 900 cycles of AlO_x. Instead of growing as a uniform film, the AlO_x had accumulated on the plastic surface as micron-sized particles and whiskers.

Subsurface crystallites of AlO_x were observed in both polymers, contained mostly within a depth of 5 μm relative to the ALD coating/polymer interface. Due to the small size of the pores in each polymer, it was difficult to determine if a direct association between subsurface crystallites and pores existed, but the size of the crystallites in the PC sample seems to corroborate this possibility.

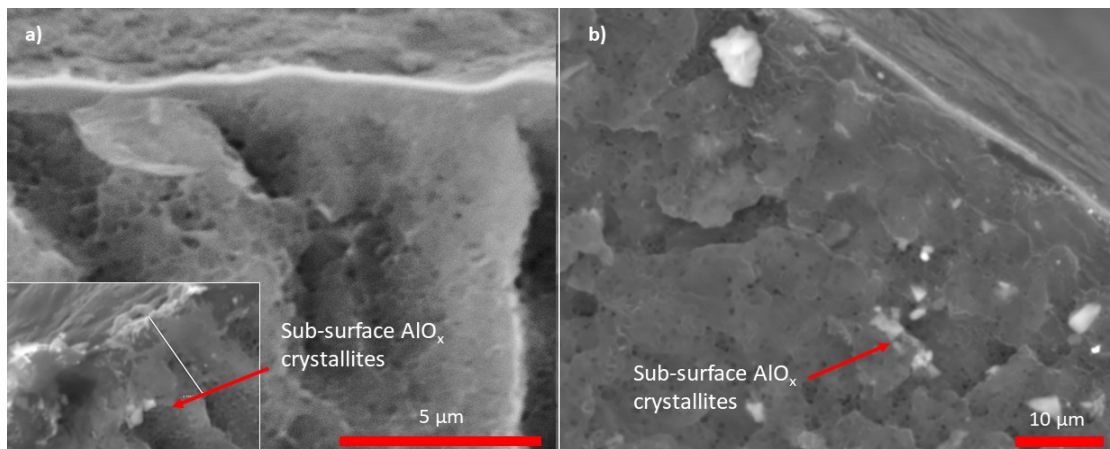


Figure 3.7: Backscattered SEM cross section images of (a) black ABS with ALD coating and (b) black PC ALD coating. Note the presence of sub-surface AlO_x crystallites, identified via EDS. An example EDS line scan path is presented in the sub-set image for the black ABS image.

Both ALD-coated polymers showed sub-surface agglomerates of AlO_x , with similar penetration depth of Al and O, as determined from EDS line scans (**Figure 3.8**). Line scans locations were chosen to avoid subsurface crystallites, in order to sample the bulk subsurface composition. The presence of subsurface Al $K\alpha$ and enhanced O $K\alpha$ signal is assumed to result from the presence of subsurface AlO_x crystallites, dispersed finely in the matrix (distinct from the agglomerates shown in **Figure 3.7**). The higher O $K\alpha$ signal in the PC sample relative to the ABS sample at increasing depths from the coating surface reflects the presence of O in the structure of the polymer. Another notable difference between the EDS line scans is the continual increase in C $K\alpha$ signal with depth from the ALD layer, as we go deeper into the sample.

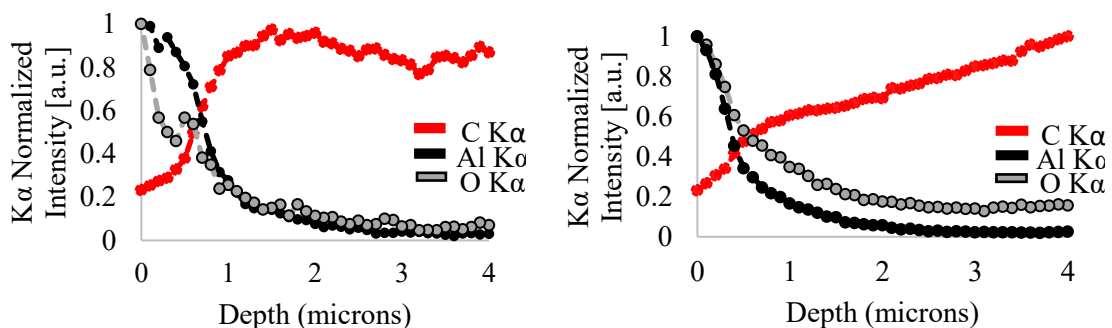


Figure 3.8: Depth profiles of C, O, and Al $K\alpha$ signal from EDS line scan (left: black ABS, right: black PC). Depth measured as linear distance from the maximum Al $K\alpha$ signal position (assumed to be the centreline of the AlO_x coating). Line scans were taken with an accelerating voltage of 15 kV and each elemental $K\alpha$ profile is normalized to the maximum intensity within the sampling length.

After coating the samples and the preparation procedures, the outgassing from all samples was analysed with the RGA setup. For resin- and ALD-coated ABS and both resin-containing PC samples, the summed partial pressure of all outgassing species increased with temperature. This led to a substantial increase in total chamber pressure, and a very high filament current was registered at temperatures over 80°C for resin-coated ABS, over 50°C for resin- and ALD-coated PC and over 60°C for resin-coated PC. In order to protect the RGA from damage, data collection from these samples was terminated at the aforementioned temperatures.

The sum of the normalized partial pressures from 1 to 100 AMU for each temperature are presented in Figure 3.9(a) for ABS and Figure 3.9(b) for PC. For both plastics, the outgassing level of the ALD-coated remained the lowest at all temperatures. The outgassing from the resin-coated ABS was the highest of all ABS samples until 60°C , after which the resin- and ALD-coated sample showed a sudden increase in outgassing. Above 70°C , the outgassing from resin-coated ABS started to decrease, but the outgassing level was still higher at 100°C than that of the ALD-coated samples. Similar to ABS, the resin-coated PC samples showed the highest outgassing level, and the outgassing from the resin-

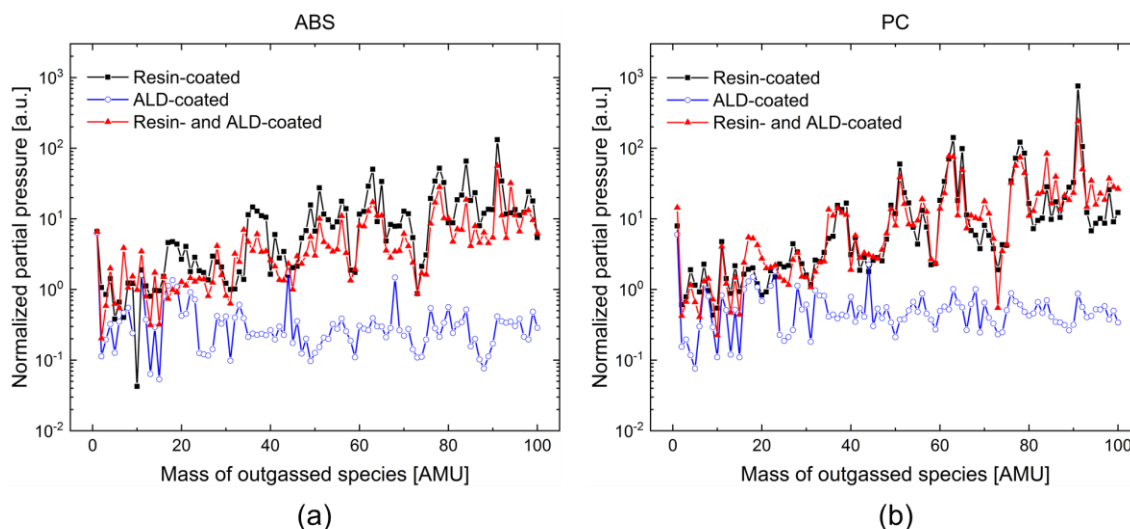


Figure 3.10: A comparison of outgassing characteristics of coated ABS (a) and PC (b) samples at molecular masses 1 to 100 AMU at 50 °C, showing a consistently low value for the ALD-coated samples.

3.4 Discussion

3-D printed polymers are known to have high porosity due to voids present in the microstructure [31-33]. While the presence of these voids can be exploited to tune mechanical properties for various biological applications [34], the high porosity and specific surface area of both 3-D printed ABS and PC posed a challenge for their use in vacuum applications, as the uncoated polymers had such a high level of outgassing that the RGA measurements could not be conducted. The pores in the material had the potential to trap atmospheric contaminants that likely escaped in the presence of vacuum. Coating the 3-D printed plastics with either a commercial vacuum sealing resin or ALD AlO_x reduced the outgassing to a level that was measurable with the employed setup. Resin-coated ABS exhibited a lower total amount of outgassing compared to PC. The higher porosity and higher specific surface area of PC potentially contributed to higher adsorption of ambient gases, resulting in serious outgassing of atmospheric contaminants under vacuum. The resin did not provide a uniform and durable coverage of the plastic surfaces, seen as cracks on the PC surface. This effect was seen to a comparatively lower extent in ABS due to its lower porosity.

A potential explanation for the decrease of pore size at the surface is the curing procedure, as at 95°C the plastics could have softened even below the glass transition temperature. SEM micrographs of the surfaces coated with the vacuum resin showed cracking, which appeared when the solvent was driven off using a baking process at elevated temperature to cure the resin. This cracking was attributed to the possible large thickness of the resin, due to which it could not be cured effectively. Hence, when the solvents were drawn out, the polymer potentially contracted and clusters of the resin could be seen on the surface.

This problem may be mitigated by gradually heating the sample to eliminate the possibility of thermal shock.

Based on the deposition on a 30 mm × 30 mm Si sample on top of a monitor wafer, it was concluded that the physical presence of the sample in the middle of the deposition area influenced the film uniformity. Based on previous studies, even minor changes to the sample placement inside the reactor can affect the gas flow on top of the wafer [35]. In the course of the AlO_x depositions, it was observed that the plastics disrupted the growth of the film. The species that outgassed from the plastics were likely parts of both ABS and PC polymer chains. These hydrocarbons speculatively adsorbed to the substrate surface of the monitor Si wafer during deposition, preventing TMA molecules from reaching the active surface OH-sites. This reduced the film thickness across the wafer. On all the four sides of the chamber, there were inlets with a constant flow of N₂ carrier gas that moved the outgassed products all over the chamber, disrupting the deposition more the further from the precursor inlet. A higher growth area did not appear in front of the water inlet suggesting that the water reaches further away from the inlet compared to TMA. On the other hand, uncontrollably rapid growth was observed in the initial deposition in areas that were in contact with the plastics. A likely explanation for this is the adsorption of water during the water pulse into the porous structure of the plastic, and its subsequent release during the TMA pulsing steps. TMA molecules reacted with the higher excess water molecules around the plastic in the gas phase. The gradual release of water led to high film thickness localized to the edges of the plastics and reducing the film uniformity. The presence of water vapor during the TMA pulse also explains the formation of the AlO_x clusters that were deposited on the surface of the plastics. As these particulates can be difficult to remove from vacuum systems, their formation should be suppressed by lengthening the purge step in the ALD process when coating porous substrates.

Despite the non-optimal ALD process, the uniformity of the film that was deposited on the monitor wafer improved with increasing AlO_x thickness on the plastic. This can be attributed to the reduction of outgassing and lower amount of water adsorption to the surface of the plastic, which was seen as reduced amount of uncontrolled growth around the edges of the sample. The physical presence of the plastic likely played a role in decreasing the uniformity of the film away from the precursor's inlets, but its effect was difficult to detect in these depositions, since the outgassing and water absorption likely had a larger influence on the film uniformity in the initial depositions. However, in run III, the disruption of precursor flows due to the physical shape of the sample might have started to influence the film uniformity.

The outgassing characteristics were the least favourable for the resin-coated samples. However, it should be noted that the resin did reduce the outgassing enough for both materials to be measured by the RGA. Intermediate outgassing characteristics were observed for the ALD-coated samples that also had vacuum resin on them. It was speculated that although the resin is meant for vacuum applications, its incomplete curing can cause continued outgassing. The resin manufacturer [36] states that the recommended curing temperature of this product is 200°C, and room temperature curing, while possible, is not recommended. Since the plastics would melt at such a high temperature, curing was

done at 95°C, which was below the glass transition temperature of both plastics. This may have been insufficient for this purpose, as the amount of outgassing continued to decrease from resin-coated ABS at temperatures above 70°C. In addition, as the resin was applied to the plastic samples using the brush provided by the manufacturer, it is probable that a too thick layer was deposited, leading to insufficient curing.

The solvents in the vacuum resin potentially continued to outgas during the RGA tests. While the precise composition of the sealant was not available, the concentration of xylene was the highest in the proprietary mixture [37], other constituents being ethylbenzene and toluene. As a preliminary test, the known mass spectrums of p-xylene, ethylbenzene and toluene [38] were compared to the partial pressure data obtained from resin-coated ABS and PC samples. The highest peak at molecular mass 91 AMU was matched to all three of these compounds. In addition, a minor peak at 67 AMU was also matched to xylene. This indicated the need to sufficiently cure the sealant to drive off solvents before use in a vacuum environment. With the curing protocol used in this study, the commercial vacuum cleaning resin is not recommended as a coating to prevent outgassing of FFF-based 3-D printed vacuum components. Instead, substantial outgassing reduction from 3-D printed plastics could be obtained with ALD AlO_x, even with a non-optimal growth process.

The collected outgassing data indicated that ABS had better overall outgassing characteristics than PC, as the resin-coated ABS samples had consistently lower normalized partial pressure values for outgassed species with molecular masses in the range of 1-100 AMU than PC. One of the NASA standard metrics to quantify outgassing is water vapour regained (WVR) [39]. 3-D printed ABS has a higher WVR value (0.25%) compared to PC (0.14%) [40]. In fact, it has been reported that at least 80% out of all gas absorbed in ABS is water vapour [41] and that most water vapour selectively outgasses in the mTorr pressure range [42-43]. In this study, all outgassing data was collected below 1 mTorr, indicating that ABS had dehydrated more effectively. The presence of other gases in PC, such as CO₂, CO and H₂ [44], and their slow removal rates may have contributed to its undesirable outgassing characteristics. However, the ALD AlO_x coating significantly reduced the amount of outgassing from both materials, enabling the use of plastics with beneficial thermal tolerance but poor outgassing properties in vacuum systems operating in the mTorr range.

While the coatings may serve as adequate barriers against outgassing, any defects in the coating will allow volatile organic compounds as well as particulate carbon black to escape and potentially contaminate the vacuum system. Hence, more detailed characterization of the outgassed species of ALD-coated FFF plastics is required to ensure that the plastic parts used in a vacuum chamber would not contaminate the system. Uncoloured 3-D printed plastics would be preferable materials for vacuum components.

The reason why the ALD-coated samples remarkably exhibited the lowest level of outgassing can potentially be attributed to the reduction of surface area and water adsorption capability by the AlO_x clusters seen in the SEM images. However, the exact mechanism for outgassing reduction by ALD AlO_x was not unveiled in these studies, and this issue is to be addressed in further studies. The density of the ALD AlO_x films was

constant from run to run with or without the plastic inside the reactor. This was an indirect indication that the outgassed species were not incorporating into the film during the growth. XPS measurements on the AlO_x films showed that carbon had only incorporated into the top ~ 5 nm of the film, which was attributed to atmospheric contamination present in all samples. This, in turn confirmed that the outgassed hydrocarbons from the plastics did not react chemically with the precursors used in this process. This was verified by measuring the refractive index at certain spots with similar thickness. In areas with thickness ≈ 20 nm, the refractive index was found to be ≈ 3 at 600 nm.

The printing parameters for these materials may be altered to reduce the porosity of the printed components. Some degree of over-extrusion coupled with heat treatments could provide a smoother surface, which would be less prone to outgassing and vapour absorption. Apart from ALD coated ABS and PC that have potential for use in vacuum environments [40], ALD coated polypropylene (PP) may also be utilized in 3-D printed vacuum processing tools because of its chemical inertness [29], cleanroom compatibility [45] and higher crystallinity [46].

More work is required to confirm the physical mechanisms behind the reduction of outgassing, and in future experiments focusing on this, a PID controlled heater could be used in the vacuum system to keep the ramp rate consistent across all the ten-degree increments. In addition, a spacer could be used to elevate the sample during outgassing tests so that the distance between the sample and the RGA is reduced. Further studies are also needed to determine the long-term stability of the outgassing reduction using ALD coatings, as the underlying 3-D printed plastic and AlO_x have different thermal expansion coefficients. Repeated thermal cycling from low to high temperature can lead to fracturing of the ALD film and impair the outgassing properties of the plastic.

3.5 Conclusions

The reduction of outgassing from affordable FFF-based 3-D printed ABS and PC using a commercial vacuum sealing resin and an inorganic ALD AlO_x coating was demonstrated, providing a basis for using commercial 3-D printed plastics in vacuum applications. Resin-coated ABS had better outgassing properties than resin-coated PC, which was attributed to the lower porosity and specific surface area of ABS compared to PC. However, an ALD AlO_x coating with thickness in the order of hundreds of nanometres was shown to significantly reduce the outgassing from both ABS and PC. The 3-D printed plastics disturbed the growth of the ALD film potentially due to outgassing and precursor adsorption into the sample surface, but their influence gradually reduced with increasing ALD coating thickness. Outgassing analysis showed that inorganic ALD AlO_x coatings effectively reduced outgassing from both ABS and PC, even with uneven and non-conformal coverage of the plastics. The vacuum sealing resin was not as effective as the ALD coatings in reducing the outgassing, likely because a non-optimal curing process had to be used due to the limited thermal resilience of the 3-D printed plastics. The results

presented in this study provide a clear basis for using affordable FFF-based plastic components in vacuum chambers.

3.6 Acknowledgments

This work was partially supported by Fulbright Finland, the Witte endowment and Aleph Objects. The authors acknowledge the provision of facilities by Aalto University at OtaNano – Micronova Nanofabrication Centre and at the RawMatTERS (RAMI) facilities, and the Applied Chemical and Morphological Analysis Laboratory at Michigan Tech for use of the instruments and staff assistance. Parts of this study were completed using Michigan Technological University's Microfabrication Facility. I.T.S.H. acknowledges the financial support from Aalto ELEC Doctoral School and Walter Ahlström foundation. G.M. and M.K. gratefully acknowledge funding from the Strategic Research Council at the Academy of Finland (CloseLoop Consortium, Grant No. 303452).

3.7 References

- [1] Pearce, J. (2012). Building Research Equipment with Free, Open-Source Hardware. *Science*, 337(6100), pp.1303-1304. doi.org/10.1126/science.1228183
- [2] Pearce, J.M., 2013. *Open-source lab: how to build your own hardware and reduce research costs*. Newnes.
- [3] Pearce, J.M., 2014. Laboratory equipment: Cut costs with open-source hardware. *Nature*, 505(7485), p.618. doi.org/10.1038/505618d
- [4] Pearce, J.M., 2015. Return on investment for open source scientific hardware development. *Science and Public Policy*, 43(2), pp.192-195. doi.org/10.1093/scipol/scv034
- [5] Baden, T., Chagas, A.M., Gage, G., Marzullo, T., Prieto-Godino, L.L. and Euler, T., 2015. Open Labware: 3-D printing your own lab equipment. *PLoS biology*, 13(3), p.e1002086. doi.org/10.1371/journal.pbio.1002086
- [6] Dhankani, K.C. and Pearce, J.M., 2017. Open source laboratory sample rotator mixer and shaker. *HardwareX*, 1, pp.1-12. doi.org/10.1016/j.ohx.2016.07.001
- [7] Trivedi, D. and Pearce, J., 2017. Open source 3-D printed nutating mixer. *Applied Sciences*, 7(9), p.942. doi.org/10.3390/app7090942
- [8] da Costa, E.T., Mora, M.F., Willis, P.A., do Lago, C.L., Jiao, H. and Garcia, C.D., 2014. Getting started with open-hardware: Development and control of microfluidic devices. *Electrophoresis*, 35(16), pp.2370-2377. doi.org/10.1002/elps.201400128

- [9] Bhattacharjee, N., Urrios, A., Kang, S. and Folch, A., 2016. The upcoming 3D-printing revolution in microfluidics. *Lab on a Chip*, 16(10), pp.1720-1742. doi.org/10.1039/C6LC00163G
- [10] Morgan, A.J., San Jose, L.H., Jamieson, W.D., Wymant, J.M., Song, B., Stephens, P., Barrow, D.A. and Castell, O.K., 2016. Simple and versatile 3D printed microfluidics using fused filament fabrication. *PloS one*, 11(4), p.e0152023. doi.org/10.1371/journal.pone.0152023
- [11] Pearce, J.M., Anzalone, N.C. and Heldt, C.L., 2016. Open-source wax RepRap 3-D printer for rapid prototyping paper-based microfluidics. *Journal of laboratory automation*, 21(4), pp.510-516. doi.org/10.1177/2211068215624408
- [12] Maldonado-Torres, M., López-Hernández, J.F., Jiménez-Sandoval, P. and Winkler, R., 2014. ‘Plug and Play’ assembly of a low-temperature plasma ionization mass spectrometry imaging (LTP-MSI) system. *Journal of proteomics*, 102, pp.60-65. doi.org/10.1016/j.jprot.2014.03.003
- [13] Gans, A.R., Jobbins, M.M., Lee, D.Y. and Alex Kandel, S., 2014. Vacuum compatibility of silver and titanium parts made using three-dimensional printing. *Journal of Vacuum Science & Technology A: Vacuum, Surfaces, and Films*, 32(2), p.023201. doi.org/10.1116/1.4846195
- [14] Povilus, A.P., Wurden, C.J., Vendeiro, Z., Baquero-Ruiz, M. and Fajans, J., 2014. Vacuum compatibility of 3D-printed materials. *Journal of Vacuum Science & Technology A: Vacuum, Surfaces, and Films*, 32(3), p.033001. doi.org/10.1116/1.4873556
- [15] Zwicker, A.P., Bloom, J., Albertson, R. and Gershman, S., 2015. The suitability of 3D printed plastic parts for laboratory use. *American Journal of Physics*, 83(3), pp.281-285. doi.org/10.1119/1.4900746
- [16] Rivera, W.F. and Romero-Talamás, C.A., 2016. Vacuum compatibility of 3-d-printed parts. *IEEE Transactions on Plasma Science*, 44(5), pp.874-876. doi.org/10.1109/TPS.2016.2540924
- [17] Chaneliere, T., 2017. Vacuum compatibility of ABS plastics 3D-printed objects. CNRS, Laboratoire Aimé Cotton.
- [18] Minton, T.K., Wu, B., Zhang, J., Lindholm, N.F., Abdulagatov, A.I., O’Patchen, J., George, S.M. and Groner, M.D., 2010. Protecting polymers in space with atomic layer deposition coatings. *ACS applied materials & interfaces*, 2(9), pp.2515-2520. doi.org/10.1021/am100217m
- [19] Kestilä, A., Nordling, K., Miikkulainen, V., Kaipio, M., Tikka, T., Salmi, M., Auer, A., Leskelä, M. and Ritala, M., 2018. Towards space-grade 3D-printed, ALD-coated small

satellite propulsion components for fluidics. *Additive Manufacturing*, 22, pp.31-37. doi.org/10.1016/j.addma.2018.04.023

[20] Groner, M.D., George, S.M., McLean, R.S. and Carcia, P.F., 2006. Gas diffusion barriers on polymers using Al₂O₃ atomic layer deposition. *Applied Physics Letters*, 88(5), p.051907. doi.org/10.1063/1.2168489

[21] Ferguson, J.D., Weimer, A.W. and George, S.M., 2004. Atomic layer deposition of Al₂O₃ films on polyethylene particles. *Chemistry of materials*, 16(26), pp.5602-5609. doi.org/10.1021/cm040008y

[22] Wilson, C.A., Grubbs, R.K. and George, S.M., 2005. Nucleation and growth during Al₂O₃ atomic layer deposition on polymers. *Chemistry of Materials*, 17(23), pp.5625-5634. doi.org/10.1021/cm050704d

[23] Hirvikorpi, T., Vähä-Nissi, M., Mustonen, T., Iiskola, E. and Karppinen, M., 2010. Atomic layer deposited aluminum oxide barrier coatings for packaging materials. *Thin Solid Films*, 518(10), pp.2654-2658. doi.org/10.1016/j.tsf.2009.08.025

[24] Parsons, G.N., Atanasov, S.E., Dandley, E.C., Devine, C.K., Gong, B., Jur, J.S., Lee, K., Oldham, C.J., Peng, Q., Spagnola, J.C. and Williams, P.S., 2013. Mechanisms and reactions during atomic layer deposition on polymers. *Coordination Chemistry Reviews*, 257(23-24), pp.3323-3331. doi.org/10.1016/j.ccr.2013.07.001

[25] Tanikella, N.G., Wittbrodt, B. and Pearce, J.M., 2017. Tensile strength of commercial polymer materials for fused filament fabrication 3D printing. *Additive Manufacturing*, 15, pp.40-47. doi.org/10.1016/j.addma.2017.03.005

[26] Puri, B.R. and Bansal, R.C., 1964. Studies in surface chemistry of carbon blacks. Part I. High temperature evacuations. *Carbon*, 1(4), pp.451-455. [doi.org/10.1016/0008-6223\(64\)90006-5](https://doi.org/10.1016/0008-6223(64)90006-5)

[27] <https://www.openscad.org/> (Retrieved: 4/4/19).

[28] Vacseal, www.vacseal.com (Retrieved: 4/4/19).

[29] Heikkinen, I.T.S., Kauppinen, C., Liu, Z., Asikainen, S.M., Spoljaric, S., Seppälä, J.V., Savin, H. and Pearce, J.M., 2018. Chemical compatibility of fused filament fabrication-based 3-D printed components with solutions commonly used in semiconductor wet processing. *Additive Manufacturing*, 23, pp.99-107. doi.org/10.1016/j.addma.2018.07.015

[30] Brunauer, S., Emmett, P.H. and Teller, E., 1938. Adsorption of gases in multimolecular layers. *Journal of the American chemical society*, 60(2), pp.309-319. doi.org/10.1021/ja01269a023

- [31] Wang, X., Zhao, L., Fuh, J.Y.H. and Lee, H.P., 2019. Effect of Porosity on Mechanical Properties of 3D Printed Polymers: Experiments and Micromechanical Modeling Based on X-Ray Computed Tomography Analysis. *Polymers*, 11(7), p.1154. doi.org/10.3390/polym11071154
- [32] Rodriguez, J.F., Thomas, J.P. and Renaud, J.E., 2000. Characterization of the mesostructure of fused-deposition acrylonitrile-butadiene-styrene materials. *Rapid Prototyping Journal*, 6(3), pp.175-186. doi.org/10.1108/13552540010337056
- [33] Bellehumeur, C., Li, L., Sun, Q. and Gu, P., 2004. Modeling of bond formation between polymer filaments in the fused deposition modeling process. *Journal of Manufacturing Processes*, 6(2), pp.170-178. [doi.org/10.1016/S1526-6125\(04\)70071-7](https://doi.org/10.1016/S1526-6125(04)70071-7)
- [34] Lam, C.X.F., Mo, X.M., Teoh, S.H. and Hutmacher, D.W., 2002. Scaffold development using 3D printing with a starch-based polymer. *Materials Science and Engineering: C*, 20(1-2), pp.49-56. [doi.org/10.1016/S0928-4931\(02\)00012-7](https://doi.org/10.1016/S0928-4931(02)00012-7)
- [35] Peltonen, P., Vuorinen, V., Marin, G., Karttunen, A.J. and Karppinen, M., 2018. Numerical study on the fluid dynamical aspects of atomic layer deposition process. *Journal of Vacuum Science & Technology A: Vacuum, Surfaces, and Films*, 36(2), p.021516. doi.org/10.1116/1.5018475
- [36] Application Notes on Vacseal, <https://www.2spi.com/catalog/documents/Vacseal-App-Notes.pdf> (Retrieved: 4/4/19).
- [37] Vacseal SDS, <http://www.vacseal.net/wp-content/uploads/2017/08/GHS-SDS-Vacseal-II-High-Vacuum-Sealant-clear-Liquid-7-15-2016.pdf> (Retrieved: 4/4/19).
- [38] NIST Webbook, <https://webbook.nist.gov/> (Retrieved: 4/4/19).
- [39] Walter, N.A. and Scialdone, J.J., 1997. Outgassing Data for Selecting Spacecraft Materials. Revision 4. NASA NTRS.
- [40] NASA Outgassing Database, <https://outgassing.nasa.gov/> (Retrieved: 4/4/19).
- [41] Sefa, M., Ahmed, Z., Fedchak, J.A., Scherschligt, J. and Klimov, N., 2016. Gas uptake of 3D printed acrylonitrile butadiene styrene using a vacuum apparatus designed for absorption and desorption studies. *Journal of Vacuum Science & Technology A: Vacuum, Surfaces, and Films*, 34(6), p.061603. doi.org/10.1116/1.4965304
- [42] Grinham, R. and Chew, A., 2017. A Review of Outgassing and Methods for its Reduction. *Applied Science and Convergence Technology*, 26(5), pp.95-109. doi.org/10.5757/ASCT.2017.26.5.95

- [43] G.P. Beukema, *Cursus Vacuumtechnologie* (2016) (Retrieved: 12/12/16).
- [44] Norton, F.J., 1963. Gas permeation through Lexan polycarbonate resin. *Journal of Applied Polymer Science*, 7(5), pp.1649-1659. doi.org/10.1002/app.1963.070070507
- [45] Pasanen, T.P., von Gastrow, G., Heikkinen, I.T., Vähänissi, V., Savin, H. and Pearce, J.M., 2019. Compatibility of 3-D printed devices in cleanroom environments for semiconductor processing. *Materials Science in Semiconductor Processing*, 89, pp.59-67. doi.org/10.1016/j.mssp.2018.08.027
- [46] Sugimoto, M., Ishikawa, M. and Hatada, K., 1995. Toughness of polypropylene. *Polymer*, 36(19), pp.3675-3682. [doi.org/10.1016/0032-3861\(95\)93769-I](https://doi.org/10.1016/0032-3861(95)93769-I)

4 Vacuum Outgassing Characteristics of Unpigmented 3-D Printed Polymers Coated with ALD Alumina

3-D printing offers enormous potential for fabricating custom equipment for space and vacuum systems, but in order to do this at low-costs, polymers are necessary. Historically polymers have not been unsuited for these applications because of outgassing, but if coated with a conformal, inorganic film introduced with atomic layer deposition (ALD), then outgassing can be reduced. Previous work showed promise with heavily outgassing carbon black containing 3-D printed polymers. In this study, ALD aluminum oxide and a commercially available vacuum sealant resin were used to coat clear, acrylonitrile butadiene styrene (ABS), polycarbonate (PC) and polypropylene (PP). Characterization of the films included spectroscopic ellipsometry for thickness, microstructure analysis with scanning electron microscopy, chemical analysis with energy-dispersive X-ray spectroscopy, and residual gas analysis for outgassing quantification. ALD-coated samples registered lower pressures than the resin-coated ones. The results showed that the ALD coatings could effectively inoculate unpigmented 3-D printed plastics, which could be used in contamination-sensitive environments such as semiconductor processing systems and space environments.

4.1 Introduction

Additive manufacturing is radically changing the way polymer-based components are manufactured [1-5], which enables the customization of 3-D printed components to meet individual user needs. Customization with 3-D printing has significantly reduced costs and led to unprecedented growth in the acceptance and use of polymers in scientific research equipment [6-9]. 3-D printed parts allow for versatile design and manufacture of custom parts at relatively low expense by low to moderately skilled workers [10-12] and a high return on investment for labs that deploy them [13]. Despite the ubiquity of 3-D printed materials in research applications, including recent inroads into clean room environments [14-15]; they have remained largely absent from semiconductor research, primarily due to their apparent incompatibility with vacuum equipment. This assumed incompatibility arises from off-gassing of polymers when exposed to vacuum conditions, chemical degradation driven by exposure to charged and high kinetic energy particles, as well as ultraviolet radiation used in some semiconductor processing systems.

The conditions experienced in vacuum systems for semiconductor processing are akin to those seen in space, where polymers degrade under exposure to ultrahigh vacuum, ultraviolet radiation, charged particles (plasma, electrons, protons), and atomic oxygen [16-19]. Mechanical degradation manifests as embrittlement of the material by initiation of stress concentrators by polymer decomposition, which can cause failure when polymer parts are under thermal cycling or tensile loads [20-22]. Off-gassing in polymers arises from the low molecular weight molecules present in the material matrix (e.g. unreacted monomers, solvents, plasticizers, antioxidants, coloring agents, and other processing aids are all common in commercial polymer material). When introduced to vacuum conditions,

these low molecular weight species, known as volatile organic compounds (VOCs) outgas [23-26]. This outgassing may result in lowered robustness through accelerated photo-degradation reactions in the polymer, as well as contamination of the surrounding system [27].

If polymers are coated with a conformal, inorganic film introduced with atomic layer deposition (ALD), outgassing can be reduced to a large extent, because the surface layer acts as a seal to prevent low molecular weight species present in the bulk of the material from escaping. This method of using ALD coatings as gas barriers [28-29] is known in the packaging industry, where aluminum oxide (AlO_x) and silicon oxide films are used as barrier layers to achieve relatively impermeable polymer-based structures [30-31], as well as with OLED encapsulation [32-34]. This work lays a strong foundation showing that transmission rates of volatiles through ALD coated polymers can be decreased immensely; supporting the potential for the application of 3-D printed polymer parts in vacuum systems and in space environments.

In addition to providing a barrier to volatile gas transmission, ALD layers have been shown to protect polymer layers from ionizing radiation and high kinetic energy particles [35]. The deposition of inorganic coatings on 3-D printed parts has the potential to seal air pockets and reduce the number of stress concentrators that lead to part failure [36-37]. Such stress concentrators may be formed due to particle impingement on either coated or uncoated components [38]. This research aims to understand the outgassing characteristics of 3-D printed polymers with ALD coatings and evaluate the efficacy of the coating in protecting the underlying polymer against very high vacuum, the most commonly seen ambient condition in semiconductor processing systems, and in space.

To limit gas diffusion in 3-D printed components, ALD AlO_x and a commercially available vacuum sealant resin, Vaseal [39], were chosen as potential coatings on clear, unpigmented acrylonitrile butadiene styrene (ABS), polycarbonate (PC) and polypropylene (PP). Previous research by the group using black colored ABS and PC [40] determined that outgassing is high when carbon black is used as pigment [41]. While an inorganic ALD coating on black polymer was successful in minimizing outgassing, the effects of using clear, unpigmented polymeric materials (and thus no artificially-enhanced outgassing) with these coatings are studied here. Characterization included spectroscopic ellipsometry for film thickness, microstructure analysis with scanning electron microscopy (SEM), chemical analysis with energy-dispersive X-ray spectroscopy (EDS), and residual gas analysis for outgassing quantification. This vacuum outgassing characterization is an important initial step for selecting a material that will be used to create open-source 3-D printable components, which could be used in contamination-sensitive environments such as semiconductor processing systems and space.

4.2 Experimental

Three types of clear, unpigmented materials were studied: acrylonitrile butadiene styrene (ABS), polycarbonate (PC) and polypropylene (PP). ABS was chosen because of its wide availability and ease of use [42], PC for its strength and thermal stability [43-45], and PP

for its chemical inertness [46]. The selected polymers exhibit a low percentage of total mass loss (TML) [47]. 3-D printed samples of the materials were coated with either ALD AlO_x or a commercial sealant, and their microstructure, chemical properties, and outgassing characteristics were analyzed. To ensure accurate comparison between different materials and coatings, the thermal history of all samples was carefully matched.

4.2.1 Sample preparation

ABS, PC and PP samples were fabricated using an open source Lulzbot Taz 6 fused filament fabrication (FFF) RepRap class 3-D printer (Aleph Objects, USA). The ABS filament was obtained from German RepRap GmbH (Feldkirchen, Germany), PC from Gizmo Dorks LLC (Temple City, California, USA) and PP from Ultimaker (Utrecht, The Netherlands). Sample dimensions were 30 mm \times 30 mm \times 1 mm. The printing parameters were set using open source Cura slicing software (21.08 Lulzbot edition), and the samples were printed with 100% infill with the parameters presented in **Table 4.1**. Both ABS and PP were printed directly onto the PEI surface of the print bed. In the case of PC, a thin layer of PVA-based glue was applied to the bed prior to printing to prevent the samples from adhering too tightly onto the print bed. After printing, the glue was carefully removed from the PC samples with disposable laboratory wipes dampened in water. Prior to further processing steps, all samples were cleaned by wiping them with cleanroom-compatible disposable wipes dampened in water and isopropanol. The samples were handled with nitrile gloves at all stages of the experiments.

Table 4.1: The printing parameters used to 3-D print the ABS, PC, and PP samples.

Plastic	Layer height (mm)	Shell thickness (mm)	Bottom/top thickness (mm)	Print speed (mm/s)	Top/bottom speed (mm/s)	Print T ($^{\circ}\text{C}$)	Bed T ($^{\circ}\text{C}$)	Minimal layer time (s)
ABS	0.15	1.0	0.8	60	60	245	95	15
PC	0.15	1.0	0.9	30	30	255	120	20
PP	0.18	1.0	1.08	50	10	235	60	15

The ABS, PC, and PP samples for the outgassing studies were prepared by coating the samples with either ALD AlO_x or Vacseal. The first sample set consisted of ALD-coated samples. AlO_x coatings were prepared with a Picosun R-100 top-flow ALD tool using trimethylaluminum ($\text{Al}(\text{CH}_3)_3$, TMA) and deionized water vapor as precursors and N_2 as carrier gas. The depositions were carried out at 80°C with a reactor pressure of 20 mTorr. The duration of the TMA pulse was 0.2 s, while the length of the water pulse was 0.5 s. The purging time between each precursor pulse was 5.0 s. In order to characterize the film growth, silicon wafers (Okmetic Oy, 100 mm, n-type, 512 μm , (100) orientation) were used as monitor samples. In an individual deposition, a single plastic sample was placed on top of a silicon wafer and coated with 300 cycles of TMA and water. All samples were coated in three similar consecutive runs, labeled runs I, II, and III, and a new silicon wafer was used in each run. The second sample set was fabricated by applying the Vacseal resin to the rest of the uncoated samples on all sides using an applicator brush, and by curing the resin at 95°C for 24 h. Additionally, the third sample set was made by applying Vacseal to

the underside of some of the ALD coated samples and curing them with the aforementioned procedure. The vacuum and thermal histories of all sample sets were matched by pre-treatments detailed [40]. This was done to ensure that the ALD-coated, resin-coated, and resin- and ALD-coated sample sets had outgassed and dehydrated similarly prior to testing.

4.2.2 Characterization

4.2.2.1 Thickness of deposited film

Thickness measurements were made on monitor wafers using a J. A. Woollam M2000UI ellipsometer. A thickness map was created for each monitor wafer, representing the thickness of alumina deposited on the 3-D printed plastic sample during that ALD run. Changes in the film uniformity are indirect indications of the modification of the outgassing properties or surface morphology of the plastic samples.

4.2.2.2 Microstructure and chemical analysis

To prepare samples for SEM imaging and EDS measurements, the ALD-coated samples were chilled to cryogenic temperatures in a liquid nitrogen bath, and subsequently bent until fracture. The fracture surface provided flat, un-altered views of the ALD coatings and subsurface of the samples.

Both backscatter (BSE) and secondary electron (SE) modes were implemented to image the ALD-coated sample fracture surfaces, and ALD layers. Imaging for the ABS and PC sample interiors (for porosity approximation) was done under a 15 kV accelerating voltage on a Hitachi S-4700 FE-SEM, while the PP sample and ALD layer imaging for all samples was done under 15 kV on a Philips XL40 ESEM.

Porosity fraction was calculated from SEM images processed in ImageJ [48]. The raw SEM images were thresholded to focus on pores in the image, and the surface area of those pores calculated in the program. Porous fractions in PC were determined from images at x10k magnification, whereas ABS porous fraction was approximated at x30k magnification, and PP at x2.5k. The difference in magnification used to calculate porous fraction was due to the difference in size and distribution of pores in each sample; the magnification was chosen to provide the most representative field of view possible.

4.2.2.3 Residual gas analysis for outgassing quantification

A Transpector Inficon residual gas analyzer (RGA) was used on the load lock of a modified Riber molecular beam epitaxy (MBE) system. The characterization chamber was equipped with a bespoke PID controlled nichrome wire heater capable of heating the sample from ambient temperature to 100°C. The sample was elevated using a SS 316 spacer such that the top of the sample was less than 10mm away from the RGA filament. The chamber was pumped down to 10^{-7} Torr using a turbo and a backing mechanical pump. After a 12-hour pump-down, each sample was heated in 10°C increments until the partial pressures of outgassing entities saturated the RGA filament. This partial pressure data was collected using TWare32 gas analysis software. Further, this data was post-processed to normalize

partial pressure of each molecular mass against a baseline collected with an empty chamber using the algorithm detailed [40].

4.3 Results and Discussion

First, the influence of the ABS, PC, and PP samples to the growth of the ALD films was considered. Film thickness maps measured with the ellipsometer for all monitor wafers are presented in **Figure 4.1**. In the case of a bare monitor wafer, the target film thickness was 50 nm per individual run. Based on the maps, it is clear that the presence of the plastic samples had a major impact on the thickness and uniformity of the AlO_x coating. For all samples after each deposition, there was an area of non-uniform growth on the wafer under the plastic samples, likely due to unintentional gas-phase chemical reactions between TMA and water vapor. For ABS samples, the thickness of the deposited film ranged from 18 to 58 nm for each sequential ALD run, and the uniformity of the films did not improve as reported [40]. For PC samples, the films became even less uniform with thickness ranging from 19 to 54 nm after deposition I and 30 to 88 nm after deposition III. In the case of PP samples, the film uniformity improved with each sequential deposition. However, the multicolored areas on the wafers underneath the samples are clear indications that the ALD process had not been optimal in the depositions.

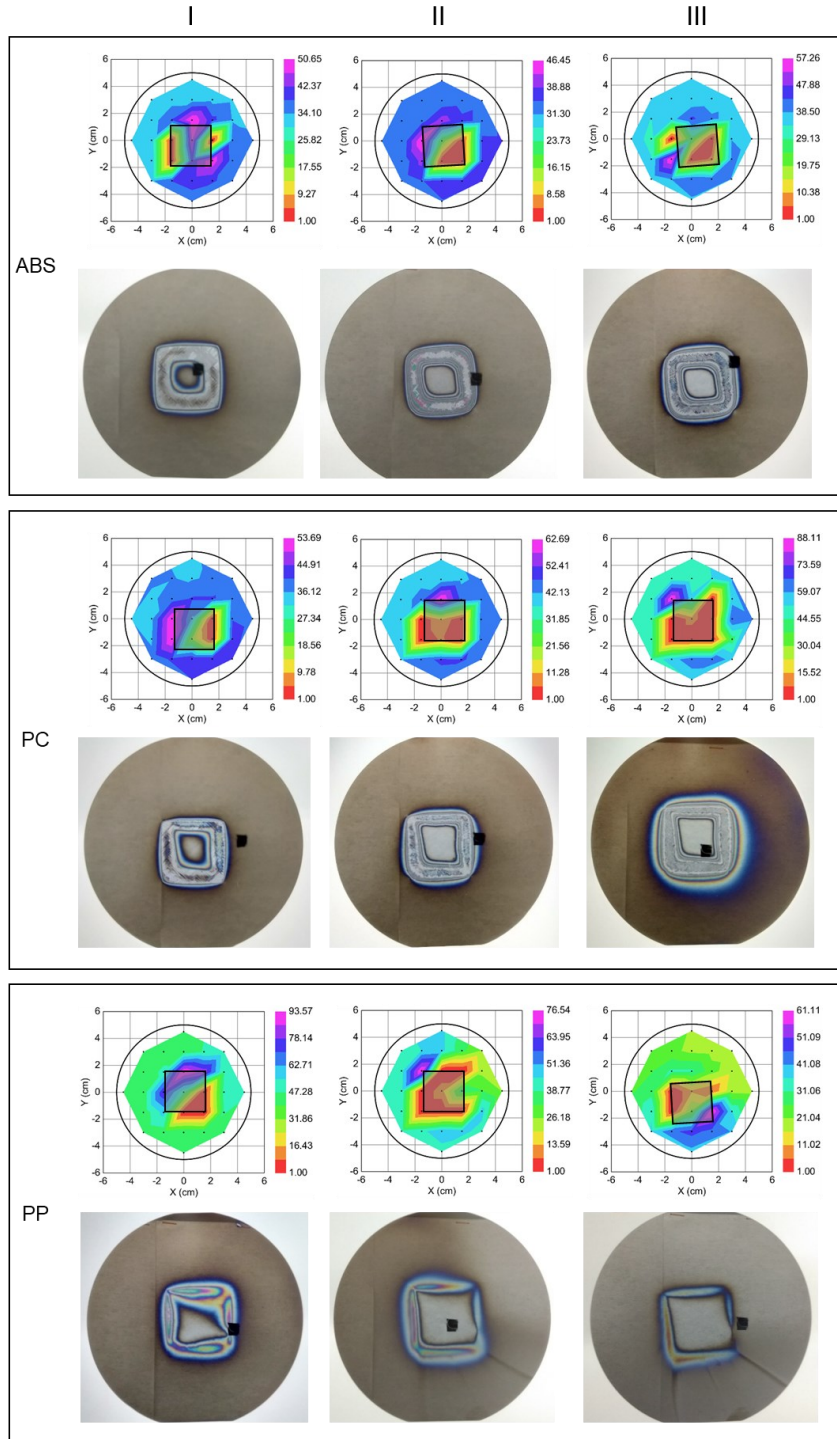


Figure 4.1: Ellipsometry maps showing thickness of AlOx on sequential monitor wafers. The thickness scale (in nm) is represented as a color bar on the right of each map. The square in the middle of each map represents the location of the plastic sample. It is observed that the thickness around the plastic sample is non-uniform due to uncontrolled deposition. The targeted thickness on silicon for each run was 50 nm.

Macroscale porosity was seen in the case of as-printed PC. These evenly spaced pores were attributed to print trajectories [49]. The distance between the pores was measured to be constant at 320 μm while the pores at the widest were 250 μm (**Figure 4.2**). The presence of pores was indicative of insufficient flow of PC during the printing process. While there was no discernible difference in the quality of the PC parts as compared to ABS and PP, it was noted that for vacuum applications, PC should be printed at a slightly elevated temperature to fill up these pores [50-51]. The macropores were not seen post heat-treatment of samples.

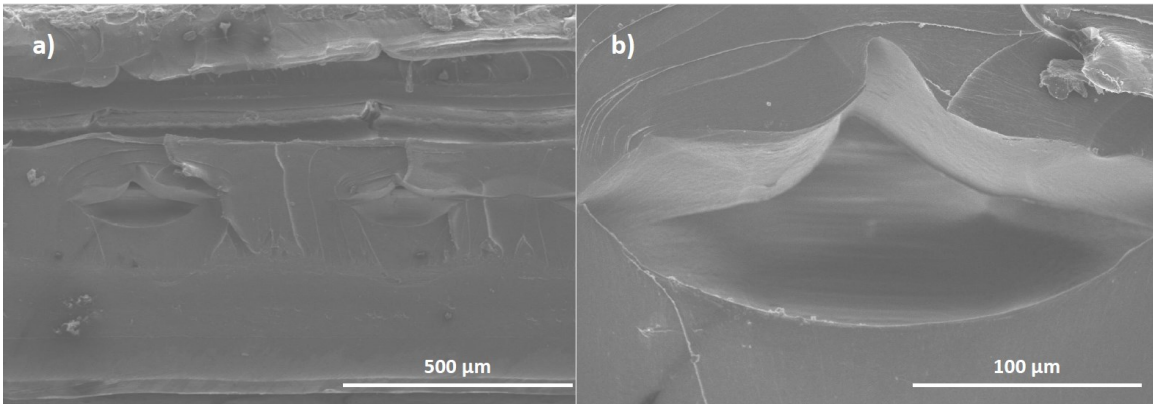


Figure 4.2: SEM image of macropores seen in PC. These are indicative of print lines.

Porous volume fraction (microscale porosity) of the 3-D printed polymer samples was found to be less than 10%, with PC approximated to be 0.1% porous, ABS 8% porous, and PP 2% porous. PC appeared to be devoid of porosity, whereas ABS contained circular pores of various sizes (**Figure 4.3**). The PP sample exhibited a rough fracture surface, but did not exhibit many features that appeared to be pores. It should be noted that surface roughness on the fracture surfaces contributed to artifactual calculation of porosity for the PC and PP samples; however, the porosity determination method was kept consistent between the samples, leading to the calculation of some porosity in these samples. ALD coatings for the samples were observed to be thick and contiguous; an example of the film surface is provided for the PP sample in **Figure 4.3d**.

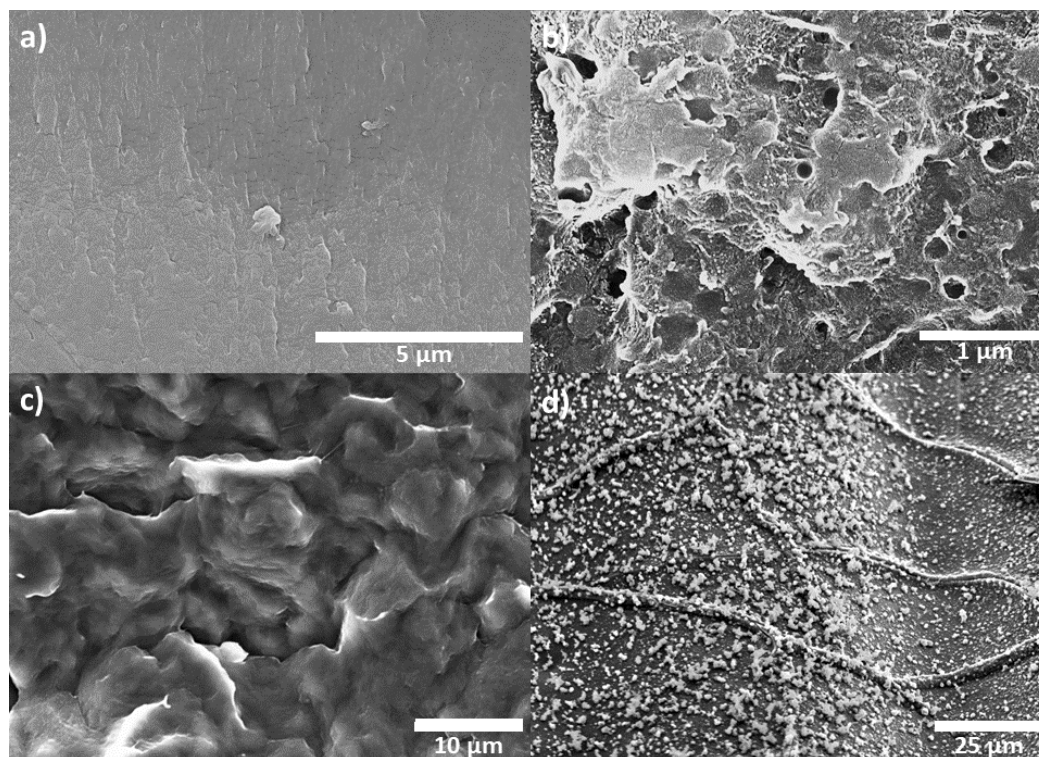


Figure 4.3: SE SEM cross section images of ALD-coated polymer samples: (a) PC (x10k), (b) ABS (x30k), and (c) PP (x2.5k); (d) shows the ALD coating on the surface of the PP sample

Apart from the underlying contiguous film, surface accumulation of AlO_x was seen in all samples. While in the case of PC, AlO_x particles were seen to form long rod-like structures, this behavior was not observed in ABS and PP. Surface particulates on ABS measured under $2 \mu\text{m}$ in length. In the case of PP, 3-D growth was observed with particles appearing to grow vertically in a fractal-like formation (**Figure 4.4**). Each of these particles was observed to be $1\text{-}2 \mu\text{m}$ in size with the entire stack measuring up to $5 \mu\text{m}$. The presence of the surface particulate matter was attributed to the process not bring entirely in the ALD regime, degassing compounds, and high surface roughness of the underlying plastic. It was theorized that some of the TMA molecules may have desorbed from the polymer surface, leading to a reaction between TMA and water vapor taking place in the chamber and not on the surface of the sample. This formation of particulates could also be due to an incomplete purge cycle, which again results in the reaction taking place in the chamber and not on the surface of the sample. Since in a conventional ALD process gas phase reactions are not allowed, the process here was seen to happen at the cusp of the CVD and ALD regimes.

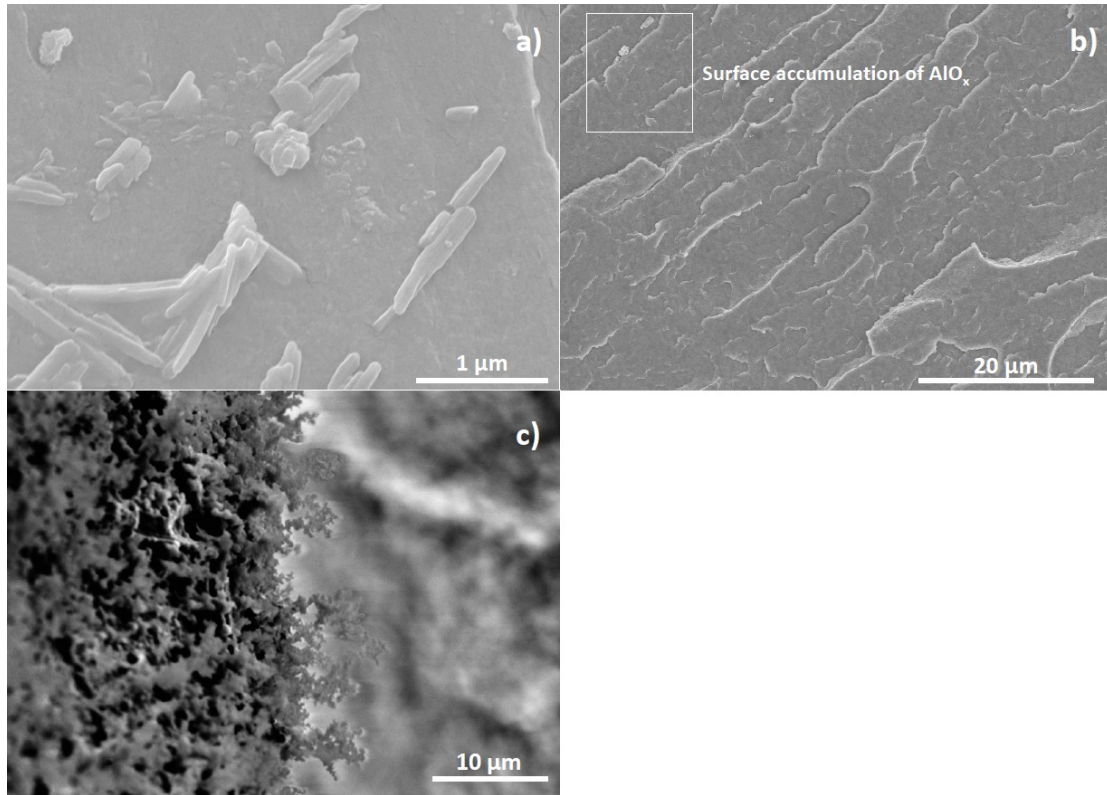


Figure 4.4: Surface accumulation of AlO_x in the form of particles are seen in (a) PC (b) ABS and (c) PP.

The thickness of the ALD-deposited AlO_x layer on plastic was similar between clear PC and ABS, having thicknesses of $2.1 \pm 0.3 \mu\text{m}$ and $2.3 \pm 0.2 \mu\text{m}$, respectively. The PP sample showed a substantially thinner layer, having a thickness of $0.88 \pm 0.5 \mu\text{m}$. The targeted thickness of AlO_x on the monitor wafer was 150 nm. Hence, the much higher apparent thickness on plastic samples speaks to the porosity of samples and the much higher diffusion of TMA and water vapor through the plastic.

It appears that the absence of subsurface porosity results in no subsurface crystallites, such as was observed in the PC and PP samples (**Figure 4.5**). Where subsurface porosity was present, as in the ABS sample, there were crystallites below the polymer sample surface.

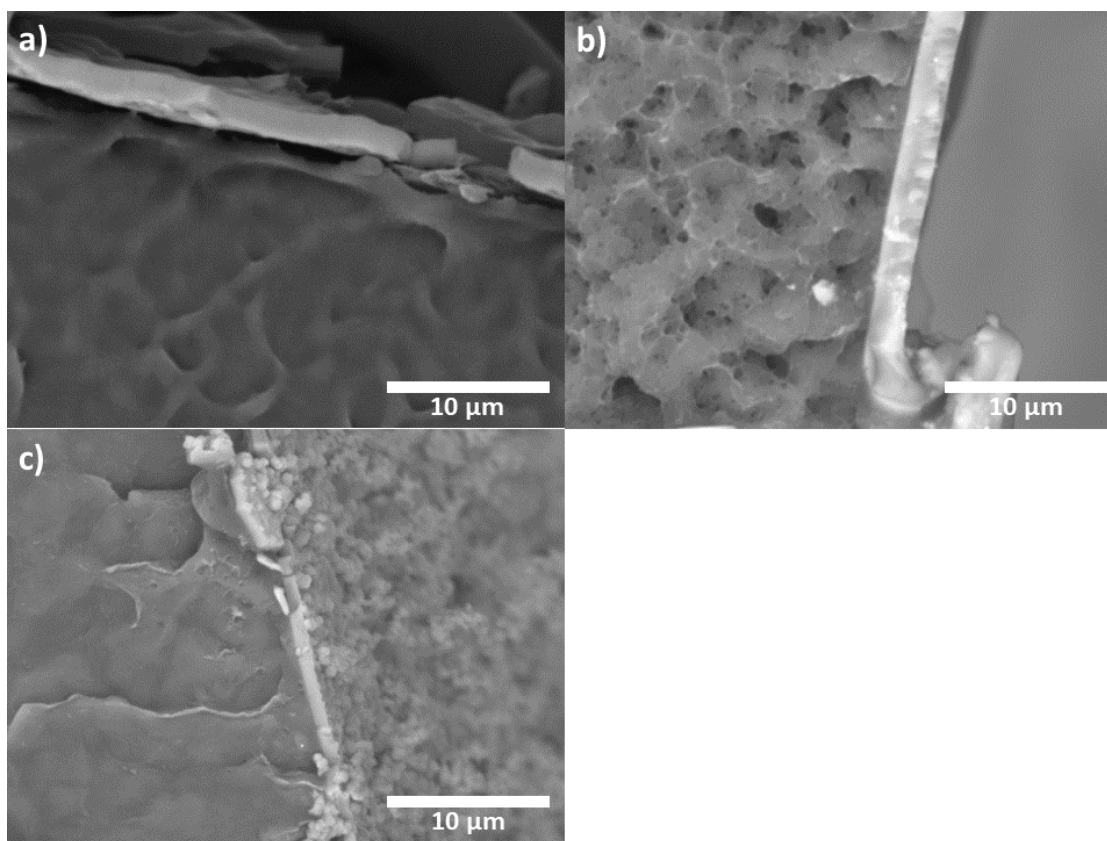


Figure 4.5: BSE SEM cross section images of ALD-coated polymer samples: (a) PC, (b) ABS and (c) PP. Note that all images are at magnification of x3.5k.

To measure the penetration depth of the TMA into the 3-D printed polymer surfaces, EDS line scans measuring Al $K\alpha$ signal were taken on cross sections of the ALD-coated samples perpendicular to the surface (see **Figure 4.5** for field of view for these line scans). It should be noted that differences in porosity, presence of subsurface crystallites, and density of each individual polymer likely impacted the sampling volume and Al $K\alpha$ signal intensity for each of EDS line scans. It should also be noted that the EDS line scan data presented is located with the 0 μm depth at the oxide/polymer interface.

The difference in TMA diffusion depth was found to be both a function of polymer composition, glass transition temperature, porosity, and characteristics of the ALD-forming film. Looking at the Al $K\alpha$ profiles for the clear polymer samples (**Figure 4.6**), clear ABS showed the least penetration, with clear PP having a somewhat higher penetration, and clear PC having a very deep Al $K\alpha$ profile.

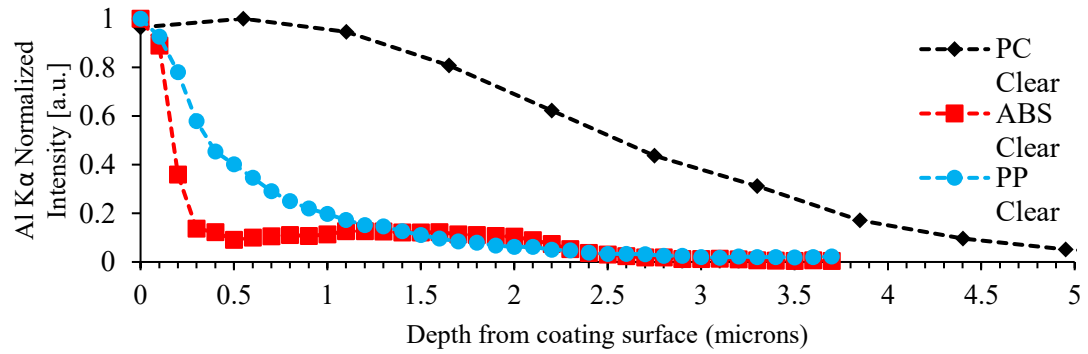


Figure 4.6: EDS depth profiles for Al K α for ALD-coated 3-D printed polymer samples

The sum of normalized partial pressures as a function of temperature for all polymers and atomic masses 1 to 100 is shown in **Figure 4.7**. For all plastics considered, the ALD coated samples registered consistently lower outgassing. Also, it was noted that all ALD coated samples could be successfully heated to 100°C without reaching RGA maximum pressure limits. Additionally, the Vacseal resin coated ABS sample could be heated to 100°C. The trend was that all Vacseal coated samples could only be heated up to 60°C - 70°C. Generally, the outgassing increased with increasing temperature. While in case of ABS the ALD + Vacseal resin coated sample registered higher outgassing than the sample coated with just Vacseal, it is difficult to draw similar conclusions about the PC and PP samples.

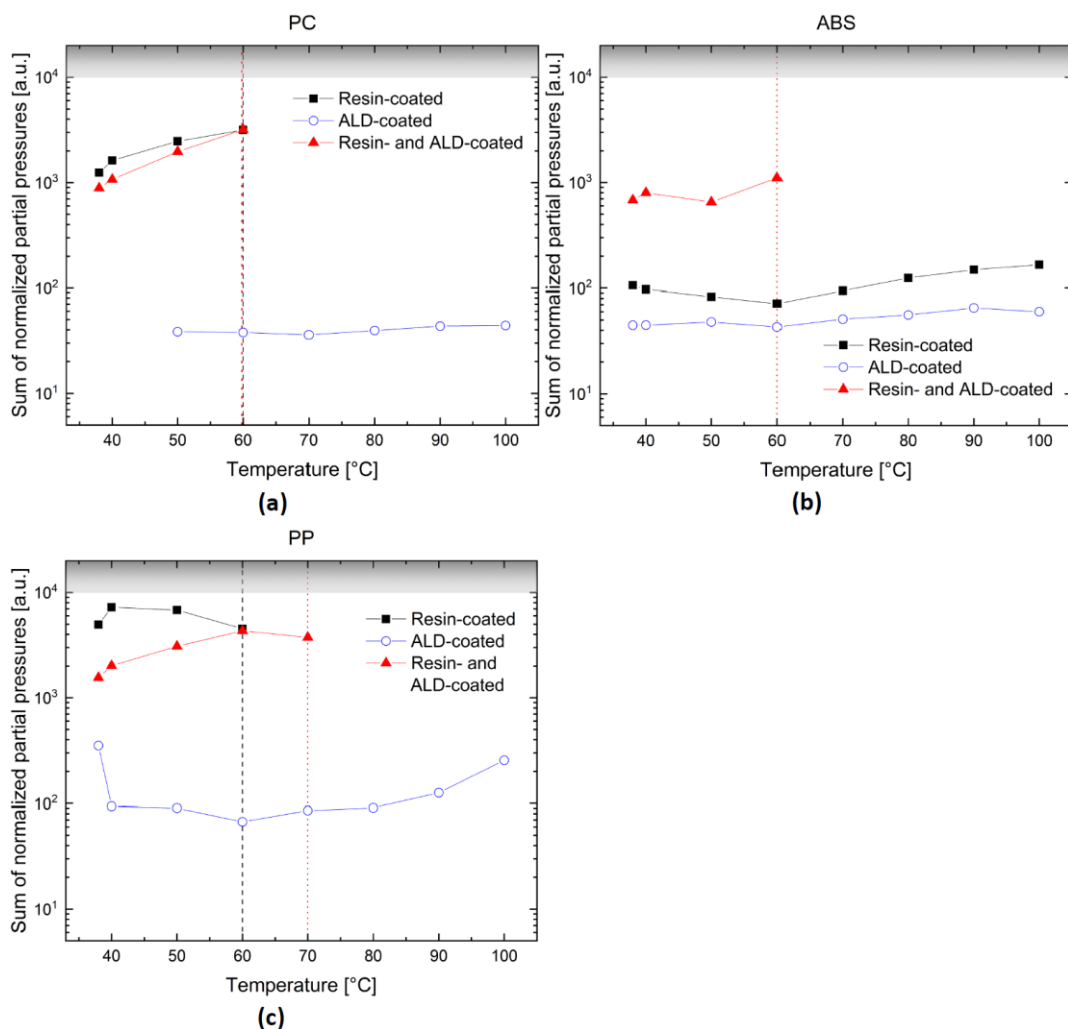


Figure 4.7: Sum of normalized partial pressures at all measured temperatures for (a) PC, (b) ABS, (c) PP. The vertical dashed lines indicate temperature setpoints after which partial pressure could not be measured without damaging equipment. The grey area represents a region of high outgassing where data collection is not possible with the RGA used in this study.

All sample data, ALD coated, resin-coated, and resin- and ALD-coated, could be gathered for temperatures up to 60°C. After 60°C some of these samples registered high degrees of outgassing and the RGA could not be safely operated. Hence all comparison is done at 60°C.

Compared to ALD-coated samples, the resin-coated samples registered higher outgassing. This is due to incomplete curing of the resin [40]. The application of Vacseal to the samples is a manual process using the brush provided by the manufacturer. Often a layer that is too thick may be deposited. When this layer is cured at room temperature it can take several weeks [52]. The high outgassing seen from the Vacseal coated sample is attributed to the solvents present in Vacseal. The peak at 91 AMU was matched to xylene, ethylbenzene

and toluene – the main components of Vacséal [53-54]. Without an effective curing method, Vacséal is not recommended as a sealant for plastics used in vacuum applications. Effective curing of Vacséal happens at elevated temperatures, which most polymeric materials cannot tolerate.

The partial pressures of outgassed entities from ALD coated samples were consistently lower for all materials, making an ALD coating, despite its non-uniformity, the best choice to inoculate polymers against outgassing. It should be noted that no data could be collected for uncoated polymers because their outgassing was too great for the equipment used and the Vacséal coating reduced outgassing enough to enable sample pump down to 10^{-7} Torr.

The outgassing characteristics of ALD coated PC, ABS and PP were very similar, with PC and ABS registering sharp drops at certain atomic numbers. In comparison, the outgassing seen in case of ALD coated PP was more stable.

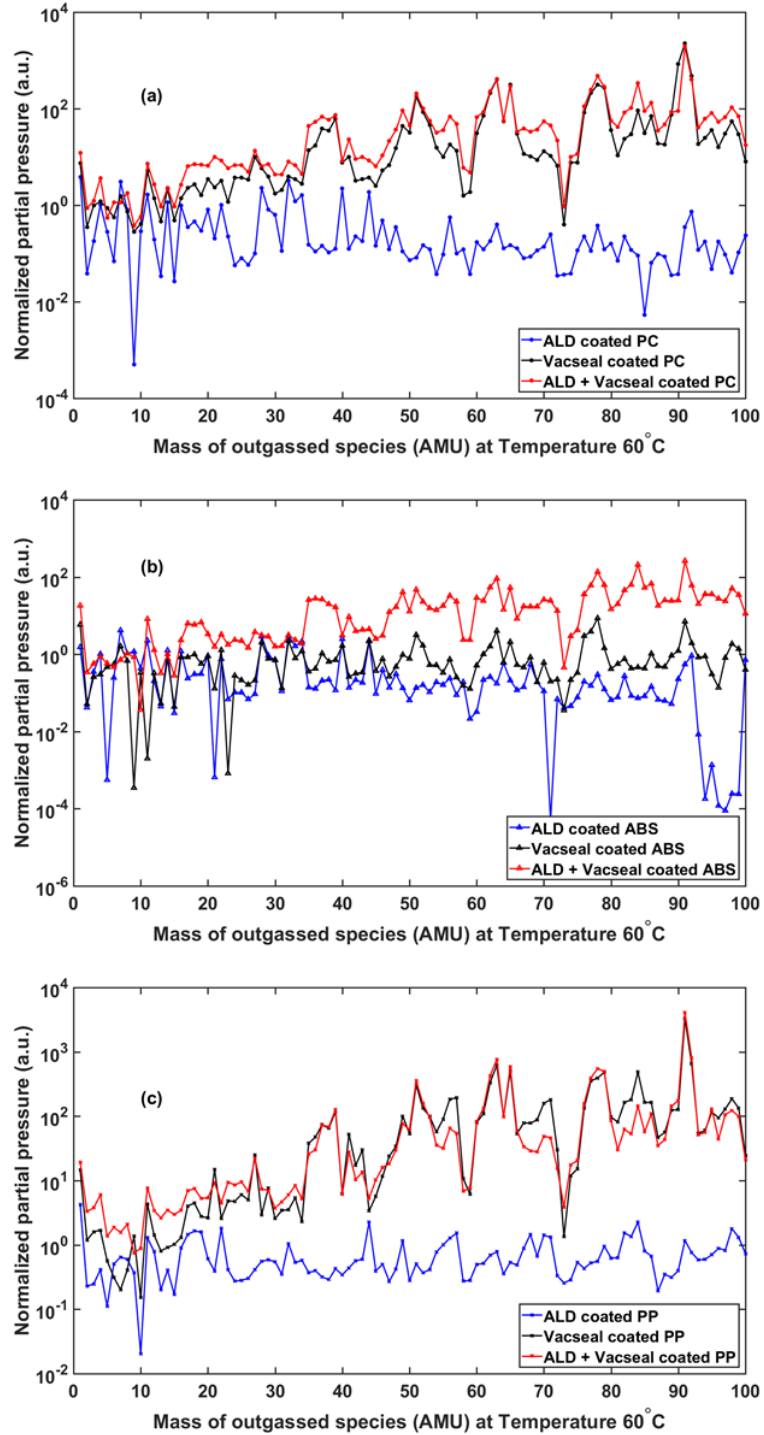


Figure 4.8: Outgassing characteristics of clear PC (a), ABS (b) and PP (c) at molecular masses 1 to 100 at 60°. A consistently low value of normalized partial pressure was seen for all ALD coated samples.

The porosity of the 3-D printed materials can make the use of ABS, PC, and PP challenging for vacuum applications, as increased surface area and relatively large pores have the potential to trap atmospheric gases into the materials. Especially in the case of PC, the extent of macroscale porosity can likely be reduced by increasing the flow rate of the filament, using a higher nozzle temperature, and optimizing the print speed in the printing process. Similar optimization can yield a smaller extent of pores and surface roughness for ABS and PP, as well. Another factor that can influence the formation of pores during the printing is the moisture content of the plastics, which can be reduced by pre-baking the filaments at an elevated temperature prior to the printing, and enclosing the filaments in a desiccant chamber during the printing process. Additionally, the surfaces of 3-D printed components intended for vacuum applications can possibly be smoothed by mechanical polishing or solvent vapor treatments prior to coating them with ALD materials or resins.

The ALD process employed in these studies was not optimal for the highly porous 3-D printed plastics. Longer purge steps between the precursor pulses are expected to yield more uniform film coverage on the 3-D printed plastics samples. This, in turn, could improve the outgassing characteristics of the plastics even further, as pinhole-free ALD AlO_x films are efficient gas barriers [28-29]. The length of the precursor pulses could as well be tuned to ensure sufficient coverage of the plastic surface with the AlO_x film. In addition, the plastic sample could be heat treated before the ALD deposition to minimize outgassing in the reactor chamber and allow a more uniform, higher quality deposition.

While most ALD films observed were continuous, there were certain defects observed, such as, the break in the coating seen in **Figure 4.5(a)**. Despite these defects the coatings were deemed to be effective outgassing barriers at the measured pressures. In order to reduce outgassing further, which may be necessary for certain contamination-sensitive applications [55-59], it would be useful to characterize the outgassed species, its effect on the tooling and other samples processed either in the same or subsequent runs. Further research is also recommended to study the mechanism behind outgassing reduction when ALD films are used as barrier coatings. In addition, 3-D printing parameters have an impact on porosity and surface finish, which in turn affect how contiguous the barrier coating will be. Several other factors, such as, a specific polymer's affinity towards a certain precursor molecule needs to be studied too [47,60]. The main limitation of the outgassing data shown in this study is that it was collected after 12 hours of pump down, when the system was under very high vacuum. It is reported that some species, such as water vapor, selectively outgas in the mTorr pressure range [61-62]. Hence, a kinetic study of partial pressure measurement, while the system is pumping down is recommended.

When these 3-D printed plastics are sealed effectively, they could be used in vacuum environments as substrates, replacement parts and as whole systems.

4.4 Conclusions

Unpigmented 3-D printed PC, ABS and PP were coated with two types of barrier coatings, an ALD AlO_x layer and a commercially available resin Vaseal, in order to study their vacuum compatibility. The low levels of porosity seen in these polymers coupled with the

absence of a potentially volatile pigment made them suitable candidates to be tested for outgassing in a vacuum environment. In both cases, a reduction in outgassing was observed as compared to uncoated films under a very high vacuum. Further, the ALD coated samples registered lower pressures than the resin coated ones, showing an ALD film to be effective at inoculating plastics in a vacuum environment.

4.5 Acknowledgements

This work was partially supported by Fulbright Finland, the Witte endowment and Aleph Objects. The authors acknowledge the provision of facilities by Aalto University at OtaNano – Micronova Nanofabrication Centre and at the RawMatTERS (RAMI) facilities, and the Applied Chemical and Morphological Analysis Laboratory at Michigan Tech for use of the instruments and staff assistance. I.T.S.H. acknowledges the financial support from AaltoELEC Doctoral School and Walter Ahlström foundation. G.M. and M.K. gratefully acknowledge funding from the Strategic Research Council at the Academy of Finland (CloseLoopConsortium, Grant No. 303452).

4.6 References

- [1] K. Wong and A. Hernandez, *ISRN Mechanical Engineering* 2012, (2012).
- [2] D. Schniederjans, *International Journal of Production Economics* 183, (2017).
- [3] N. Guo and M. Leu, *Frontiers of Mechanical Engineering* 8, (2013).
- [4] B. Wittbrodt, A. Glover, J. Laureto, G. Anzalone, D. Oppliger, J. Irwin and J. Pearce, *Mechatronics* 23, (2013).
- [5] A. Laplume, B. Petersen and J. Pearce, *Journal of International Business Studies* 47, (2016).
- [6] J. Pearce, *Science* 337, (2012).
- [7] J. Pearce, *Open-source lab: how to build your own hardware and reduce research costs*, (2013).
- [8] T. Baden, A. Chagas, G. Gage, T. Marzullo, L. Prieto-Godino and T. Euler, *PLOS Biology* 13, (2015).
- [9] M. Coakley and D. Hurt, *Journal Of Laboratory Automation* 21, (2016).
- [10] I. Petrick and T. Simpson, *Research-Technology Management* 56, (2013).
- [11] B. Berman, *Business Horizons* 55, (2012).
- [12] D. Bak, *Assembly Automation* 23, (2003).
- [13] J. Pearce, *Science and Public Policy* 43, (2015).

- [14] T. Pasanen, G. von Gastrow, I. Heikkinen, V. Vähänissi, H. Savin and J. Pearce, *Materials Science in Semiconductor Processing* 89, (2019).
- [15] I. Hietanen, I. Heikkinen, H. Savin and J. Pearce, *Hardwarex* 4, (2018).
- [16] J. Dever, S. Miller, E. Sechkar and T. Wittberg, *High Performance Polymers* 20, (2008).
- [17] Hall, D. and Fote, A., *26th Thermophysics Conference*, (1991).
- [18] J. Townsend, P. Hansen, J. Dever, K. de Groh, B. Banks, L. Wang and C. He, *High Performance Polymers* 11, (1999).
- [19] T. Zuby, K. Degroh and D. Smith, *Degradation of FEP Thermal Control Materials Returned From The Hubble Space Telescope (No. N--96-18436; NASA-TM--104627; NAS--1.15: 104627; REPT--96B00024; NIPS--96-07908)*. (National Aeronautics and Space Administration, Greenbelt, MD (United States). Goddard Space Flight Center., 1995).
- [20] J. Dever, K. de Groh, B. Banks and J. Townsend, *High Performance Polymers* 11, (1999).
- [21] W. Campbell Jr, R. Marriott and J. Park, *Outgassing Data for Selecting Spacecraft Materials* (National Aeronautics and Space Administration, 1984).
- [22] J. Gaier, M. Brinkmeier and E. Gaier, in (NASA CONFERENCE PUBLICATION, 2020), pp. 257-268.
- [23] R. Elsey, *Vacuum* 25, (1975), pp. 299-306.
- [24] J. Kwon, H. Jung, I. Yeo and T. Song, *Vacuum* 85, (2011).
- [25] R. Elsey, *Vacuum* 25, (1975), pp. 347-361.
- [26] W. Perkins, *Journal of Vacuum Science and Technology* 10, (1973).
- [27] A.J. Muller, L.A. Psota-Kelty, H.W. Krautter and J.D. Sinclair, *Solid State Technology* 37, (1994).
- [28] T. Hirvikorpi, M. Vähä-Nissi, A. Harlin, J. Marles, V. Miikkulainen and M. Karppinen, *Applied Surface Science* 257, (2010).
- [29] T. Hirvikorpi, M. Vähä-Nissi, A. Harlin and M. Karppinen, *Thin Solid Films* 518, (2010).
- [30] J. Lange and Y. Wyser, *Packaging Technology and Science* 16, (2003).
- [31] H. Chatham, *Surface And Coatings Technology* 78, (1996).

- [32] S. Park, J. Oh, C. Hwang, J. Lee, Y. Yang and H. Chu, *Electrochemical and Solid-State Letters* 8, (2005).
- [33] A. Ghosh, L. Gerenser, C. Jarman and J. Fornalik, *Applied Physics Letters* 86, (2005).
- [34] J. Meyer, D. Schneidenbach, T. Winkler, S. Hamwi, T. Weimann, P. Hinze, S. Ammermann, H. Johannes, T. Riedl and W. Kowalsky, *Applied Physics Letters* 94, (2009).
- [35] T. Minton, B. Wu, J. Zhang, N. Lindholm, A. Abdulagatov, J. O’Patchen, S. George and M. Groner, *ACS Applied Materials & Interfaces* 2, (2010).
- [36] G. Pluvinage, Springer Science & Business Media, (2003).
- [37] E. Kelly, *The Journal Of Prosthetic Dentistry* 21, (1969).
- [38] D. Rickerby and N. MacMillan, *Wear* 60, (1980).
- [39] Vacseal.Net (2020).
- [40] I. Heikkinen, G. Marin, N. Bihari, C. Ekstrum, P. Mayville, Y. Fei, Y. Hu, M. Karppinen, H. Savin and J. Pearce, *Surface and Coatings Technology* 386, (2020).
- [41] B. Puri and R. Bansal, *Carbon* 1, (1964).
- [42] N. Tanikella, B. Wittbrodt and J. Pearce, *Additive Manufacturing* 15, (2017).
- [43] A. Davis and J. Golden, *Journal Of Macromolecular Science, Part C* 3, (1969).
- [44] J. Cantrell, S. Rohde, D. Damiani, R. Gurnani, L. DiSandro, J. Anton, A. Young, A. Jerez, D. Steinbach, C. Kroese and P. Ifju, *Rapid Prototyping Journal* 23, (2017).
- [45] W. Zhu, S. Pyo, P. Wang, S. You, C. Yu, J. Alido, J. Liu, Y. Leong and S. Chen, *ACS Applied Materials & Interfaces* 10, (2018).
- [46] I. Heikkinen, C. Kauppinen, Z. Liu, S. Asikainen, S. Spoljaric, J. Seppälä, H. Savin and J. Pearce, *Additive Manufacturing* 23, (2018).
- [47] Outgassing.Nasa.Gov (2020).
- [48] Imagej.Nih.Gov (2020).
- [49] S. Guessasma, S. Belhabib and H. Nouri, *Polymers* 11, (2019).
- [50] Y. Song, Y. Li, W. Song, K. Yee, K. Lee and V. Tagarielli, *Materials & Design* 123, (2017).

- [51] I. Gajdoš and J. Slota, Tehnički Vjesnik 20, (2013).
- [52] Application Notes on Vacseal, 2Spi.Com (2020).
- [53] Vacseal SDS, Vacseal.Net (2020).
- [54] Webbook.Nist.Gov (2020).
- [55] T. Patrick, Vacuum 23, (1973).
- [56] K. Fayazbakhsh and A. Abedian, Advances In Space Research 45, (2010).
- [57] A. Neuber, M. Butcher, H. Krompholz, L. Hatfield and M. Kristiansen, IEEE Transactions On Plasma Science 28, (2000).
- [58] N. Ridley and Z. Wang, Materials Science Forum 233-234, (1996).
- [59] D. Storm, T. McConkie, M. Hardy, D. Katzer, N. Nepal, D. Meyer and D. Smith, Journal Of Vacuum Science & Technology B, Nanotechnology And Microelectronics: Materials, Processing, Measurement, And Phenomena 35, (2017).
- [60] M. Sefa, Z. Ahmed, J. Fedchak, J. Scherschligt and N. Klimov, Journal Of Vacuum Science & Technology A: Vacuum, Surfaces, And Films 34, (2016).
- [61] R. Grinham and A. Chew, Applied Science And Convergence Technology 26, (2017).
- [62] G.P. Beukema, Cursus Vacuumtechnologie (2016).

5 Understanding the multilevel phenomena that enables inorganic atomic layer deposition to provide barrier coatings for highly-porous 3-D printed plastic in ultra-high vacuums

When 3-D printed plastic is exposed to vacuum, the low molecular mass entities outgas, leaving behind a weakened polymer matrix and potentially contaminating the vacuum equipment. Inorganic barrier coatings can limit this diffusion and offers potential for bespoke plastic vacuum equipment. Atomic layer deposition (ALD)-coated plastic parts have been shown to be compatible with vacuum conditions, but the failure mechanisms under vacuum are not well understood. The diffusion of precursor materials into porous plastic to deposit thin diffusion barriers is a multi-scale phenomenon, and the surface properties of the plastic interface must be correlated with its bulk properties for a complete understanding these barriers. This investigation makes a comparative study of ALD deposited alumina on 3-D printed black and clear acrylonitrile butadiene styrene, polycarbonate and compares surface properties of commercially available polypropylene with pure polypropylene. The results show that despite surface defects of 3-D printed plastics, ALD deposited alumina adequately remedies outgassing at very high vacuum levels and indicate that moisture affinity of the matrix polymer may impact penetration depths of trimethylaluminum. It is concluded that the thickness of an ALD-based barrier inorganic coating on porous 3-D printed plastic is a complex function of its functional groups, porosity and crystallinity.

5.1 Introduction

Polymers have found applications in a multitude of microelectronics manufacturing related fields such as barrier coatings [1-4], encapsulation [5-9], photoresists [10,11], self assembled monolayers (SAMs) [12-16], precursors and catalysts for atomic layer deposition (ALD) and chemical vapor deposition (CVD) processes [17-20]. While these polymers are being integrated into clean processes, there is a conspicuous absence of polymeric materials in the equipment used to build systems capable of running these processes. Outside of the cleanroom, scientists have benefited from the application of digital additive manufacturing of a rapidly expanding list of open source designs to make low-cost custom scientific equipment [21-23]. Such highly customized 3-D printed scientific components have already been shown to be compatible with clean room environments [24], but for the most strategic national scientific goals high-value vacuum processing is needed [25]. These highly customized systems could potentially be fabricated using additive manufacturing of various plastics and used in vacuum processing with appropriate inorganic coatings.

To use these 3-D printed parts from low-cost and accessible polymer-based printers to build laboratory equipment making use of vacuum conditions, it is essential to understand failure mechanisms of these materials. One of the primary reasons plastic parts fail when exposed to a vacuum environment is because low molecular mass molecules escape the polymer matrix in a process called outgassing, leading to organic contamination in a formerly clean chamber [26-31]. This also leads to the mechanical integrity of the part getting compromised [32-37].

In order to prevent the plastic part from outgassing a number of barrier coatings have been proposed [38-40]. The inorganic coatings grown using atomic layer deposition (ALD) show the most promise due to the conformal nature of the process. A simple ALD process alternates precursors flowing into the deposition chamber. The first precursor flows in the chamber during the pulse time and reacts with the active group on the surface until complete surface coverage is obtained. During a purge step, all the excess precursor and by-products are removed from the chamber before the second precursor flows into the chamber. After this pulse, the surface reactions for the desired material and the ALD cycle is completed with another purge step. The number of repetitions of the ALD cycle will determine the thickness of the thin film, while pulse and purge steps need to be optimized based on the complexity of the structure to be coated. The gas phase nature and the step by step process of ALD are the basis of the conformability of the deposited film [41,42]. Since ALD relies on self-saturating chemical reactions between the precursors and the substrate, high aspect ratio structures can be easily coated [43-47]. These high aspect ratio features are seen in 3-D printed parts not just as the print lines, but also as holes due to the porous nature of the plastic, which can even be impacted by the color [48]. In a low temperature ALD process on a porous substrate, there is a high level of penetration of the coating. This implies that for the same mass flow, a targeted thickness of 150 nm (on a polished silicon surface) may not translate to 150 nm on a plastic substrate [49]. This thickness may be highly non-uniform and vary from the nanometer to the micrometer range [49]. Hence, to characterize these films, there is a need to apply a mesoscopic method. This study provides a multilevel approach comprising various characterization methods to probe the interaction of the deposited inorganic film on the substrate at the nanoscale as well as the micron level.

To study these multi-scale properties, ALD alumina coated 3-D printed plastics were investigated; one sample set pigmented with black color and the other was unpigmented. Polycarbonate (PC) and acrylonitrile butadiene styrene (ABS) were chosen as materials of interest; PC because of its strength and high temperature resistance [50-51] and ABS because it is one of the most commonly used 3-D printing plastics [52]. In addition, polypropylene (PP) was added to the unpigmented sample set because of its high inertness, which makes it appropriate for chemical processing [53]. These characterization techniques were specifically chosen because of their sensitivity at varying length scales. The bulk crystallinity of the plastic was examined through x-ray diffraction (XRD), microstructure through energy dispersive x-ray spectroscopy (EDX), and the surface through x-ray photoelectron spectroscopy (XPS) and Fourier transform infrared spectroscopy –

attenuated total reflectance (FTIR-ATR). In addition, the outgassing was quantified using a bespoke vacuum chamber set up equipped with a residual gas analyzer (RGA) [54]. The results were analyzed to provide a comparison of how surface properties and penetration of alumina differ with the addition of a pigment to plastic. The results are discussed in the context of the use of 3-D printed plastic as components for vacuum systems.

5.2 Experimental

Individual samples of PC and ABS dimensions 30 x 30 x 1 mm were 3-D printed using a Lulzbot Taz 6 RepRap-class 3-D printer (Aleph Objects, USA) using printing parameters described in detail earlier [49, 54]. To print pure PP for contaminant analysis, PP pellets were acquired from Millipore Sigma (Saint Louis, MO, USA). A RepRap-class delta 3-D printer [55] was modified to print these soft pelletized samples using a heated steel syringe following the designs for open source wax pellet printers [56]. Open source Franklin software [57] was used to control the system and print 30 x 30 x 1 mm samples.

These samples were then coated with ALD alumina with a process pressure of 20mTorr in a top-flow type reactor (Picosun R-100) using a protocol presented in earlier studies [48,54]. The films were deposited at 80°C utilizing trimethylaluminium (TMA) and water as precursors. The precursors were kept at room temperature in the containers and reached the deposition chamber carried by a constant flow of nitrogen. The pulse time of the TMA and water were 0.2 and 0.5 s respectively with a 5 s purge time between both pulses.

The target thickness of AlO_x on the plastic substrates was 150 nm and to achieve that 3 depositions of 300 ALD cycles were performed on each plastic substrate. The target thickness was the one measured for 900 ALD cycles on a silicon sample. The total of 900 cycles was divided into 3 separate depositions because the carrier wafer under the plastic substrate could be changed every deposition to study the effect of the plastic sample on the deposited thickness. These depositions were marked I, II and III per each plastic sample, and the samples were characterized after all three deposition runs.

5.2.1 Characterization

5.2.1.1 *Thickness of deposited film*

Monitor wafers were used to measure the thickness of alumina using a J. A. Woollam M2000UI ellipsometer. The generated thickness maps served as indirect indicators of thickness non-uniformity on the plastic substrates.

5.2.1.2 Residual gas analysis for outgassing quantification

The load lock of a Riber molecular beam epitaxy system was modified to serve as an outgassing test chamber. A Transpector Inficon residual gas analyzer (RGA) was installed on an available flange. A PID controlled heater was built and installed to serve as the substrate heater. A SS 316 spacer was used to elevate the sample such that the top of the sample was within a 10mm distance from the RGA filament. The system was attached to a roughing and a turbo pump and a 12-hour pump down sequence was initiated. This resulted in a base pressure of $\sim 10^{-7}$ Torr. After the base pressure was reached, the RGA data was collected using TWare32 gas analysis software at ambient temperature and at elevated temperatures in steps of 10°C. This data was normalized against a baseline collected in an empty chamber [54].

5.2.1.3 Microstructure analysis

Cryo-fractured samples were coated with Pt-Pd and the surface was examined under a Philips XL-40 ESEM at 15kV. Energy-dispersive X-ray spectroscopy (EDS) data was collected to quantify the penetration of alumina into the porous substrate. Open source ImageJ (NIH) was used to calculate porosity.

5.2.1.4 FTIR

A Nicolet iS50R Fourier transform infrared spectrometer (FTIR, Thermo Fisher Scientific) was used to collect attenuated total reflectance FTIR (ATR-FTIR) spectra of all tested polymer samples. Samples of clear and black PC and ABS were analyzed using ATR-FTIR. In addition, commercially available PP filament and pure PP (Sigma-Aldrich, MO) were compared. An ATR diamond cell and an La-DGTS detector was used to collect spectra between 4000 – 400 cm^{-1} range. All ATR-FTIR spectra were collected using 256 scans, a 4 cm^{-1} spectral resolution and a gain of 4.0. The absorption peaks were compared with the literature data in order to compare differences between the polymers and assign key vibrational modes.

5.2.1.5 Crystallinity calculation using XRD

In order to quantify the crystallinity of each sample, a Scintag XDS-2000 θ/θ powder diffractometer (CA, USA) was used with a 2000W Cu X-ray tube ($\lambda=1.540562\text{\AA}$). 2θ data was gathered for angles between 5° and 90° in steps of 0.04° using the software package Scintag DMSNT.

5.2.1.6 Surface analysis using XPS

A PHI 5800 X-ray photoelectron spectrometer (Physical Electronics; Chanhassen, MN) was used with a Mg anode operated at 15kV to produce electron energy of 1253.6 eV. Survey spectra were collected for all coated ABS and PC samples, and uncoated pure PP and filament PP samples. These were collected in intervals of 0.8 eV/step, 20 ms/step dwell time and a 187.85 eV pass energy. High resolution spectra were collected in intervals of 0.1 eV/step, 100 ms/step dwell time and a 23.50 eV pass energy. The number of scans collected were 30 scans for N 1s and 10 scans for O 1s, C 1s and Si 2p.

5.3 Results and discussion

To understand how the ALD films are deposited on the plastic and how the 3-D printed samples affect the deposition, the carrier wafers that were carrying the sample in the deposition chamber were analyzed. A thickness map over the wafer area (100 mm diameter) was performed by ellipsometry [48,54]. The expected thickness of 50 nm was not observed on the silicon, showing that the presence of the plastic samples was affecting the film growth. An effect on the gas flow was observed with higher thicknesses observed on areas of the wafers near the precursor's inlets. The higher thicknesses near the inlets are thought to be caused mostly by the precursors accumulating inside the porous surface of the plastic samples. During the subsequent pulse, the trapped precursor would release and react with the incoming precursor both in the gas phase and on the wafer surface. This situation could be improved with a longer purge step that would be more effective at removing all the unreacted precursor from the voids in the surface. The presence of the trapped precursors explains the higher thickness near the precursor's inlets and the lower thickness near the inlets where just carrier gas flowing. Subsequent depositions on the same sample show a slight reduction in this effect and a reduction in penetration of the precursors inside the surface because the previously deposited alumina film starts acting as the barrier. In addition, the reduced degassing will cause less disturbance to the gas flow. In the future, a more optimized recipe for the deposition will include longer purge times (and pulse if needed), higher number of cycles to further improve the barrier properties. The tuning of the recipes to the different plastic materials would further improve the reduction of the degassing.

Based on SEM imaging data, high degree of porosity was observed in the black samples, but not in the clear ones. This was attributed to the presence of carbon black in the black samples. Carbon black is a highly adsorbent material that has an affinity towards volatile organic compounds (VOCs) commonly seen in these plastic materials [58]. Since subsurface crystallites were seen in all the samples [48,54], cross sectional EDS was used to determine the extent of alumina penetration (Figure 5.1).

For the black polymer Al K α profiles, opposite behavior relative to the clear samples was seen for PC and ABS: black PC had a much shallower penetration depth, whereas black ABS appeared to have had deeper penetration of TMA.

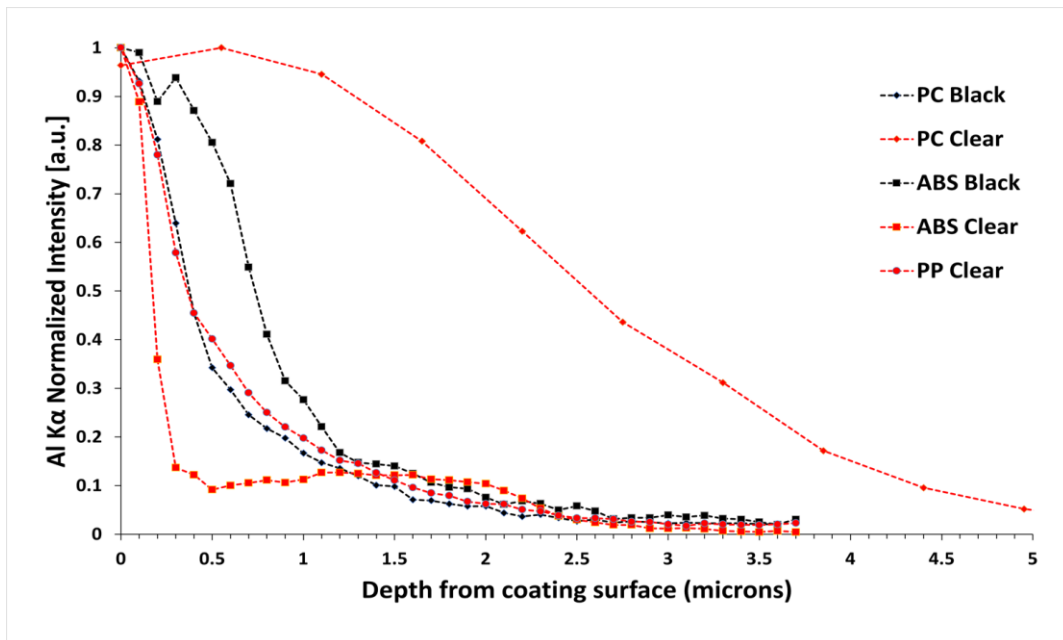


Figure 5.1: EDS depth profiles for Al K α for clear and black ALD-coated 3-D printed polymer samples. 0 μm represents the alumina oxide/polymer interface.

The diffusion of gas through a polymer is dependent on multiple characteristics of both the gas and polymer: gas solubility, diffusivity, and reactivity in the polymer, as well as polymer free volume, porosity, crystallinity, and functionality [59-62]. While there are many competing factors at play in this study, polymer functionality and glass transition temperature within the clear polymer samples appear to be significant to TMA penetration depth.

The high TMA penetration depth for clear PC can be explained by the presence of the carbonyl groups in the polymer, which have been found to strongly associate, and react, with TMA; this has been found to promote micron-scale penetration and formation of AlO $_x$ in the subsurface of PC [63]. Despite a lack of functionality that is known to strongly associate with TMA, clear PP was found to have a TMA penetration depth of over a micron. This can potentially be explained by the ALD deposition temperature being greater than PP's T_g by approximately 100°C. It has been previously observed that glass transition temperature is an important factor in TMA penetration of chemically inert polymers, with higher mass uptakes upon exposure to TMA when ALD reactor temperatures exceed the T_g of the substrate polymer. Limited mass-uptake under TMA exposure has been reported for those polymers that react with TMA, such as PET and PMMA, due to the formation of

a saturated reaction layer at the polymer surface [64]. It is possible that a similar phenomenon occurs due to oxide layer formation in the case of clear ABS, with oxide formation early in the deposition process isolating TMA from the polymer, thus resulting in a shallow penetration depth.

It was observed that the clear PP sample had a thinner ALD-deposited film than PC and ABS samples. Slower nucleation of AlO_x film via the TMA/ H_2O ALD system on chemically-inert polymers, such as PP, has been previously reported [63]. The mechanism explaining this behaviour is the weaker association of TMA with bonding sites at the polymer's surface. That there is a thick ALD film on the clear ABS sample suggests that the ABS surface interaction with TMA is reactive enough to quickly nucleate an ALD film. As noted before, the strong association between the carbonyl groups in PC and TMA allows for quick film nucleation and growth.

It is interesting to note that both clear PC and ABS had significantly different Al $K\alpha$ profiles, yet they have similar film thicknesses. This is possibly due to a difference in diffusivity of TMA in the polymers, the presence of pores in the clear ABS sample, and the difference in moisture content in the polymer subsurface. Sub-surface crystallites present in the clear ABS sample, indicating that some portion of the TMA diffused into the polymer reacted towards the surface of the sample, the pores acting as TMA-sinks; such behaviour would lessen the concentration gradient into the polymer surface, and reduce the subsurface diffusion flux. Additionally, ABS is known to have a high moisture adsorption percentage [65], which might promote a TMA reaction near the surface of the polymer. The ALD-coated samples in this study were coated without any pre-treatment, so some amount of atmospheric moisture would have still been present in the polymers.

The presence of porosity in the polymer subsurface appears to cause the formation of AlO_x crystallites within pores. As subsurface crystallites were only observed in black and clear samples that contained at least ~8% porosity (Figure 5.2), the presence of pores appear necessary for subsurface oxide formation at the ALD parameters implemented in this study. The presence of porosity in the underlying polymer also appears to impact the thickness of the ALD coating, with transport of TMA into interior surface area and being consumed in reactions forming crystallites contained within pores. Both black polymer variables, which had higher levels of porosity than the clear samples, showed substantially thinner ALD surface coatings along with extensive sub-surface crystallite formation.

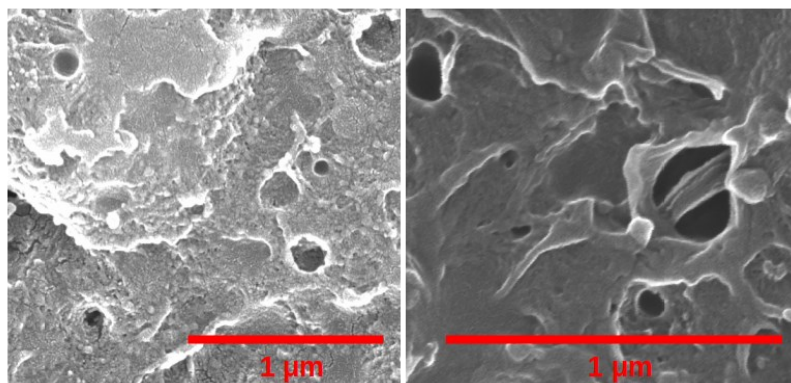


Figure 5.2: Porosity seen in a cross section of clear (left) and black (right) ABS. These large porous spaces allow precursor flow into the bulk of the plastic.

In attempting to understand why the penetration depth of TMA in black ABS exceeds that of clear ABS 3-D printed material, the characteristic that differentiates the two samples is the quality of the surface ALD-coating at the samples' surfaces. The black ABS samples exhibited patchy ALD coatings, with areas devoid of an oxide layer, as determined from SEM-EDS [54]. The clear ABS sample exhibited a thick, contiguous ALD coating, which suggests that after a period of TMA/H₂O cycling, a film built up that congested the inward diffusion of TMA into the polymer sample; with only a partial coating, the black ABS sample was free to uptake TMA throughout the ALD deposition process. However, the black and clear PC samples show the opposite behavior, with shallower penetration of TMA in the presence of porosity. This dissimilar behavior of black PC samples can potentially be explained by considering the material as a closed-cell foam, given the material was found to have in excess of 50% porosity [66].

All 3-D printed samples were tested for vacuum outgassing characteristics using the RGA setup. Figure 5.3 shows the outgassing measured in normalized partial pressure of entities with molecular masses from 1 to 100 AMU. Partial pressure recorded with a coated sample in the chamber was always less than that recorded with an uncoated sample. In fact, the chamber did not pump down to an acceptable level of vacuum in the defined time when an uncoated sample was used and the RGA could not be safely operated. It was observed that the ALD coated samples consistently recorded lower outgassing as compared to other test samples (a commercially available resin-Vacseal [67]). These other test samples are discussed in detail in previous work [48,54]. Further, an appreciable difference was not

seen between the different test plastics indicating ALD alumina is an effective outgassing barrier irrespective of the plastic used.

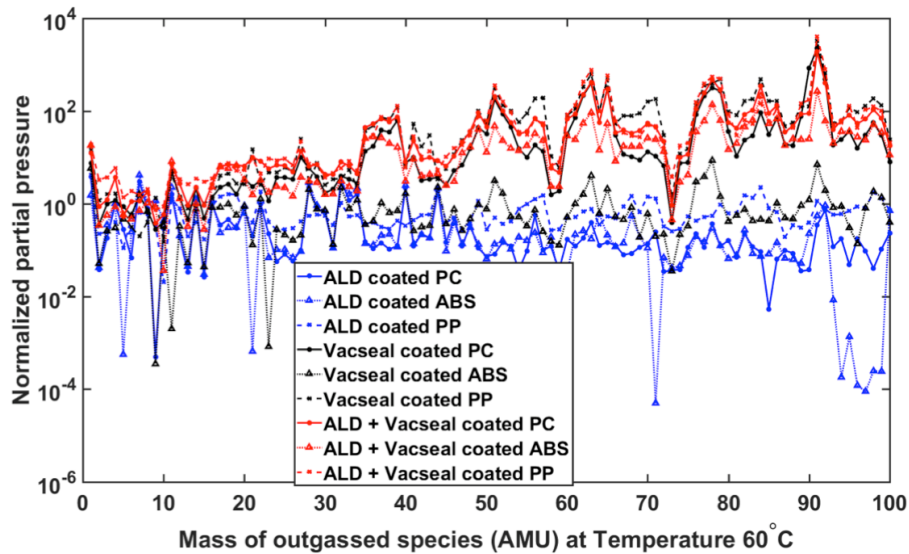


Figure 5.3: Vacuum outgassing characteristics of all black and clear samples showing the lowest recorded outgassing for ALD coated samples.

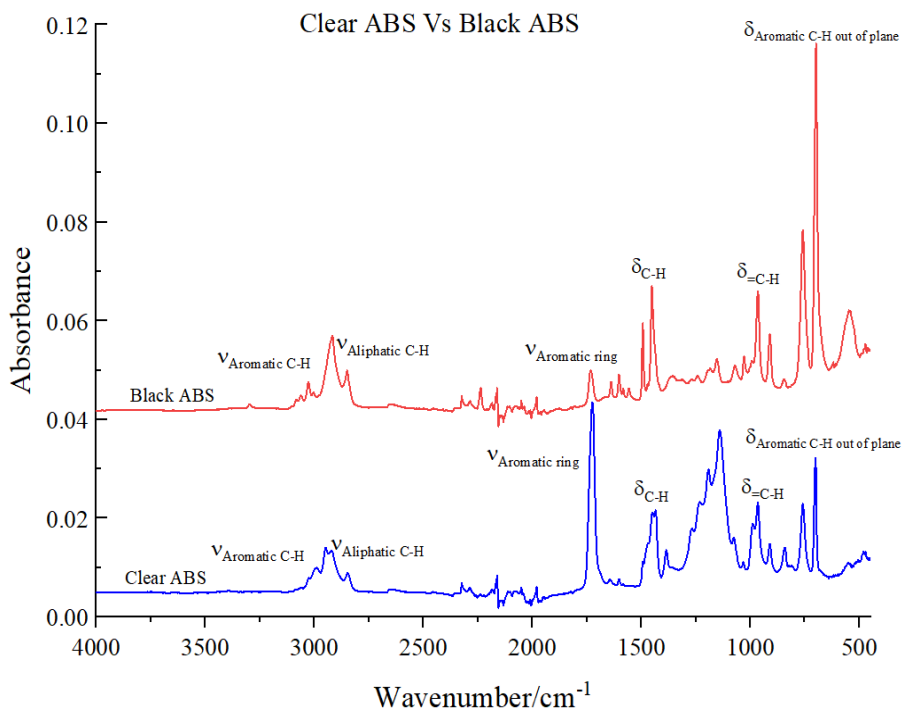
Recognizing the dependence of ALD film growth on the surface chemistry of the substrate [68], FTIR was used to characterize the difference in functional groups between the clear and black PC and the ABS polymers. Since the thickness and quality of ALD coatings differed greatly between black and clear polymers, it was theorized that the surface chemical signatures of these also differed. Also, all filament used in these studies is known to contain impurities that promote ease of 3-D printing. Each polymer has a unique vibrational signature, albeit identifying the impurities can be non-trivial. The structural similarities and differences between PC and ABS were identified using FTIR analysis (Figure 5.4).

The peak positions and their assignments of functional groups for both spectra show that the both clear ABS and black ABS contain the same main functional groups (both aromatic and aliphatic C-H, monosubstituted aromatic rings) suggesting that both have structural similarities [69-71]. The absorption intensities of certain vibrational peaks of clear and black ABS polymers, however, are considerably different. For example, stretching vibrations of aromatic ring (clear ABS – 1724 cm^{-1} and black ABS – 1732 cm^{-1}) and characteristic aromatic C-H out of plane bending vibrations (clear ABS – $759, 701\text{ cm}^{-1}$ and black ABS – $759, 698\text{ cm}^{-1}$) have shown clearly different intensities, which suggests that the relative abundance of monomers in the polymers may be different to each other.

ABS polymers are composed of three types of monomers which are acrylonitrile, butadiene and styrene. Styrene contains an aromatic ring (monosubstituted) and this makes characteristic strong IR absorption peaks in the fingerprint region of the FTIR spectra. The

nitrile functional group is present in both ABS polymers and is expected to have a strong absorption $C\equiv N$ stretch within $2100 - 2400\text{ cm}^{-1}$ region [71]. However, no absorbances are clearly observed of clear ABS nor black ABS polymers due to the interference of the ATR diamond cell in the same region.

The FTIR spectral comparison of pure and black PC polymers is shown in Figure 5.4(b). According to the main functional group assignments, black PC contains extra carbonyl peak ($C=O$) at 1725 cm^{-1} and an extra aromatic C-H in plane bending vibration peak at 957 cm^{-1} when compared to the FTIR spectrum of clear PC. This indicates that in addition to having carbon black in black polycarbonate, it also contains additional functional groups indicating that the structure of black PC monomer is different from the clear PC monomer.



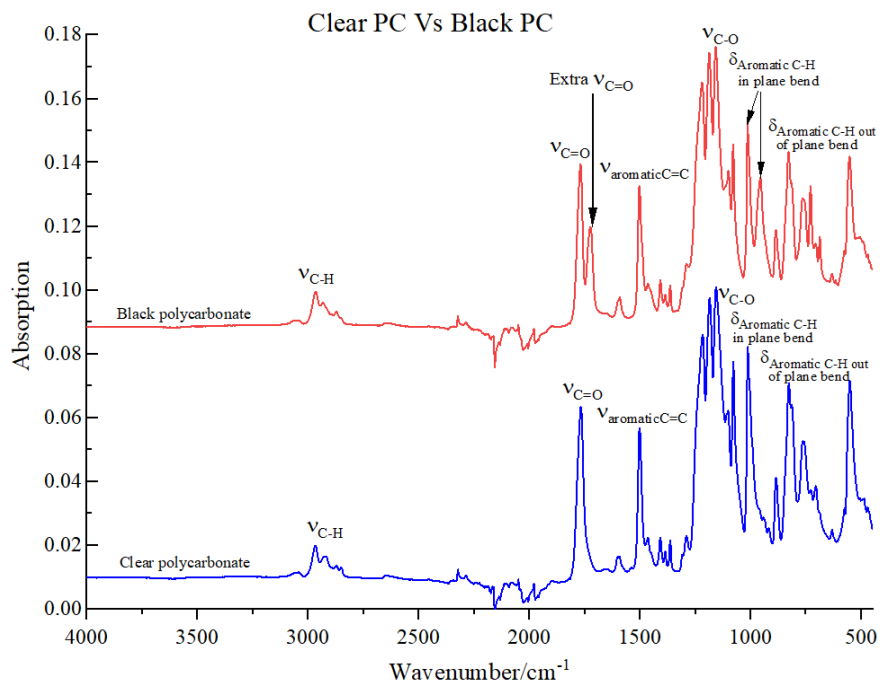


Figure 5.4: FTIR spectral comparison of black and unpigmented ABS and PC.

To further examine the contaminants present in these plastics, XPS was used to delineate the differences between black and clear samples (Figure 5.5). As compared to clear plastics, the black samples contained more aliphatic carbon, further hinting at the presence of higher amounts of carbon black. Silicon contamination was seen in all the samples. This was attributed to a contaminated ALD process chamber. In addition, Ca was seen in the ABS samples, likely present in the plastic as CaCO_3 is commonly added to ABS as a filler [72].

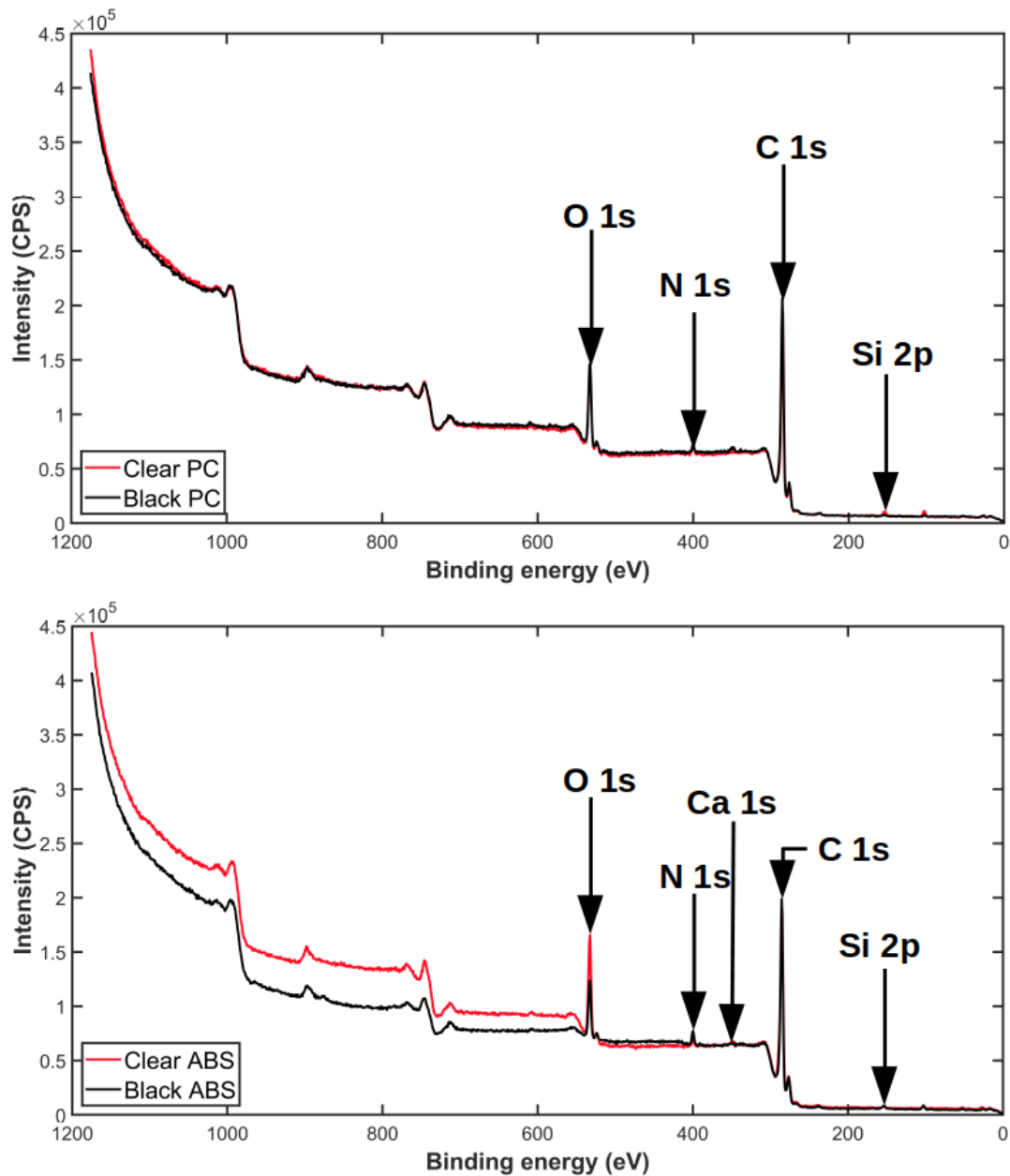


Figure 5.5: XPS spectra of black and clear a) PC and b) ABS samples. All samples showed Si contamination likely due to a contaminated ALD deposition chamber.

Since the substrate affects ALD growth [73,74], the crystallinity of all 5 polymeric materials was measured (Figure 5.6). XRD revealed PP to have the highest crystallinity at 26% while the other samples were determined to be amorphous. It is noted that the semi-crystalline PP is above its glass transition temperature (T_g) during deposition while the other samples are not. The semi-crystalline nature of PP coupled with its part-viscous state

during deposition effects porosity and hence, the mechanical and surface properties of this substrate [75], thus impacting ALD growth.

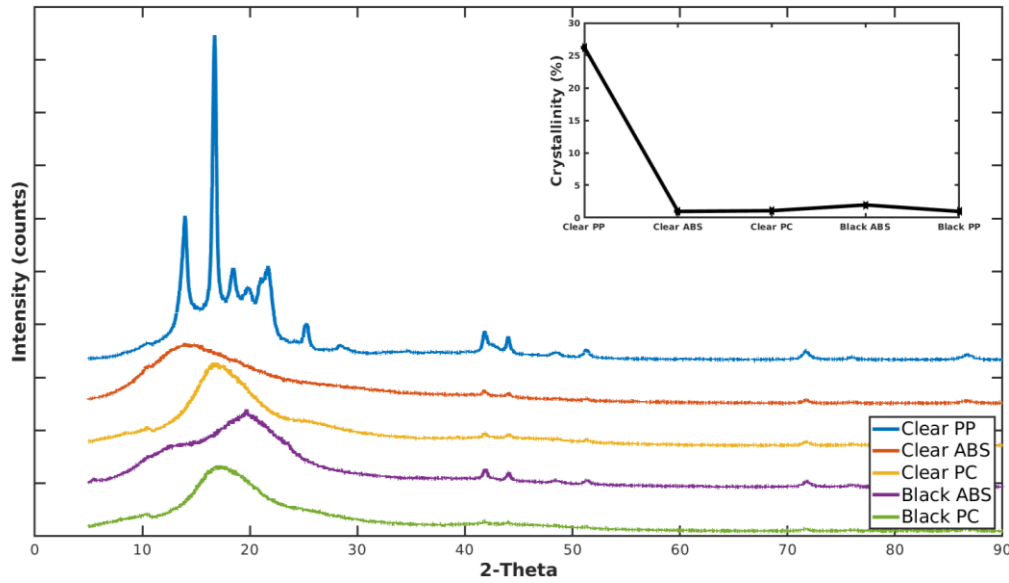


Figure 5.6: XRD spectra of all 3-D printed samples (inset) showing degree of crystallinity.

Table 5.1 provides a comparison between important physical properties and microstructure characteristics and TMA diffusion depth, as well as ALD coating thickness for all 3-D printed polymer samples.

Table 5.1: Comparison of T_g, porosity, crystallinity, and TMA diffusion depth and AlOx coating thickness. Note that diffusion depth is defined as the sub-surface depth at which the normalized Al K α signal was measured to be less than 0.1.

Sample	T _g (°C)	Porosity (%)	Crystallinity (%)	TMA Diffusion Depth (μm)	Apparent thickness of ALD Coating (μm)
ABS clear	105	8	<5	0.5	2.3 ± 0.2
ABS black	105	25	<5	1.8	0.21 ± 0.02
PC clear	150	0.1	<5	4.4	2.1 ± 0.3
PC black	150	58	<5	1.5	0.91 ± 0.07
PP clear	-20	2	26	1.6	0.88 ± 0.05

Selection of a material that would be used to build 3-D printed vacuum chamber components or the chambers themselves for contamination-sensitive applications involved studying vacuum outgassing characteristics. These depend on porosity and functionalization of the substrate as well as uniformity of coating. ALD was found to be

the optimal coating to inoculate materials against outgassing with its performance being superior to the commercially available resin. Black colored polymers were eliminated due to the presence of carbon black. Although an ALD coating would mitigate outgassing from them, it would have to be done in a contamination-insensitive chamber, separate from the where they will be used.

Semiconductor deposition systems, especially ALD, often use toxic and corrosive chemicals as precursors [76]. Hence, a chemically inert material needs to be chosen to build these chambers [77]. Unpigmented PP was chosen as the material of choice to build vacuum components due to its low outgassing and porosity. To further seal clear PP, an inorganic ALD coating will be deposited on the 3-D printed geometry to ensure that it can hold a vacuum. Other methods such as heat sealing are also being examined.

While clear PP filament does not contain any pigment, it does contain additives such as lubricants, solvents, plasticizers and antioxidants. Recognizing ALD as a surface science tool, ATR-FTIR spectra were obtained for commercially available PP filament and pure PP. According to the FTIR spectral comparison of pure and commercial polypropylene in Figure 5.7, both pure and commercial polypropylenes contain exactly the same functional groups at similar wavenumbers. Hence, from the perspective of an ALD process, the surface of both was found to be the same. Pure PP is a soft material and is thus challenging to print with, nor is it suitable for rigid vacuum chambers. An initial print concluded that pure PP does not have the mechanical strength required to build rigid objects. Since the surface signature from pure PP was the same as that obtained from filament PP, filament PP is the recommended material for future use.

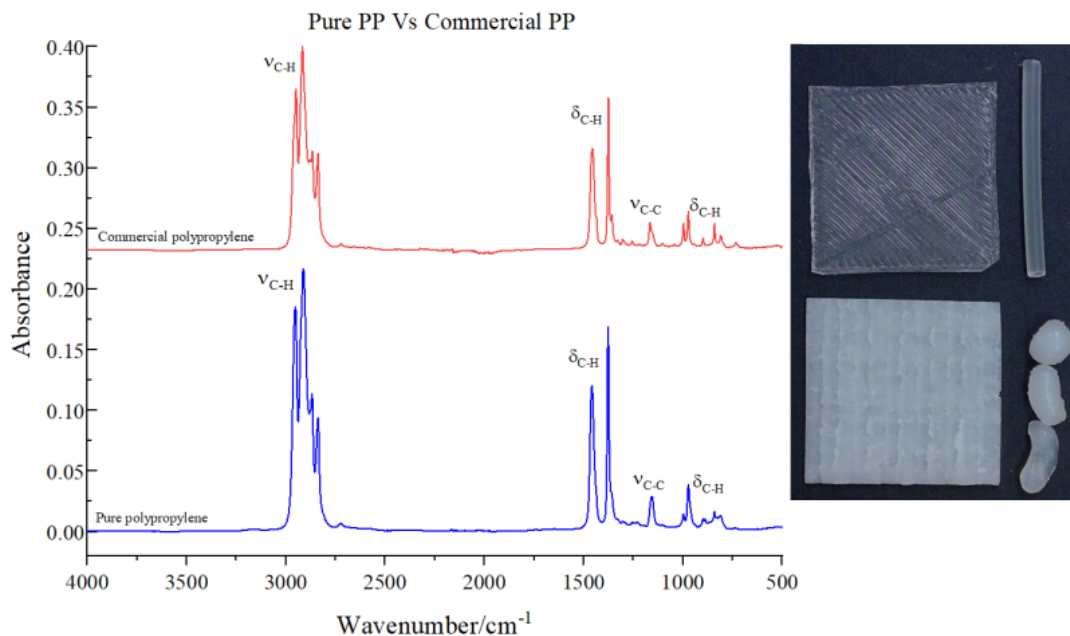


Figure 5.7: FTIR spectral comparison of pure polypropylene and commercial polypropylene filament shows additional carbon in pure PP. 3-D printed pure PP using a bespoke syringe printer setup shows soft and crumbly texture. This is compared against a similar sample printed using commercial filament.

XPS analysis of pure and filament PP revealed additional carbon contamination in pure PP (Figure 5.8). This was attributed to the printing method using a bespoke syringe 3-D printer. At elevated temperatures such as those required for printing, the steel syringe introduced carbon into the print. It should be noted that 3-D printing of pure PP was not treated as a clean process. While the syringe was wiped with 2-propanol prior to assembly, repeated tests involving finalizing printing parameters may have introduced carbon contamination. In addition, the presence of sodium on the surface of the pure PP sample further hints at contamination from handling.

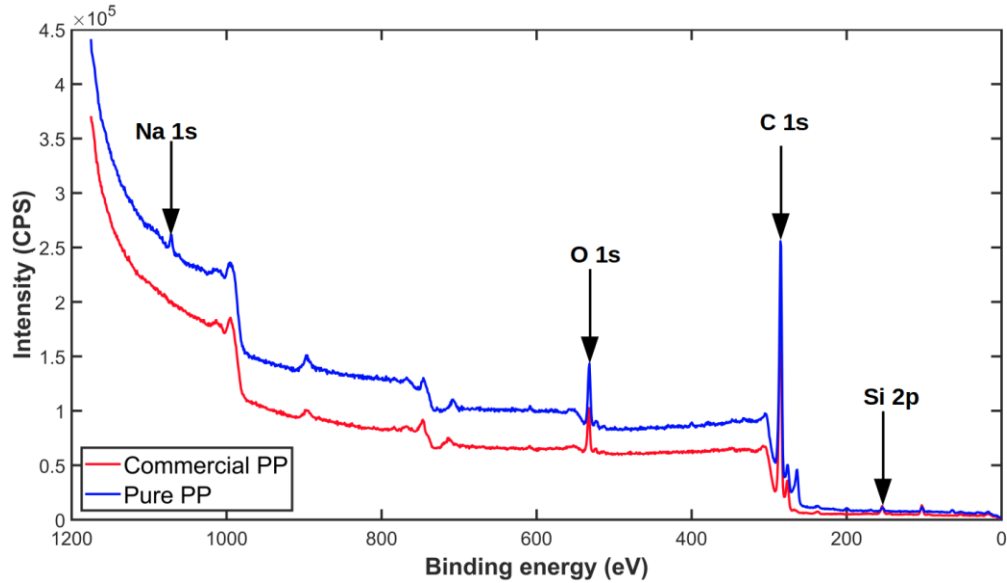


Figure 5.8: XPS spectra comparing pure PP to filament PP. The samples showed both sodium and silicon contamination.

With the selection of clear PP filament as the most appropriate low-temperature 3-D printing material, future work is required to study the mechanism of growth of ALD alumina on these different substrates. This way the deposition parameters can be adjusted more effectively to the material as well as the structure that is printed. An optimized thin film will increase the degassing barrier properties of the ALD alumina.

Currently, there is very limited literature available on ALD alumina coatings on polymers. Coating 3-D printed polymers is an even more nascent area of research. Nucleation and growth of alumina on spin coated polymer samples has shown that localized porosity [78, 79] and crystallinity [80] have an impact on nucleation and growth characteristics. The presence of an interfacial layer is theorized [81]. The growth of alumina using TMA and water is a complex function of both adsorption and diffusion limited absorption processes. Currently, the accepted models assume that no specific surface modification or terminating functional groups are necessary [82]. However, with 3-D printed plastics that contain several proprietary additives, the presence of mobile species is likely. Coupled with the higher porosity seen in these materials, these mobile additives would play an active role in the chemisorption of TMA to the plastic substrate. The effects of pigment, crystallinity, porosity, and surface states need to be examined as possible reasons for different diffusion depths of TMA and water in polymers, and hence different film growth morphologies. Currently, the authors theorize that film growth mechanism is a synergistic effect of all these factors. Long term stability tests, such as thermal cycling, are also needed to ascertain the use of these materials to build micro- and nano-fabrication tooling.

5.4 Conclusions

Low-cost 3-D printing was used to create samples from black pigmented and unpigmented PC and ABS, which were then coated ALD alumina. In addition, surface characteristics of additive-free PP was compared to commercially available PP filament. There was a marked reduction in outgassing of the ALD coated samples despite the non-uniformity of the coating. Whereas previous work shows the importance of temperature in TMA transport into polymers, this work suggests that moisture affinity of the matrix polymer may impact penetration depth of TMA. A multi-scale approach, as proposed here, is critical in understanding how the interfacial properties of plastic/alumina affect its bulk performance. XPS and FTIR-ATR are used to determine surface groups and bonding states to understand the affinity of the plastic for TMA and water. In addition, porosity and crystallinity calculations are used to correlate the measured thickness on the barrier coating to its outgassing protection capabilities. It is concluded that porosity, functional groups, and crystallinity all influence the growth of this ALD barrier film. In addition, this barrier film penetrates into the substrate to varying extents depending on the porosity of the substrate. Despite the defects on the surface, this film adequately remedied outgassing at very high vacuum (VHV) levels. Hence, a coated 3-D printed plastic material may be considered for building low temperature vacuum processing equipment and associated components.

5.5 Acknowledgements

This research was supported by the Witte Endowment and by Fulbright Finland. The authors acknowledge the provision of facilities and technical support by Aalto University at OtaNano – Micronova Nanofabrication Centre and at the RawMatTERS (RAMI) facilities. Parts of this study were completed using Michigan Technological University's Applied Chemical and Morphological Analysis Laboratory. The authors thank Adam Pringle and Shane Oberloier for technical assistance.

5.6 References

- [1] Burrows, P.E., Graff, G.L., Gross, M.E., Martin, P.M., Hall, M., Mast, E., Bonham, C.C., Bennett, W.D., Michalski, L.A., Weaver, M.S. and Brown, J.J., 2001, February. Gas permeation and lifetime tests on polymer-based barrier coatings. In *Organic Light-Emitting Materials and Devices IV* (Vol. 4105, pp. 75-83). International Society for Optics and Photonics.
- [2] Smokovych, I., Hasemann, G., Krüger, M. and Scheffler, M., 2017. Polymer derived oxidation barrier coatings for Mo-Si-B alloys. *Journal of the European Ceramic Society*, 37(15), pp.4559-4565.
- [3] Textor, T., Ittel, D.K. and Bahners, T., 2004. Inorganic-organic hybrid polymers based on silanes for coating textile substrates. *Silanes and Other Coupling Agents*, 3, pp.193-203.

- [4] Amberg-Schwab, S., Weber, U., Burger, A., Nique, S. and Xalter, R., 2006. Development of passive and active barrier coatings on the basis of inorganic–organic polymers. *Monatshefte für Chemie/Chemical Monthly*, 137(5), pp.657-666.
- [5] Wan, Y.J., Li, G., Yao, Y.M., Zeng, X.L., Zhu, P.L. and Sun, R., 2020. Recent advances in polymer-based electronic packaging materials. *Composites Communications*, 19, pp.154-167.
- [6] Krulevitch, P., Benett, W., Hamilton, J., Maghribi, M. and Rose, K., 2002. Polymer-based packaging platform for hybrid microfluidic systems. *Biomedical Microdevices*, 4(4), pp.301-308.
- [7] Kausar, A., 2020. A review of high performance polymer nanocomposites for packaging applications in electronics and food industries. *Journal of Plastic Film & Sheeting*, 36(1), pp.94-112.
- [8] Qin, Y., Howlader, M.M., Deen, M.J., Haddara, Y.M. and Selvaganapathy, P.R., 2014. Polymer integration for packaging of implantable sensors. *Sensors and Actuators B: Chemical*, 202, pp.758-778.
- [9] Phua, E.J.R., Liu, M., Cho, B., Liu, Q., Amini, S., Hu, X. and Gan, C.L., 2018. Novel high temperature polymeric encapsulation material for extreme environment electronics packaging. *Materials & Design*, 141, pp.202-209.
- [10] Willson, C.G., Dammel, R.R. and Reiser, A., 1997, July. Photoresist materials: a historical perspective. In *Metrology, Inspection, and Process Control for Microlithography XI* (Vol. 3050, pp. 38-51). International Society for Optics and Photonics.
- [11] Sun, G., Cho, S., Clark, C., Verkhoturov, S.V., Eller, M.J., Li, A., Pavía-Jiménez, A., Schweikert, E.A., Thackeray, J.W., Trefonas, P. and Wooley, K.L., 2013. Nanoscopic cylindrical dual concentric and lengthwise block brush terpolymers as covalent preassembled high-resolution and high-sensitivity negative-tone photoresist materials. *Journal of the American Chemical Society*, 135(11), pp.4203-4206.
- [12] Mann, B. and Kuhn, H., 1971. Tunneling through fatty acid salt monolayers. *Journal of Applied Physics*, 42(11), pp.4398-4405.
- [13] Polymeropoulos, E.E. and Sagiv, J., 1978. Electrical conduction through adsorbed monolayers. *The Journal of Chemical Physics*, 69(5), pp.1836-1847.
- [14] Netzer, L. and Sagiv, J., 1983. A new approach to construction of artificial monolayer assemblies. *Journal of the American Chemical Society*, 105(3), pp.674-676.
- [15] Langmuir, I., 1920. The mechanism of the surface phenomena of flotation. *Transactions of the Faraday Society*, 15(June), pp.62-74.

- [16] Ulman, A., 2013. *An Introduction to Ultrathin Organic Films: From Langmuir--Blodgett to Self-Assembly*. Academic press.
- [17] Cheng, Y., Emge, T.J. and Brennan, J.G., 1994. Polymeric Cd (Se-2-NC₅H₄)₂ and square planar Hg (Se-2-NC₅H₄)₂: Volatile CVD precursors to II-VI semiconductors. *Inorganic Chemistry*, 33(17), pp.3711-3714.
- [18] Cornu, D., Bernard, S., Duperrier, S., Toury, B. and Miele, P., 2005. Alkylaminoborazine-based precursors for the preparation of boron nitride fibers by the polymer-derived ceramics (PDCs) route. *Journal of the European Ceramic Society*, 25(2-3), pp.111-121.
- [19] Lin, H.Y., Luan, J., Tian, Y., Liu, Q.Q. and Wang, X.L., 2021. Thiophene-based Ni-coordination polymer as a catalyst precursor and promoter for multi-walled carbon nanotubes synthesis in CVD. *Journal of Solid State Chemistry*, 293, p.121782.
- [20] Parsons, G.N., George, S.M. and Knez, M., 2011. Progress and future directions for atomic layer deposition and ALD-based chemistry. *Mrs Bulletin*, 36(11), pp.865-871.
- [21] Pearce, J.M., 2012. Building research equipment with free, open-source hardware. *Science*, 337(6100), pp.1303-1304.
- [22] Pearce, J.M., 2013. *Open-source lab: how to build your own hardware and reduce research costs*. Elsevier: New York.
- [23] Pearce, J.M., 2020. Economic savings for scientific free and open source technology: A review. *HardwareX*, 8, p.e00139.
- [24] Pasanen, T.P., von Gastrow, G., Heikkinen, I.T., Vähänissi, V., Savin, H. and Pearce, J.M., 2019. Compatibility of 3-D printed devices in cleanroom environments for semiconductor processing. *Materials Science in Semiconductor Processing*, 89, pp.59-67.
- [25] Heikkinen, I.T.S., Savin, H., Partanen, J., Seppälä, J. and Pearce, J.M., 2020. Towards national policy for open source hardware research: The case of Finland. *Technological Forecasting and Social Change*, 155, p.119986.
- [26] Laikhtman, A., Gouzman, I., Verker, R. and Grossman, E., 2009. Contamination Produced by Vacuum Outgassing of Kapton Acrylic Adhesive Tape. *Journal of spacecraft and rockets*, 46(2), pp.236-240.
- [27] Patrick, T.J., 1981. Space environment and vacuum properties of spacecraft materials. *Vacuum*, 31(8-9), pp.351-357.
- [28] Jiao, Z., Jiang, L., Sun, J., Huang, J. and Zhu, Y., 2019, October. Outgassing environment of spacecraft: An overview. In *IOP Conference Series: Materials Science and Engineering* (Vol. 611, No. 1, p. 012071). IOP Publishing.

- [29] Patrick, T.J., 1973. Outgassing and the choice of materials for space instrumentation. *Vacuum*, 23(11), pp.411-413.
- [30] Shackelford, J., 1991. Gas Permeation and the Outgassing and Leak Testing of Vacuum Systems. *International Advances in Nondestructive Testing*, 16, pp.245-256.
- [31] Han, J.H. and Kim, C.G., 2006. Low earth orbit space environment simulation and its effects on graphite/epoxy composites. *Composite structures*, 72(2), pp.218-226.
- [32] Grossman, E. and Gouzman, I., 2003. Space environment effects on polymers in low earth orbit. *Nuclear Instruments and Methods in Physics Research Section B: Beam Interactions with Materials and Atoms*, 208, pp.48-57.
- [33] Chen, J., Ding, N., Li, Z. and Wang, W., 2016. Organic polymer materials in the space environment. *Progress in Aerospace Sciences*, 83, pp.37-56.
- [34] Povilus, A.P., Wurden, C.J., Vendeiro, Z., Baquero-Ruiz, M. and Fajans, J., 2014. Vacuum compatibility of 3D-printed materials. *Journal of Vacuum Science & Technology A: Vacuum, Surfaces, and Films*, 32(3), p.033001.
- [35] Jing, C.J.W.W.L., 2012. Effect of Thermal Vacuum Environment on Performance of Adhesive Bonding Materials. *Aerospace Materials & Technology*, p.06.
- [36] Jang, J.H., Hong, S.B., Kim, J.G., Goo, N.S., Lee, H. and Yu, W.R., 2019. Long-term properties of carbon fiber-reinforced shape memory epoxy/polymer composites exposed to vacuum and ultraviolet radiation. *Smart Materials and Structures*, 28(11), p.115013.
- [37] Khasanshin, R.H., Timofeev, A.N. and Ivanov, M.F., Mass loss of polymeric composites in vacuum in dependence on electron radiation intensity. The European Space Agency, retrieved 01/21/2021.
- [38] Benmalek, M. and Dunlop, H.M., 1995. Inorganic coatings on polymers. *Surface and Coatings Technology*, 76, pp.821-826.
- [39] Singh, B., Bouchet, J., Rochat, G., Leterrier, Y., Manson, J.A. and Fayet, P., 2007. Ultra-thin hybrid organic/inorganic gas barrier coatings on polymers. *Surface and Coatings Technology*, 201(16-17), pp.7107-7114.
- [40] da Silva Sobrinho, A.S., Latreche, M., Czeremuskin, G., Klemberg-Sapieha, J.E. and Wertheimer, M.R., 1998. Transparent barrier coatings on polyethylene terephthalate by single-and dual-frequency plasma-enhanced chemical vapor deposition. *Journal of Vacuum Science & Technology A: Vacuum, Surfaces, and Films*, 16(6), pp.3190-3198.
- [41] Johnson, R.W., Hultqvist, A. and Bent, S.F., 2014. A brief review of atomic layer deposition: from fundamentals to applications. *Materials Today*, 17(5), pp.236-246.

- [42] George, S.M., 2010. Atomic layer deposition: an overview. *Chemical Reviews*, 110(1), pp.111-131.
- [43] Ritala, M., Leskelä, M., Dekker, J.-P., Mutsaers, C., Soininen, P. J. and Skarp, J., 1999 *Chemical Vapor Deposition*, 5(1), 7-9.
- [44] Knaut, M., Junige, M., Neumann, V., Wojcik, H., Henke, T., Hossbach, C., Hiess, A., Albert, M. and Bartha, J.W., 2013. Atomic layer deposition for high aspect ratio through silicon vias. *Microelectronic Engineering*, 107, pp.80-83.
- [45] Shkondin, E., Takayama, O., Lindhard, J.M., Larsen, P.V., Mar, M.D., Jensen, F. and Lavrinenko, A.V., 2016. Fabrication of high aspect ratio TiO₂ and Al₂O₃ nanogratings by atomic layer deposition. *Journal of Vacuum Science & Technology A: Vacuum, Surfaces, and Films*, 34(3), p.031605.
- [46] Pardon, G., Gatty, H.K., Stemme, G., van der Wijngaart, W. and Roxhed, N., 2012. Pt–Al₂O₃ dual layer atomic layer deposition coating in high aspect ratio nanopores. *Nanotechnology*, 24(1), p.015602.
- [47] Cremers, V., Puurunen, R.L. and Dendooven, J., 2019. Conformality in atomic layer deposition: Current status overview of analysis and modelling. *Applied Physics Reviews*, 6(2), p.021302.
- [48] Wittbrodt B, Pearce JM. 2015. The effects of PLA color on material properties of 3-D printed components. *Additive Manufacturing*. 1;8:110-6.
- [49] Bihari, N., Heikkinen, I.T., Marin, G., Ekstrum, C., Mayville, P.J., Oberloier, S., Savin, H., Karppinen, M. and Pearce, J.M., 2020. Vacuum outgassing characteristics of unpigmented 3D printed polymers coated with atomic layer deposited alumina. *Journal of Vacuum Science & Technology A: Vacuum, Surfaces, and Films*, 38(5), p.053204.
- [50] Davis, A. and Golden, J.H., 1969. Stability of polycarbonate. *Journal of Macromolecular Science, Part C*, 3(1), pp.49-68.
- [51] Cantrell, J.T., Rohde, S., Damiani, D., Gurnani, R., DiSandro, L., Anton, J., Young, A., Jerez, A., Steinbach, D., Kroese, C. and Ifju, P.G., 2017. Experimental characterization of the mechanical properties of 3D-printed ABS and polycarbonate parts. *Rapid Prototyping Journal*, 23 (14).
- [52] Tanikella, N.G., Wittbrodt, B. and Pearce, J.M., 2017. Tensile strength of commercial polymer materials for fused filament fabrication 3D printing. *Additive Manufacturing*, 15, pp.40-47.
- [53] Heikkinen, I.T., Kauppinen, C., Liu, Z., Asikainen, S.M., Spoljaric, S., Seppälä, J.V., Savin, H. and Pearce, J.M., 2018. Chemical compatibility of fused filament fabrication-based 3-D printed components with solutions commonly used in semiconductor wet processing. *Additive Manufacturing*, 23, pp.99-107.

- [54] Heikkinen, I.T., Marin, G., Bihari, N., Ekstrum, C., Mayville, P.J., Fei, Y., Hu, Y.H., Karppinen, M., Savin, H. and Pearce, J.M., 2020. Atomic layer deposited aluminum oxide mitigates outgassing from fused filament fabrication–based 3-D printed components. *Surface and Coatings Technology*, 386, p.125459.
- [55] Zhang, C., Wijnen, B. and Pearce, J.M., 2016. Open-source 3-D platform for low-cost scientific instrument ecosystem. *Journal of Laboratory Automation*, 21(4), pp.517-525.
- [56] Pearce, J.M., Anzalone, N.C. and Heldt, C.L., 2016. Open-source wax RepRap 3-D printer for rapid prototyping paper-based microfluidics. *Journal of Laboratory Automation*, 21(4), pp.510-516.
- [57] Wijnen, B., Anzalone, G., Haselhuhn, A., Sanders, P. and Pearce, J., 2016. Free and open-source control software for 3-D motion and processing. *Journal of Open Research Software*, 4(1), p.e2.
- [58] Zhu, Z.W. and Zheng, Q.R., 2016. Methane adsorption on the graphene sheets, activated carbon and carbon black. *Applied Thermal Engineering*, 108, pp.605-613.
- [59] Crank, J. and Park, G.S., 1951. Diffusion in high polymers: some anomalies and their significance. *Transactions of the Faraday Society*, 47, pp.1072-1084.
- [60] Ashley, R.J., 1985. Permeability and plastics packaging. In *Polymer permeability* (pp. 269-308). Springer, Dordrecht.
- [61] Couchman, P.R. and Karasz, F.E., 1978. A classical thermodynamic discussion of the effect of composition on glass-transition temperatures. *Macromolecules*, 11(1), pp.117-119.
- [62] Hedenqvist, M. and Gedde, U.W., 1996. Diffusion of small-molecule penetrants in semicrystalline polymers. *Progress in Polymer Science*, 21(2), pp.299-333.
- [63] B. Gong and G. N. Parsons, 2012. Quantitative in situ infrared analysis of reactions between trimethylaluminum and polymers during Al₂O₃ atomic layer deposition," *Journal of Materials Chemistry*, 22, pp. 15672 - 15682.
- [64] Padbury, R.P. and Jur, J.S., 2014. Temperature-dependent infiltration of polymers during sequential exposures to trimethylaluminum. *Langmuir*, 30(30), p9228-9238.
- [65] Sefa, M., Ahmed, Z., Fedchak, J.A., Scherschligt, J. and Klimov, N., 2016. Gas uptake of 3D printed acrylonitrile butadiene styrene using a vacuum apparatus designed for absorption and desorption studies. *Journal of Vacuum Science & Technology A: Vacuum, Surfaces, and Films*, 34(6), p.061603.
- [66] L. Pilon, A. G. Fedorov and R. Viskanta, "Gas Diffusion in Closed-Cell Foams," *Journal of Cellular Plastics*, vol. 36, no. 6, pp. 451 - 474, 2000. Zaera, F., 2012. The

surface chemistry of atomic layer depositions of solid thin films. *The Journal of Physical Chemistry Letters*, 3(10), pp.1301-1309.

[67] <https://www.2spi.com/item/z05049/vacseal/>

[68] Zaera, F., 2012. The surface chemistry of atomic layer depositions of solid thin films. *The Journal of Physical Chemistry Letters*, 3(10), pp.1301-1309.

[69] Asensio, R.C., Moya, M.S.A., de la Roja, J.M. and Gómez, M., 2009. Analytical characterization of polymers used in conservation and restoration by ATR-FTIR spectroscopy. *Analytical and Bioanalytical Chemistry*, 395(7), pp.2081-2096.

[70] Jung, M.R., Horgen, F.D., Orski, S.V., Rodriguez, V., Beers, K.L., Balazs, G.H., Jones, T.T., Work, T.M., Brignac, K.C., Royer, S.J. and Hyrenbach, K.D., 2018. Validation of ATR FT-IR to identify polymers of plastic marine debris, including those ingested by marine organisms. *Marine Pollution Bulletin*, 127, pp.704-716.

[71] Noda, I., Dowrey, A.E., Haynes, J.L. and Marcott, C., 2007. Group frequency assignments for major infrared bands observed in common synthetic polymers. In *Physical properties of polymers handbook* (pp. 395-406). Springer, New York, NY.

[72] Tang, C.Y., Chan, L.C., Liang, J.Z., Cheng, K.W.E. and Wong, T.L., 2002. Mechanical and thermal properties of ABS-CaCO₃ composites. *Journal of Reinforced Plastics and Composites*, 21(15), pp.1337-1345.

[73] Puurunen, R.L., 2005. Surface chemistry of atomic layer deposition: A case study for the trimethylaluminum/water process. *Journal of Applied Physics*, 97(12), p.9.

[74] Hussin, R.O.S.N.I.Z.A., Choy, K.L. and Hou, X.H., 2015. The Effect of Substrate on TiO₂ Thin Films Deposited by Atomic Layer Deposition (ALD). In *Advanced Materials Research* (Vol. 1087, pp. 147-151). Trans Tech Publications.

[75] Newman, S. and Cox, W.P., 1960. The glass temperature of semicrystalline polymers. *Journal of Polymer Science*, 46(147), pp.29-49.

[76] Gordon, R.G., 2014. ALD precursors and reaction mechanisms. In *Atomic Layer Deposition for Semiconductors* (pp. 15-46). Springer, Boston, MA.

[77] Kurisu, H., Ishizawa, K., Yamamoto, S., Hesaka, M. and Saito, Y., 2008. Application of titanium materials to vacuum chambers and components. In *Journal of Physics: Conference Series* (Vol. 100, No. 9, p. 092002). IOP Publishing.

[78] Jain, T.S. and de Pablo, J.J., 2002. Monte Carlo simulation of free-standing polymer films near the glass transition temperature. *Macromolecules*, 35(6), pp.2167-2176.

[79] Pavel, D. and Shanks, R., 2003. Molecular dynamics simulation of diffusion of O₂ and CO₂ in amorphous poly (ethylene terephthalate) and related aromatic polyesters. *Polymer*, 44(21), pp.6713-6724.

[80] Compañ, V., López-González, M.M. and Riande, E., 2003. Langmuir sites in semicrystalline rubbery films?. *Macromolecules*, 36(22), pp.8576-8578.

[81] Mansfield, K.F. and Theodorou, D.N., 1991. Molecular dynamics simulation of a glassy polymer surface. *Macromolecules*, 24(23), pp.6283-6294.

[82] Wilson, C.A., Grubbs, R.K. and George, S.M., 2005. Nucleation and growth during Al₂O₃ atomic layer deposition on polymers. *Chemistry of Materials*, 17(23), pp.5625-5634.

6 Future Work

This dissertation describes the evaluation of ALD alumina as barrier coatings for 3-D printed plastic substrates and the potential to use these materials for custom open source scientific and processing equipment. It details a unique characterization plan, where the load lock of a molecular beam epitaxy system is used as a bespoke chamber to test different coatings on plastics. It recognizes the importance of a multi-scale approach, where the surface and the bulk properties together describe the mechanism of ALD on plastics. This highly interdisciplinary work brings in elements of material science in Chapters 3, 4 and 5 with discussions of structure-property-mechanism relationships. It delves into open source hardware design using mechanical and materials engineering concepts in Chapter 2. Chapter 2 also displays materials engineering coupled with electrical and computer engineering techniques used to make a control system and a firmware to run the optical characterization system. This dissertation as a whole demonstrates the need for in-depth knowledge in all of these fields to successfully understand how to efficiently coat porous plastic materials to someday create a tool that is capable of deposition in a vacuum environment. Through the course of this study, a number of ideas for improving the method of deposition of barrier coating were considered, and some of these are discussed below.

6.1 Precursor selection and process optimization

With the growing importance of low-cost alumina deposition in making lines and vias in back end of the line semiconductor processing, industry demands tools that have low capital cost, easy maintenance and characterizable output. While 3-D printed plastic reactors or components may be part of the answer, it is important to be able to define how these will be sealed to prevent outgassing into the chamber and then the sample.

In this work, the barrier coating applied is a TMA + water-based alumina. A number of other precursors may be used to create films that have different diffusion barrier properties. Any chamber used for deposition of inorganic materials of interest to the semiconductor industry must be hermetic. Hence, diffusion of water through this barrier coating deposited on a plastic substrate must be measured. Numerical modeling efforts to study diffusion of water through TMA-based and other alumina coatings may be initiated. While TMA has been studied as a precursor on silicon and metal substrates, modeling efforts on plastic substrates are severely lacking.

For the current process, multiple single variable tests (SVTs) for optimization are proposed. Longer purge times would help in adequately expelling excess precursor, except the adsorbed layer. In addition, a longer precursor dose would help in a more saturated plastic surface. The TMA + water ALD reaction occurs readily and is kinetically favorable at 80°C. An increase in substrate temperature as compared to chamber wall temperature will help in better loading of precursor on the substrate, leading to the reaction preferentially happening on the substrate. This method uses the precursor judiciously. A number of different methods of precursor delivery may also be tried, to increase the pressure of incoming precursor. Flow over vapor carrier gas methods, pulsing methods etc. can help in attaining a higher mass flow of TMA. However, temperature SVTs need to be handled

with caution since a higher temperature can lead to plastic substrate off gassing, deformation and melting. If the process is being tested on glass and silicon substrates, a very high temperature may not qualify the process to be translated as is to a plastic substrate. It might cause desorption of precursor and slow the deposition, or in an extreme case, dissociate the precursor leading to a highly reactive gas phase reaction (chemical vapor deposition).

6.2 Characterization of films

Since the desired application of these films is barrier coatings in the optoelectronics industry, in addition to extensive characterization using the gimbal system, it is also recommended that the resultant film be analyzed for physical and chemical properties. For this the use of both glass and silicon monitor wafers is recommended. It is important to gain data on the chemical nature of the film and presence of contaminants. FTIR is a surface sensitive technique ideally suited to check for the various bonds present apart from Al-O. Spectroscopic ellipsometry (SE) can give the user further insight into not just the thickness of the film, but also its uniformity. A multi- point scan will help in ascertaining if the active area of deposition in the system receives the same flux of precursor gases and hence results in the same thickness of AlO_x over the substrate surface. SE can also be used to determine stoichiometry of the film. This will further feed into process development for deposition. The effective medium approximation (EMA) layer may be used for this. In addition, optical constants may also be obtained using ellipsometry.

SEM imaging may be used to examine the film for presence of defects. It is recommended that a surface scan be done in addition to a cross section to determine pinhole and other defects in the layer. SEM based techniques such as EDS and x-ray mapping will also be useful to get data on contaminants as well as their spatial distribution.

While the primary application is on plastic substrates, characterization using spectroscopy is best done on glass and silicon substrates.

6.3 Education

The development of the open source 3-D printed gimbal system paves the way not only for production of inexpensive characterization tools, but also catalyzes interdisciplinary research in the field of electrical, materials and mechanical engineering. The low cost of the system makes it accessible for universities all over the world to research growth of thin films, their optical properties and their angle dependence. The author and collaborators particularly wish to see this technology being used to research and develop low-cost solar photovoltaic materials and devices. The ease of use and customization of the system will allow these to be manufactured local to where they are deployed, thus cutting costs and environmental impact further.

The easy build of the gimbal system is an advantage since K-12 education systems can use this as a tool to teach not only data comprehension (reading and following build instructions), but also physics and engineering basics. It allows for the development of many 3-D printing and Arduino based pre-college outreach programs through universities,

schools and local libraries as well as the opportunity of SMEs and maker spaces/fab labs to add a new powerful tool for materials characterization to their collections. As the ALD coating of 3-D printed plastics matures, in part with the assistance of the work described in this thesis, it may be possible for these same educational venues to begin to build and use vacuum system made from these materials. This will significantly expand their technical capacities and enable the open source model to not only be used for democratizing characterization tools, but also high-end vacuum-based processing of advanced materials.

A Copyright documentation

Chapter 2 is reproduced from “Bihari, N., Dash, S.P., Dhankani, K.C. and Pearce, J.M., 2018. 3-D printable open source dual axis gimbal system for optoelectronic measurements. *Mechatronics*, 56, pp.175-187,” with the permission of Elsevier.

Chapter 3 is reproduced from “Heikkinen, I.T., Marin, G., Bihari, N., Ekstrum, C., Mayville, P.J., Fei, Y., Hu, Y.H., Karppinen, M., Savin, H. and Pearce, J.M., 2020. Atomic layer deposited aluminum oxide mitigates outgassing from fused filament fabrication–based 3-D printed components. *Surface and Coatings Technology*, 386, p.125459,” with the permission of Elsevier.

Chapter 4 is reproduced from “Bihari, N., Heikkinen, I.T., Marin, G., Ekstrum, C., Mayville, P.J., Oberloier, S., Savin, H., Karppinen, M. and Pearce, J.M., 2020. Vacuum outgassing characteristics of unpigmented 3D printed polymers coated with atomic layer deposited alumina. *Journal of Vacuum Science & Technology A: Vacuum, Surfaces, and Films*, 38(5), p.053204,” with the permission of AIP Publishing.